THE UNIVERSITY OF HULL

Using External Fields to Control the Behaviour of Anisotropic Particles at Liquid Interfaces

being a Thesis submitted for the Degree of Doctor of Philosophy

in the University of Hull

by

Bethany Jade Newton, B.Sc. (Hons.)

Department of Physics

August 2016

Summary of Thesis

In this thesis we use analytical theory and high resolution finite element simulations (using the program 'Surface Evolver') to consider the influence of an external magnetic field on the orientation and self-assembly of rod-like magnetic particles.

Firstly, we calculate the equilibrium tilt angle with respect to the undeformed interface and the meniscus shape around an ellipsoidal particle when a magnetic field is applied perpendicular to the interface. As we increase field strength, the particle undergoes a discontinuous transition to the 'perpendicular' orientation. We show that it is necessary to include meniscus deformations in our calculations in order to accurately model this transition. We also show for the first time that the tilt angle vs. magnetic field curve exhibits *hysteresis* behaviour.

Secondly, we study the orientation of magnetic cylindrical particles. For cylindrical particles at a liquid interface, orientational transitions induced by an external field remain when the external field is removed i.e. the switching effect is *non-volatile*. By tuning both the aspect ratio and contact angle, we show that it is possible to engineer cylindrical particles that have multiple locally stable orientations and hence obtain extremely rich magnetic responses to an external field. We show that such systems provide a facile platform for creating *switchable* functional materials.

Finally, we investigate the interactions between, and self-assembly of, multiple ellipsoidal particles. For two ellipsoidal particles, the only stable configuration was found to be the side-to-side configuration. However, for three ellipsoidal particles, the tip-to-tip configuration was also found to be locally stable. There is good qualitative agreement between our finite element simulations and a linearised analytical theory and we attribute quantitative discrepancies between the two to non-linear and many-body effects.

Contents

Acknowledgements

I would like to thank my supervisor, Dr. D. Martin A. Buzza, for his excellent guidance, support and encouragement as well as his help in securing funding for the duration of my studies. His extensive knowledge has been invaluable.

Sincere gratitude goes to the University of Hull for waiving my fees and for part of my financial support. I thank Professor Mary O'Neill who helped secure funding for me and the Department of Physics for financial support for conferences and educational visits.

I express my gratitude to the three charities that funded my living expenses namely: The Joseph and Annie Cattle Trust; The Elizabeth F. Walker Foundation and The Ann Watson's Trust; without their generosity I would not have been able to even begin the Ph.D. I would also like to thank the James Reckitt Charitable Trust for the James Reckitt Achievement Bursary which has supported me in the final months of study.

I could not have completed any of the simulation work without some guidance from the creator of Surface Evolver, Professor Kenneth A. Brakke. His vast knowledge as well as tips and tricks with the program were very helpful. I also thank Dr Lorenzo Botto for his expertise in developing the interaction potential equations used for the results in Chapter 6.

A big thank you is extended to the guys I have shared an office with namely: Abdulsattar, Addison, Ant, Dan, Dean, Lee, Nick and Raj. A lot of laughs and encouragement have been shared which made the Ph.D. research much more enjoyable on what can be a lonely journey. Finally, but by no means least, I would like to thank all of my family and my fiancé for their understanding and confidence in my abilities.

Declaration of Authorship

I declare that the work is original and has not been submitted previously for examination or award. Where I have used the results or work of others they have been acknowledged accordingly.

Some of my work that forms part of this thesis has been the source of conference presentations and journal publications shown below:

Poster Presentations

- B. J. Newton and D. M. A. Buzza, "Influence of Magnetic Field on the Orientation of Anisotropic Magnetic Particles at Liquid Interfaces", The Physics of Soft and Biological Matter, Homerton College, Cambridge, UK, April 2014.

- B. J. Newton and D. M. A. Buzza, "Influence of Magnetic Field on the Orientation of Anisotropic Magnetic Particles at Liquid Interfaces", Soft Interfacial Materials Discussion Meeting, The Royal Society, London, UK, October 2015.

Publications

- Bethany J. Newton, Kenneth A. Brakke and D. Martin A. Buzza, "Influence of magnetic field on the orientation of anisotropic particles at liquid interfaces", *Physical Chemistry Chemical Physics*, **16** (2014), pp.26051–26058.

- Bethany J. Newton and D. Martin A. Buzza, "Magnetic cylindrical colloids at liquid interfaces exhibit non-volatile switching of their orientation in an external field", Soft Matter, **12** (2016), pp.5285-5296.

This thesis contains approximately 24300 words, 52 figures and 4 tables.

Bethany J. Newton
August 2016

Dedicated to Dennis Kirman

See You Later Alligator

Chapter 1
Introduction

1.1. Particles at Liquid Interfaces

Particles adsorbed at fluid interfaces have been extensively studied in the last three decades due to their many applications in soft matter systems ranging from: particle stabilised emulsions and foams (i.e. Pickering emulsions);[1, 2] to membrane and interfacial proteins;[3] to functional surfaces for nanotechnology; [4, 5] to personal care products, foods and paint.[6] In this thesis we focus on colloidal particles, which are in the nanometre to micrometre range.[1] This mesoscopic size scale is interesting since in this regime, the particles are large enough so that we can ignore the microscopic details of the solvent molecules and treat both the bulk fluid phases and the fluid interface as a continuum. On the other hand, the particles are small enough so that gravitational forces are unimportant and the behaviour of the particles at the fluid interface is primarily controlled by surface tension (i.e. capillary) forces rather than gravity. Most of the research in this area has focused on spherical or nearly spherical particles. However, with advances in the synthesis of colloidal particles, particles with other shapes have received increasing attention over the last decade. A non-exhaustive list of these shapes include ellipsoids,[7–10] cylinders,[11, 12] cubes[13] and more exotic shapes including microbullets,[14] dumbbells,[15, 16] corrugated particles,[17] and particles with complex cross-sections.[18] A review of the literature with a focus on ellipsoidal and cylindrical particles is presented in Chapter 2. In Section 1.3 we review other interesting shapes and their potential applications. It has been suggested

that these new shapes could be exploited to assemble useful structures or new materials; however, a better understanding is required of the interactions and assembly of anisotropic particles.[19] In this thesis we will focus on ellipsoidal and cylindrical colloidal particles.

1.2. Spherical Particles

We will start our discussion by considering the simpler case of spherical particles at a fluid interface. When colloidal particles adsorb at an interface a key factor is the three phase contact angle, θ_w, given by Young's Equation

$$\cos\theta_w = \frac{\gamma_{po} - \gamma_{pw}}{\gamma_{ow}} \tag{1.1}$$

where γ_{po}, γ_{pw},γ_{ow} are the interfacial tensions of the particle/oil, particle/water and oil/water interfaces respectively. In Figure 1.1 we show the effect of varying contact angle for a spherical particle in its equilibrium position relative to the fluid interface when gravity can be ignored. The situation where gravity is important will be considered later in this section.

For a contact angle $\theta_w = 90°$ the particle is equally wetted by, in this case, the oil and water. When a spherical particle with a constant contact angle different to 90° is adsorbed at a liquid interface, the particle moves up into the oil phase or down into the water phase so that it is in equilibrium. As perfectly smooth spheres are axisymmetrical this satisfies the wetting boundary condition without the particle deforming the liquid interface. For hydrophilic particles the contact angle is less than 90° so that a larger section of the

particle is in the water phase than in the oil phase, shown in Figure 1.1(a). For hydrophobic particles the contact angle is greater than 90° with more of the particle in the oil than in the water phase, shown in Figure 1.1(c). For an ideal surface the contact angle will be the angle calculated by Equation 1.1. However, in the real world the contact angle can vary slightly due to defects, either chemical or physical.[20] Contact angles can exhibit hysteresis which is found by calculating the difference between the advancing (θ_A) and the receding (θ_R) contact angles. If a liquid drop is inflated on a flat solid substrate the contact angle will exceed the angle given by Young's equation without the contact line moving; the threshold where further inflation moves the contact line is known as the advancing contact angle, θ_A. Similarly, if a drop is deflated, the contact angle decreases to a limit known as the receding angle, θ_R.[20] In all our simulation work we will ignore contact angle hysteresis and assume that the contact angle is the equilibrium value given by Young's equation.

Assuming gravity is negligible and neglecting line tension, the behaviour of the particles at the interface is controlled by surface tension. The energy required to remove a particle from the interface is given by

$$E = \pi R^2 \gamma_{ow} \left(1 \pm \cos\theta_w\right)^2 \tag{1.2}$$

where R is the radius of the particle, γ_{ow} is the interfacial tension between oil and water and θ_w is the contact angle.[21] It is reasonable to neglect line tension since its effects are only noticeable for nano-sized particles, whereas in this thesis the focus is on micron-sized particles.[22] In Equation 1.2, the positive value is used for transfer from the interface into the oil. The negative

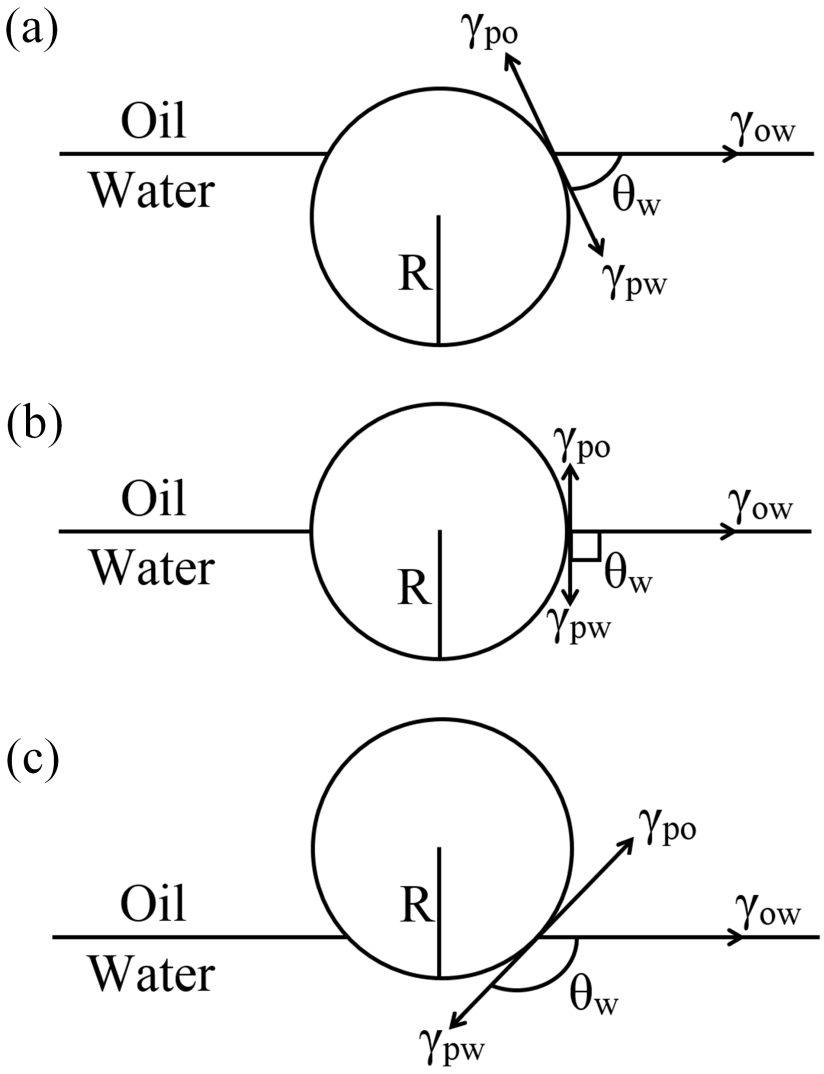

Figure 1.1: Spherical particle at an oil-water interface with different contact angles (θ_w) (a) hydrophilic particle $\theta_w < 90°$ (b) neutrally wetted particle $\theta_w = 90°$ (c) hydrophobic particle $\theta_w > 90°$

value is used for transfer from the interface into the water. The free energy of detachment of a spherical particle is at a maximum when the contact angle is at 90° i.e. when the spherical particle is equally wetted by the two liquids. Using typical values for a particle with $R = 10\,nm$, $\gamma_{ow} = 30\,mN\,m^{-1}$ and $\theta_w = 90°$ gives the energy of detachment $E = 2290\,k_BT$, which means that colloidal particles essentially attach to an interface irreversibly. As the energy barrier is thousands of k_BT, thermal energy is insufficient to remove the particle from the interface.

Lateral capillary forces arise between particles at liquid interfaces when there is overlap of the deformation of the interface caused by the adsorbed particles.[23] For large particles, $\gtrsim 10\mu m$, the deformation of the liquid meniscus can arise due to the weight or buoyancy of the particles and the resultant capillary forces are called flotation forces, see Figure 1.2.[24–26] The sign of the meniscus slope angles ψ_1 and ψ_2 at the two contact lines determines if the lateral capillary force will be attractive (Figure 1.2(a)) or repulsive (Figure 1.2(b)). Specifically, the capillary force is attractive when $\sin\psi_1 \sin\psi_2 > 0$ and repulsive when $\sin\psi_1 \sin\psi_2 < 0$. Not surprisingly the larger the interfacial deformation created by the particles the stronger the capillary interaction between them.[25]

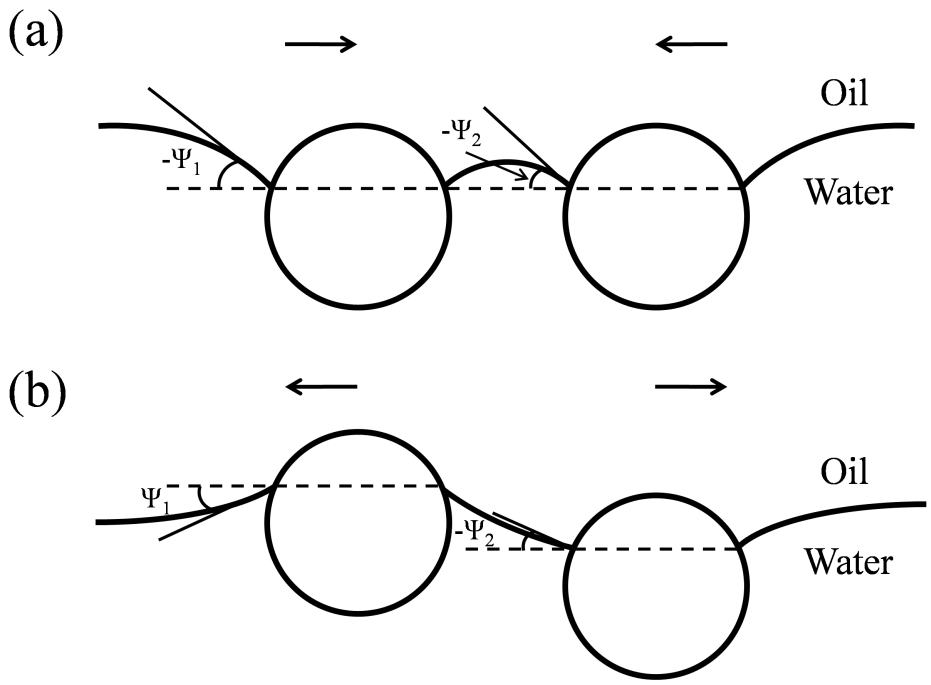

Figure 1.2: Flotation forces for two spherical particles, ψ_1 and ψ_2 are the meniscus slope angles (a) attraction between similar floating particles (b) repulsion between a light and heavy floating particle.[25]

Bond number is the ratio of gravitational effects to the surface tension forces which is given by the following equation,

$$B = \frac{(\rho_{water} - \rho_{oil})R^2 g}{\gamma_{ow}} \tag{1.3}$$

where B is the Bond number, ρ_N is the density of water or oil, R is the radius of the particle, g is the acceleration due to gravity and γ_{ow} is the interfacial tension of the oil-water interface. Using typical values for these parameters gives a very small Bond number, in the order of 10^{-5} or less [27] and therefore, gravitational effects may be disregarded. We do not account for flotation forces as we can demonstrate using Bond number why gravity is negligible for the particle dimensions which we consider.

1.3. Non-Spherical Particles

Bowden et al. first demonstrated the effect of capillary interactions caused by complex shapes at an interface and showed that they can be used to drive the assembly of particles into desired structures based on the properties of the particles. Although these results were for mesoscopic particles this research led to interest in capillary interactions for smaller complex shaped particles.[28] Brown et al. looked at micron-sized particles showing that quadrupolar deformation due to the anisotropic particles caused the particles to interact and form ordered structures.[29] The behaviour of anisotropic particles at fluid interfaces is even richer than that of spherical particles for two reasons. Firstly, anisotropic particles can adopt multiple locally stable orientations at the liquid interface.[11, 13, 30–33] Secondly, for non-neutrally wetting particles (i.e., con-

tact angle $\theta_w \neq 90°$), the constant contact angle requirement at the three phase contact line leads to significant deformations of the liquid meniscus around the anisotropic particles and hence strong capillary interactions between particles. [7–10, 12, 23, 34, 35] This is because anisotropic particles are non-axisymmetric and therefore, to satisfy a constant contact angle, the liquid interface has to deform. In fact, the leading order term turns out to be quadrupolar which is observed in Figure 1.3(b) for a single ellipsoidal particle; that is, for a hydrophilic particle, a rise along the sides and depressions at the ends of the ellipsoid. For small particles, $\lesssim 10\mu m$, capillary forces can still arise between anisotropic particles due to the contact line undulations with overlapping deformations causing the particles to self-assemble into a variety of structures.

Both the orientation of individual particles and the capillary interaction between particles are strongly dependent on the shape of the anisotropic particle. For example, for ellipsoidal particles, the equilibrium orientation is always 'side-on' (i.e., particle long axis parallel to liquid interface),[9] while for cylindrical particles, the equilibrium orientation can be 'side-on' or 'end-on' (i.e., particle long axis perpendicular to liquid interface).[11] In addition, while the far-field capillary interactions between both ellipsoidal and cylindrical particles are quadrupolar,[7–10, 12, 23, 34] the near-field capillary interactions are strongly shape dependent, causing ellipsoidal particles to prefer to assemble side-to-side (identical ellipsoids) or at an angle (non-identical ellipsoids) and cylindrical particles to prefer to assemble tip-to-tip.[23, 34, 36]

If in addition, we can change the orientation of anisotropic particles by means of an external field (e.g. by embedding a magnetic dipole within the particle),

which allows us to tune the orientation and capillary interactions between such particles and hence control their self-assembly. The ability to engineer and control the configuration of anisotropic particles at liquid interfaces opens up exciting possibilities for the manufacture of switchable materials with specific mechanical, optical or magnetic properties.

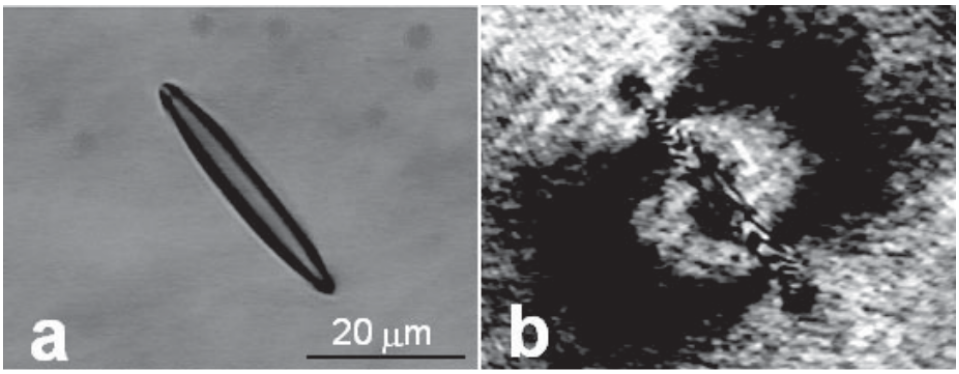

Figure 1.3: (a) Image of a single ellipsoidal particle in a similar orientation to (b) which shows a Phase Shifting Interferometry (PSI) image of the quadrupolar deformation present for $\theta_w = 39°$.[8]

Cubes have recently been investigated by Morris et al.; specifically, the authors studied the orientation of cubes in a thin film. They found that cubic particles with high contact angles favour a twisted/tilted orientation but rupture the thin film easier than if wider, flatter particles with low contact angles are used. Their work provided useful insight into thin film stability which the authors suggest could have implications for self assembly of particles and also the separation of precious minerals which is used in the flotation industry.[13, 37, 38] Recent applications of the use of anisotropic particles dispersed in nematic liquid crystals have found interesting one dimensional chains for planar cells or two dimensional structures for homeotropic cells at the interface.[14] This deepens the understanding of directed assembly of anisotropic particles within complex fluids. Park et al. provided insight into the ori-

entation of Janus dumbbells for varying particle size, aspect ratio and surface properties. They found a primary energy minimum which has advantages for obtaining particle layers at fluid-fluid interfaces with uniform orientation.[16] Their research provides a way of designing particles with specific properties that are tailored for a particular application. Corrugated particles have been found to have quadrupolar deformation in the far field; however, in the near field periodic deformations have been observed with different wavelengths of the particles reaching an equilibrium separation, which suggests capillary repulsion can be used to create microparticle assembly that is not in contact.[17] Lewandowski et al. have studied particles with complex cross-sections (the particles studied have planar sides and curved ends) and found preference for assembly that is based on the aspect ratio of the particles, with planar sides coming together for aspect ratios of 0.66 and particles favouring the curved ends together for an aspect ratio of 4.[18, 23]

1.4. Aim and Outline of Thesis

The aim of this thesis is to investigate the orientation, capillary forces and self-assembly of anisotropic colloidal particles at liquid interfaces, under the influence of an external field. The specific shapes we will study include ellipsoids and cylinders and they will be investigated theoretically using analytical theory and finite element simulations.

The rest of the thesis is structured as follows: in Chapter 2 we review the literature relevant to our study, including both experimental and theoretical studies. Particles under consideration range from spheres, to anisotropic particles,

to Janus particles. In Chapter 3 we outline the finite element method Surface Evolver used for the results presented in the rest of the thesis. In Chapter 4 we present results for an ellipsoidal particle at a liquid interface under the influence of an external field. We investigate the equilibrium meniscus shape when a magnetic field is applied perpendicular to the interface for varying contact angle, aspect ratio and tilt angle.[39] In Chapter 5 we investigate the effect of an external field on a cylindrical particle. By tuning both the aspect ratio and contact angle of the cylinders, we show it is possible to have multiple stable orientations at different tilt angles.[40] In Chapter 6 we study the effect an external field has on multiple ellipsoidal particles. Specifically, we present results for 2 and 3 ellipsoids for varying tilt and bond angles, to find the orientation with the lowest free energy. Finally, in Chapter 7 we outline the conclusions from the thesis and discuss potential future work.

Chapter 2
Theoretical Background and Literature Review

In this Chapter, we outline some of the important concepts for particles at a liquid interface and present key findings from the literature which will be extended to form the basis for the rest of the thesis. Specifically, in Section 2.1, we look at the interface deformation around isolated particles presenting the key equations and approximations for the interfacial profile. In Section 2.2 and 2.3 we review multiple particles at a liquid interface, paying particular attention to capillary interaction (the interaction caused by overlapping deformations of the liquid interface) and self-assembly (particles self-organising into favoured orientations). In Section 2.4 the preferred orientation of anisotropic particles in zero field is investigated. Finally, in Section 2.5 the ability to manipulate the orientation of anisotropic particles in an external field is considered.

An important parameter that describes the geometry of rod-like particles is aspect ratio. For cylindrical particles this is defined as

$$\alpha = \frac{L}{2r} \tag{2.1}$$

where α is the aspect ratio, L is length of the particle and r is the radius of the particle (see Figure 2.1(a)).

For ellipsoidal particles, the aspect ratio is given by

$$\alpha = \frac{z_m}{r_m} \tag{2.2}$$

where α is the aspect ratio, z_m is the semi-major axis, r_m is the semi-minor axis (see Figure 2.1(b)). The effect of different aspect ratios is one of the variables investigated in this thesis.

(a) (b)

Figure 2.1: Aspect ratio for (a) a cylindrical particle and (b) an ellipsoidal particle

2.1. Interface Deformation by Isolated Particles

In this section, we outline the key equations to describe the meniscus around isolated particles at a liquid interface, identifying the best coordinate system to correctly represent deformations of the interface for rod-shaped particles.

When colloidal anisotropic particles are adsorbed at an interface between two immiscible fluids, several factors will decide the shape of the meniscus produced. These include the aspect ratio, contact angle and orientation of the particle. For micron-sized particles, where gravity can be neglected, the Young-Laplace equation can be used to describe the shape of the meniscus around an adsorbed particle. Specifically, each point of the fluid interface around the adsorbed particle obeys the equation

$$\triangle P = \gamma \left(\frac{1}{r_1} + \frac{1}{r_2} \right) \tag{2.3}$$

where $\triangle P$ is the pressure difference between the two bulk phases separated by the meniscus, γ is the surface tension of the interface, r_1 and r_2 are the two principle radii of curvature at any point on the meniscus.

The right hand side of Equation 2.3 is the capillary pressure, i.e. the pressure difference across an interface due to the curvature of the interface. For small enough deformations we can approximate the curvature by $\left(\frac{1}{r_1} + \frac{1}{r_2}\right) \approx \nabla^2 h$ so that $\triangle P = \gamma \nabla^2 h$. Here, ∇^2 is the 2D Laplacian operator which in Cartesian coordinates is defined as $\nabla^2 = \frac{\partial^2}{\partial x^2} + \frac{\partial^2}{\partial y^2}$ and h refers to the height of the meniscus as a function of $2D$ in plane coordinates. Far from the particle the meniscus is flat, so $\triangle P = 0$. Therefore, when gravity is neglected, the interface deformation obeys the 2D Laplace equation

$$\nabla^2 h = 0. \tag{2.4}$$

Solving Equation 2.4 thus allows us to determine the shape of the meniscus h around an adsorbed particle.

Depending on the symmetry of the problem, the Laplace equation can be solved in different coordinate systems. For spherical or near spherical particles, where the symmetry is circularly symmetric, the natural coordinate system to use is circular polar coordinates. In circular polar coordinates, the general solution of Equation 2.4 is [23]

$$h(r, \theta) = A_0 \ln r + \sum_n \frac{A_n}{r^n} \cos(n\theta) \tag{2.5}$$

where r and θ are polar coordinates in a particle centred reference frame.[41]

The coefficient A_n is the amplitude of the interface. The term $\ln r$, in Equation 2.5, is a polar monopole, $r^{-1}\cos\theta$ is a polar dipole, $r^{-2}\cos(2\theta)$ is a polar quadrupole etc. Monopoles are forbidden because there is no external force like gravity; dipoles are also not present because there is no external torque rotating the particles away from their optimum orientation. Therefore, the quadrupole term, which describes the shape of the contact line, is the lowest allowed multipole order. Higher order multipoles also describe the contact line and are significant when close to the particle. This will be discussed later in this Chapter.[23, 41] It is convenient to rewrite the capillary quadrupole as

$$h(r,\theta) = H_p \left(\frac{r_p}{r}\right)^2 \cos(2\theta) \tag{2.6}$$

where H_p (A_2 in Equation 2.5) is the amplitude of the interface along the circular contour of radius r_p surrounding the particle. For a quadrupole the interfacial deformation is symmetric around two perpendicular axes with rise and fall, see Figure 2.4.[23] For a perfectly smooth sphere there is no meniscus deformation, see Chapter 1, Section 1.2. However, for real spheres, surface roughness leads to contact line undulations and meniscus deformation where the lowest order multipole is a quadrupole given by Equation 2.6.

Elliptical coordinates are a two-dimensional coordinate system which is the most convenient coordinate system for solving the Laplace equation when rod-like particles (e.g. ellipsoids and cylinders) are adsorbed in the side-on orientation at the liquid interface, see Figure 2.2.[9] A particle-centred elliptical coordinate system (s,t) is related to the Cartesian coordinate system (x,y) by

the following transformations

$$x = \beta \cosh s \cos t \tag{2.7}$$

$$y = \beta \sinh s \sin t \tag{2.8}$$

where β is a length scale related to the distance from the origin. The coordinate system in Figure 2.2 shows different values of constant s producing ellipses and constant values of t creating hyperbolae. Specifically, β controls the aspect ratio of constant s ellipses.

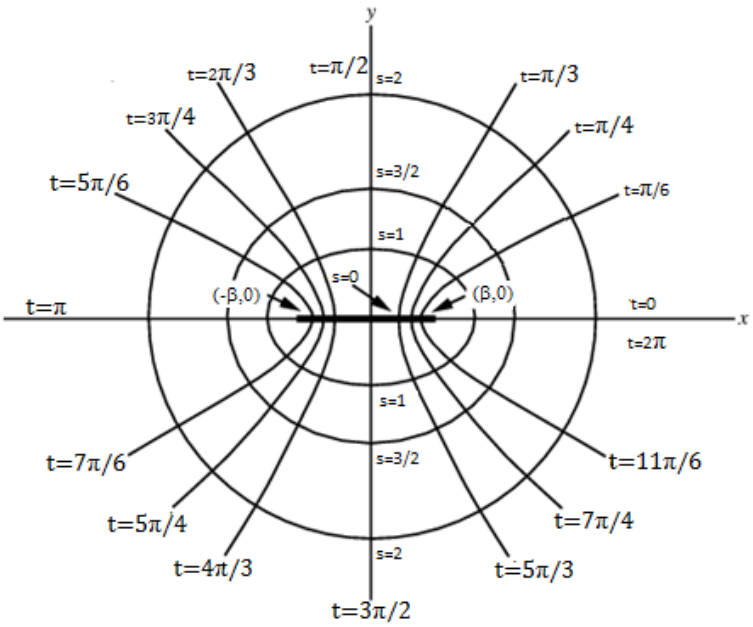

Figure 2.2: Elliptical coordinate system - (s, t) coordinates showing ellipses and hyperbolae for varying values of s and t - adapted from [42]

In terms of elliptical polar coordinates, the 2D Laplace equation becomes

$$\nabla^2 h(s,t) = \frac{1}{H^2}\left(\frac{\partial^2}{\partial s^2} + \frac{\partial^2}{\partial t^2}\right) h(s,t) = 0 \tag{2.9}$$

where

$$H = \beta\sqrt{\sinh^2 s + \sin^2 t} \tag{2.10}$$

The general solution to Equation 2.9 is

$$h(s,t) = C + A_0\frac{s}{s_0} + \sum_{m>0} e^{-m(s-s_0)}\left[A_m\cos(mt) + B_m\sin(mt)\right] \tag{2.11}$$

where C is a constant, A_m and B_m are elliptic multipole moments with order m, and s_0 is approximately the s coordinate of the contact line. For an isolated cylinder in the side-on state $s_0 = \coth^{-1}(\alpha)$ and $\beta = \sqrt{2}r\sqrt{\alpha^2 - 1}$.[12] The lowest decaying mode is $m = 2$, as the particles are small enough that gravitational effects can be disregarded and there is no external force on the particles which would provide a torque. Therefore, the quadrupolar term is the first surviving term of the expansion in Equation 2.11. Due to symmetry, all sine moments are equal to zero i.e. $B_m = 0$; this is true if we align x and y along the semi-minor and semi-major axes respectively.[43] It is convenient to rewrite the leading order interface shape $h(s,t)$ as

$$h(s,t) = H_0 + H_e e^{-2(s-s_0)}\cos(2t) \tag{2.12}$$

where H_0 is the height of the unperturbed liquid interface (the constant term denoted as C in Equation 2.11), H_e (A_2 in Equation 2.11) is the amplitude of the interface at the ellipse $s = s_0$.[12]

For ellipsoidal or cylindrical particles in the side-on orientation there is no meniscus deformation for $\theta_w = 90°$, see Section 1.3. However, for $\theta_w \neq 90°$, the constant contact angle condition leads to contact line undulations and menis-

cus deformation. The lowest order multipole is given by Equation 2.12, where H_e is the amplitude of contact line undulation. Elliptical quadrupoles have been shown to represent effectively the interfacial deformation around anisotropic particles for distances larger than a few particle radii away from the particle surface, typically 3 radii.[12] Loudet et al. found this to be the case for ellipsoidal particles, see Chapter 1, Figure 1.3. For cylindrical particles Lewandowski et al. showed the characteristic quadrupolar deformation, Figure 2.3(a) which highlights the rise at the ends of a cylinder and the slight depression at the sides typical of a quadrupole. Figure 2.3(b) shows the interface fringes caused by the presence of the cylindrical particle at the interface, again with characteristic quadrupolar deformation. Closer to the particle surface,

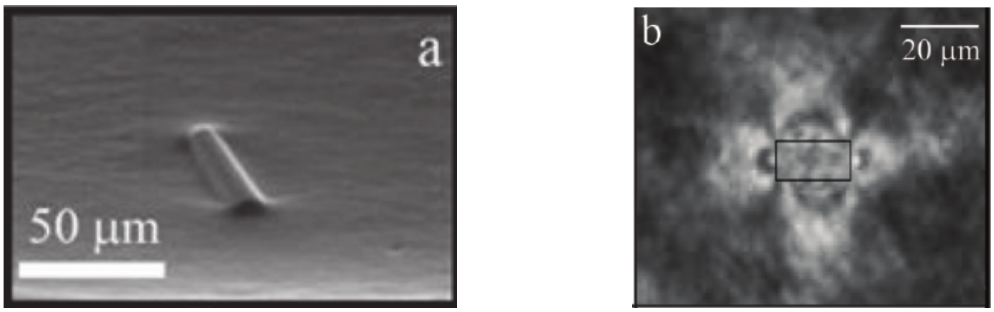

Figure 2.3: Experimental observations for a cylindrical particle (a) Scanning Electron Microscopy (SEM) image for a cylinder with $\alpha = 3$ (b) Interface fringes for a cylinder with $\alpha = 2.5$ and $\theta_w = 80 \pm 2°$.[12]

higher order modes start to contribute significantly to the deformation around the particle.[12]

2.2. Far Field Capillary Interactions

We next consider the interactions for multiple anisotropic particles approaching each other. We start by outlining the theory developed for nearly spherical

particles and show how this can be adapted for anisotropic particles.

Capillary forces arise between adsorbed particles when the deformed menisci of the two particles start to overlap.[7, 8] This is because the excess area caused by the deformed menisci changes as the particles approach each other; clearly greater menisci deformations produce stronger interactions.[44] For perfectly smooth spheres there are no capillary interactions because there is no deformation of the interface, see Chapter 1, Section 1.2. However, it has been shown that spheres in the nanometre to micrometre range can exhibit lateral capillary forces due to surface roughness.[45] Specifically, particles with rough surfaces, have irregular contact lines which cause the interface to deform and therefore lead to substantial capillary forces.

Stamou et al. developed the theory for the far field capillary interaction between nearly spherical particles.[41] When quadrupolar deformation fields from neighbouring particles overlap, the energy E associated with the interface is given by the product of the interfacial tension γ and the area of the liquid–liquid interface, which in the small slope limit is equal to

$$E \approx \gamma \int_A \left[1 + \frac{1}{2}\nabla h \cdot \nabla h\right] dxdy \tag{2.13}$$

where the second term inside the square bracket is the excess surface area due to the deformations h.

Far field interactions are understood by considering the overlap of disturbances h_A and h_B created by neighbouring particles A and B. In the superposition approximation, h_A and h_B are the distortions created by isolated particles and $h = h_A + h_B$.[46] The contribution to E that depends on the inter-particle

separation and orientation for the far field capillary interaction potential is

$$E_{AB} = \gamma \int \nabla h_A \cdot \nabla h_B dxdy \tag{2.14}$$

By inserting Equation 2.6 into 2.14, Stamou et al. [41] showed that for interacting polar quadrupoles, E_{AB} is given by

$$E_{AB} = -\gamma \frac{12 H_p^4 r_p^4}{r_{AB}^4} \cos(2\psi_A + 2\psi_B) \tag{2.15}$$

where r_{AB} is the centre-to-centre separation and ψ_A and ψ_B are the bond angles. In the very far field, the meniscus around anisotropic particles can be represented as polar quadrupoles and interact according to Equation 2.15. Theoretical investigations have found that capillary interactions between quadrupoles are attractive at long distances and repulsive at short distances.[43]

Although Equation 2.15 accurately describes the attractive force between ellipsoids and cylinders near contact, it does not explain the rotational behaviour observed in experiments. Equation 2.15 predicts quadrupole interaction minimised for $\psi_A = -\psi_B$ or $\psi_A = \pi - \psi_B$ independent of bond angle ψ_A. Therefore, it predicts the same energy when the positives face each other as for the negatives facing each other, see Figure 2.4. However, experiments on anisotropic particles show orientational dependence of pair interactions, with the side-to-side attraction being stronger than the tip-to-tip attraction, see Figure 2.4(b).[23, 36] This behaviour can be explained using elliptical quadrupoles because the interface distortion is more concentrated near the tips of the particle. Therefore, the capillary energy is smaller when the long-axis of

the quadrupoles is aligned because the tips are closer to each other, see Figure 2.4. Until Lehle et al. investigated the near field capillary interactions between ellipsoids, the pair interactions were not very well understood.[9] They investigated the capillary interactions for all distances between two ellipsoidal particles finding capillary interactions are absent for a contact angle of 90°. They solved the Laplace equation using elliptical coordinates to find a numerical solution for the meniscus deformation. Elliptical coordinates provide the most convenient solution because the curve around the particles is an ellipse. They showed that the side-to-side configuration represented a lower capillary energy state than the end-to-end configuration for ellipsoids in contact.[9] Therefore, this theory correctly explains experimental observations.[7]

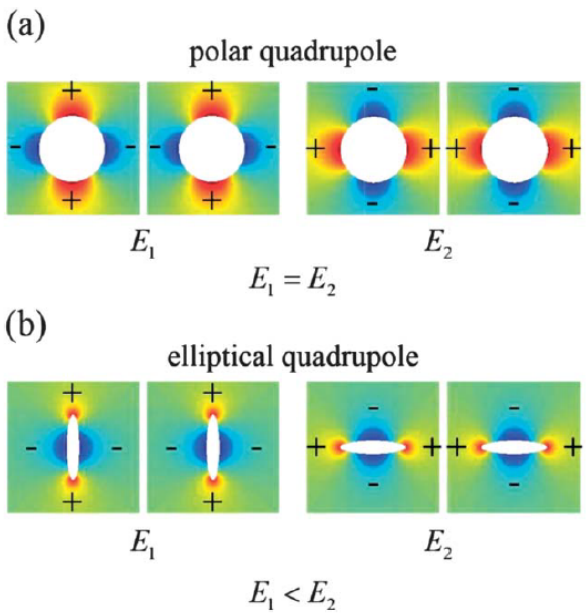

Figure 2.4: (a) Polar quadrupoles leave capillary energy unaltered by rotation (b) Elliptical quadrupoles predict a smaller capillary energy when the tips are closer together.[23]

2.3. Self-Assembly

The analysis of far field interactions is important for predicting particle trajectories towards self-assembly, but to understand the final microstructures formed we need to understand near field effects since these eventually become dominant when the particles aggregate.[23] The fact that shape may induce enough long range capillary interaction to cause orientated self-assembly has been demonstrated for anisotropic particles such as ellipsoids and cylinders.[7, 12]

Loudet et al. first looked at the behaviour of ellipsoidal particles, finding long ranged capillary interactions based purely on the shape of the particles, as the surface chemistry was similar to that of spheres. Because the ellipsoids were made by stretching spherical particles, they concluded that the interactions must be due to the shape.[7] Loudet et al. also looked at the effect of surface chemistry on the self-assembled structures of ellipsoids, finding silicon ellipsoids preferentially aligned side-to-side whereas polystyrene ellipsoids aligned tip-to-tip, Figure 2.5(a) and (b). If silicon ellipsoids approached tip-to-tip the particles were found to rearrange into their preferred side-to-side configuration after contact. These observations may be explained using surface charge. Specifically, uncharged ellipsoids prefer side-to-side chaining, Figure 2.5(a), whereas the charged polystyrene ellipsoids form flower-like structures tip-to-tip, Figure 2.5(b).[7] The attractions between these ellipsoids were found to be long ranged extending over distances multiple times the particle length.[7] They also found that the capillary attraction is several orders of magnitude greater than the thermal energy ($10^5 k_B T$). Quadrupolar deformation of the contact line was confirmed by a later study by Loudet and co-workers.[8] For

uncharged ellipsoidal particles that are relatively smooth, Botto et al. found that they tend to "roll" over each other into their desired structure i.e. to preferentially align side-side.[23]

Loudet et al.[36] further extended the understanding of ellipsoidal particles at interfaces by observing how a pair of prolate ellipsoids with different aspect ratios self-assemble. They found so called 'capillary arrows' where the particles self-assembled with an angle between their axes which form a strong dipolar structure which is explained through the near field characteristics of the capillary interactions of the particles, shown in Figure 2.5(c). Specifically, the authors suggest that the unequal particles 'feel' the side-to-side configuration as energetically unfavourable and the repulsion of this unfavoured state forces the particles into an arrow like structure.[36]

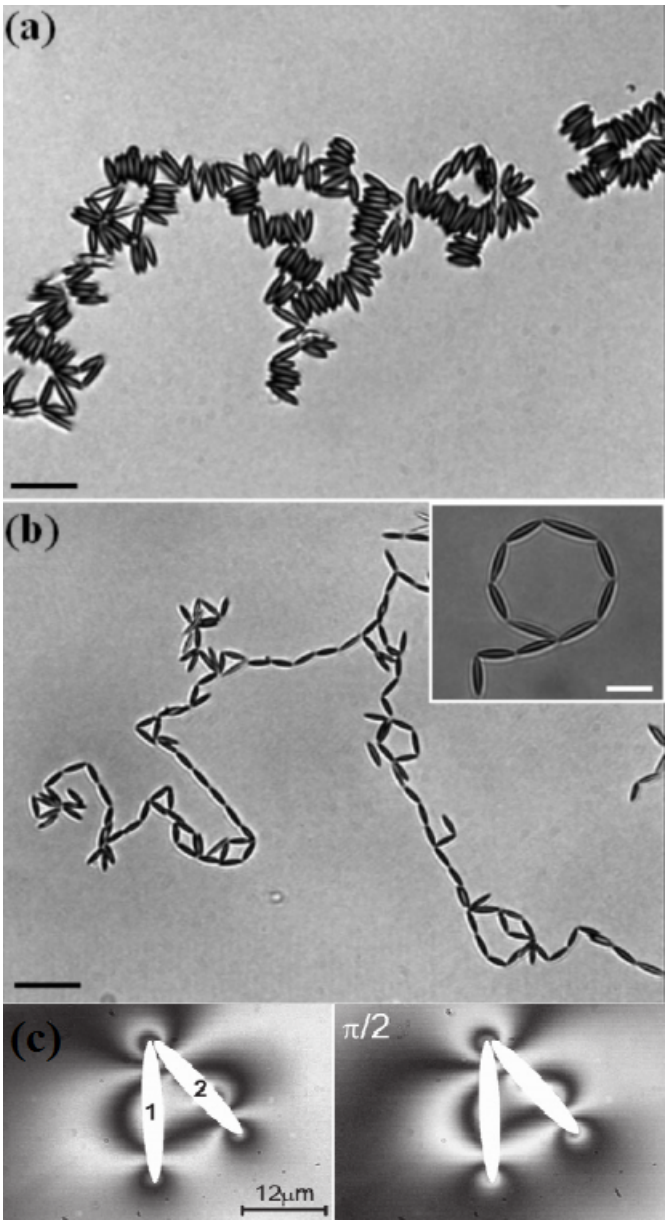

Figure 2.5: Optical microscopy image of ellipsoidal particles at a water-oil interface (a) silicon ellipsoids scale bar: $21\mu m$ (b) polystyrene ellipsoids scale bar: $33\mu m$ inset scale bar: $13.6\mu m$ (c) two ellipsoids with unequal length forming a capillary arrow scale bar: $12\mu m$[7, 36]

In the near field, the capillary energy landscape becomes strongly dependent on shape. Closer to contact, the aspect ratio becomes an important parameter, capillary torques become relatively strong and preferred orientations emerge, as predicted by the interaction potential for elliptical quadrupoles.[23] In contrast to ellipsoidal particles that are relatively smooth, cylindrical particles have

clearly defined edges, which are different at the sides to that at the ends. They prefer to "hinge" at the ends of the particle i.e. to preferentially align end-to-end, Figure 2.6. Lewandowski et al. and Botto et al. have shown using numerical simulations that close to the ends of a cylinder there is excess surface area. When particles approach each other these excess areas overlap causing a capillary bridge to form which creates an energy barrier for re-orientation, thus stabilising the end-to-end configuration.[12, 34]

(a) (b)

Figure 2.6: (a) Linear chain of microcylinders assembled by capillarity at the air–water interface [12] (b) Monolayer of microcylinders formed by compression after chain formation[23]

2.4. Orientation of Anisotropic Particles in Zero Field

Up to this point, we have only considered the behaviour of rod-like anisotropic particles when they are adsorbed in the side-on orientation, i.e. where the long axis is parallel to the interface. In fact, when rod-like anisotropic particles, such as ellipsoids and cylinders, adsorb at liquid interfaces, the particles can adopt multiple orientations relative to the liquid interface. In this section, we therefore consider the orientation of rod-like particles in the absence of an external field.

We first consider the impact of particle orientation on the deformation of the liquid meniscus around the particle. The deformation and position of the contact line is determined by the contact angle of the particles (we assume an oil/water interface for definiteness). In Figure 2.7 we consider an ellipsoidal particle in the two limiting orientations of end-on, shown in Figure 2.7(a) & (b) and side-on shown in 2.7(c). In the end-on state, Figure 2.7(a) & (b), it is possible to satisfy a constant contact angle condition with a flat interface for a contact angle $\theta_w = 90°$. The contact line is located at the equator of the particle i.e. the particle is equally wetted by the oil and water. For a contact angle $\theta_w \neq 90°$ the constant contact angle can be satisfied by changing the vertical position of the particle relative to the interface; this is illustrated in Figure 2.7(b) for a hydrophilic particle. Therefore, more of the particle is in the water phase rather than the oil. If we now consider the side-on state, it is possible to satisfy a constant contact angle condition with a flat interface for $\theta_w = 90°$, Figure 2.7(c). For $\theta_w \neq 90°$ there is contact line undulation as discussed in Chapter 1, Section 1.3.

In Figure 2.8 we consider a cylindrical particle in the two limiting orientations of end-on, shown in Figure 2.8(a) & (b) and side-on shown in 2.8(c). In the end-on state, Figure 2.8(a) it is possible to satisfy a constant contact angle condition with a flat interface for a contact angle $\theta_w = 90°$. The contact line is again located at the equator of the particle. For $\theta_w \neq 90°$ the constant contact angle can be satisfied by changing the vertical position of the particle relative to the interface; this is illustrated in Figure 2.8(b) for a hydrophilic particle. If we now consider the side-on state, it is possible to satisfy a constant contact

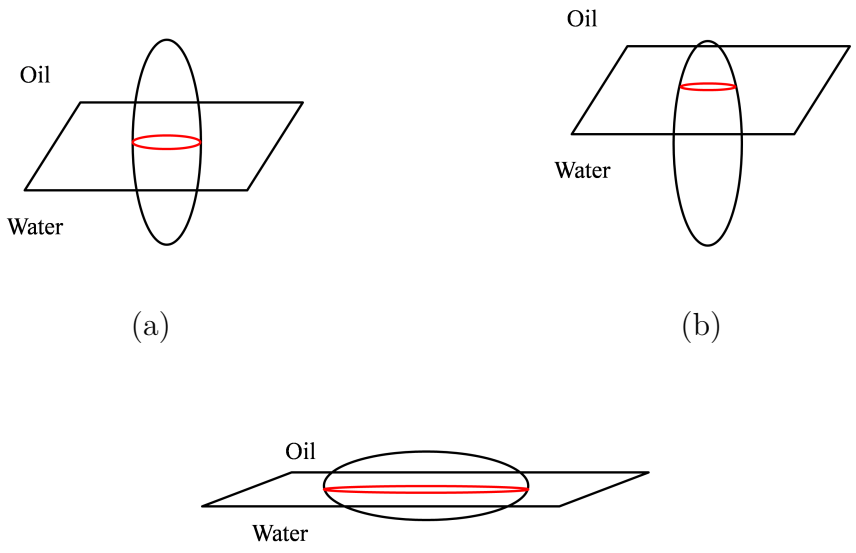

Figure 2.7: Ellipsoidal particles at an oil/water interface with contact line in each figure shown in red (a) End-on ellipsoidal particle with $\theta_w = 90°$ (b) End-on ellipsoidal particle with $\theta_w < 90°$ (c) side-on ellipsoidal particle with $\theta_w = 90°$.

angle condition with a flat interface for $\theta_w = 90°$, Figure 2.8(c). For $\theta_w \neq 90°$ there is contact line undulation as discussed in Chapter 1, Section 1.3.

Next we consider the equilibrium orientation in the absence of an external field. An equilibrium force balance can be satisfied in either orientation, with the energetically most favourable option being adopted i.e. the one with the lowest free energy. To a first approximation, the equilibrium orientation is the orientation that removes the maximum amount of the oil/water interface, see Chapter 1, Section 1.3. For ellipsoidal particles the side-on orientation is always the most stable orientation independent of aspect ratio, α, as this will always remove the largest amount of the oil/water interface. In fact end-on ellipsoids are not observed without the influence of an external field or under compression.[26, 47]

For cylindrical particles the orientation depends on aspect ratio α; this is because the area removed by the flat ends of the cylinder is constant and

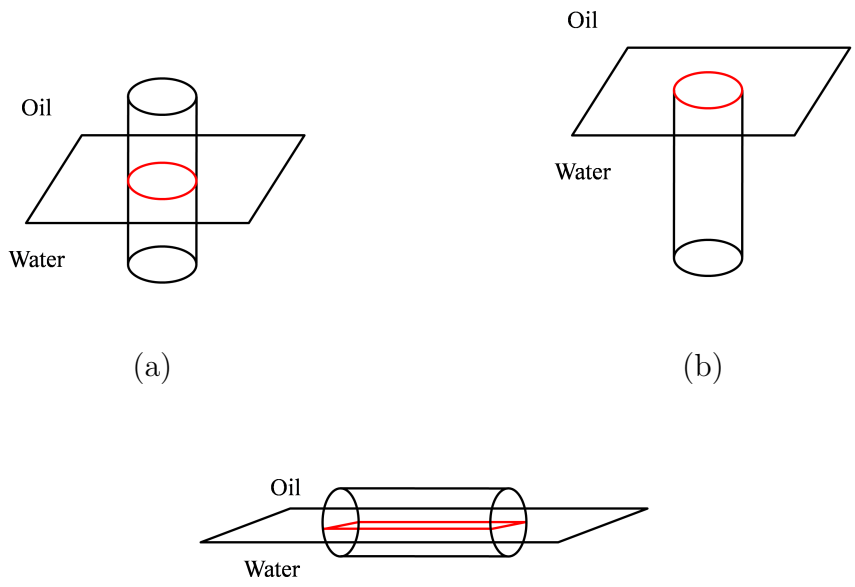

Figure 2.8: Cylindrical particles at an oil/water interface with contact line in each figure shown in red (a) end-on cylindrical particle with $\theta_w = 90°$ (b) end-on cylindrical particle with $\theta_w < 90°$ (c) side-on ellipsoidal particle with $\theta_w = 90°$.

independent of α i.e. for the end-on state. The area removed in the side-on state decreases with decreasing α. Therefore, for small enough α the end-on state becomes the most stable. The expression for the phase boundary between end-on and side-on state in the $\alpha - \theta_w$ plane is given by Lewandowski et al.[12] as

$$\alpha = \frac{\pi}{4} \frac{1}{\sin \theta_w}. \tag{2.16}$$

A phase diagram can be used to show preferred orientation; this was presented by Lewandowski et al. and is shown in Figure 2.9. The coexistence line (red dashed line), is where the cylinder can be orientated in either end-on/side-on configuration. The turning point at the bottom of the graph corresponds to an aspect ratio $\alpha = 1$ and a contact angle $\theta_w = 90°$.

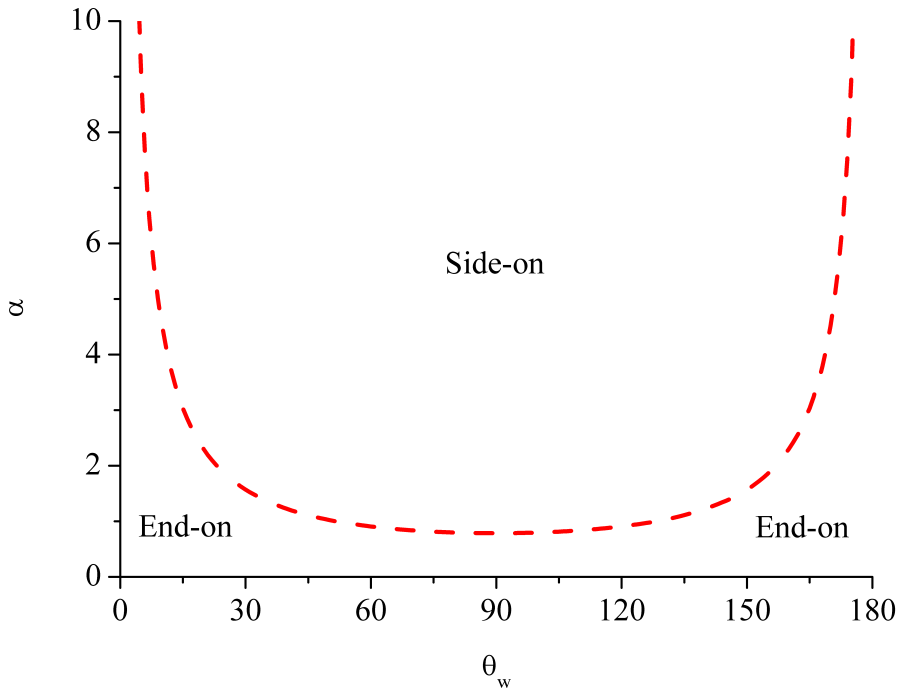

Figure 2.9: Phase diagram for an isolated cylindrical particle in the aspect ratio α contact angle θ_w plane.[12]

Lewandowski et al.[11] only considered end-on or side-on orientation in their analysis. In Chapter 5, we also consider intermediate orientations of cylinders between these two limiting orientations. We find the surprising result that tilted states are stable for homogeneous short cylinders.

Compressed ellipsoidal monolayers have been studied by Basavaraj et al. who found that the effect of surface pressure can produce some interesting results when the particles are compressed. For example, when the layer of ellipsoids was compressed some ellipsoids reorientated and flipped so that the long axis of the particle was then in the upright position; further compression resulted in some ellipsoids leaving the interface.[47] This work was then followed up by Madivala et al. who exploited the highly elastic monolayers of ellipsoids (much higher elasticity than if spherical particles were used) to create stable Pickering emulsions that could be tuned by changing the particle size

or concentration.[48, 49] The orientation of more complex anisotropic shapes has been investigated recently, see Chapter 1, Section 1.3. The most interesting of all of these was the prediction of higher order multipoles being the leading order for more complex anisotropic shapes rather than quadrupolar as seen for ellipsoids and cylinders. For example, the leading order distortion for cuboidal particles has recently been shown to be octupolar.[33] Anisotropic Janus particles have also been found to adopt tilted orientations as their equilibrium state is based purely on their surface chemistry.[16, 50, 51]

2.5. Orientation of Anisotropic Particles in an External Field

In the previous section, we showed that the favoured orientation for ellipsoids and cylinders depends on shape, aspect ratio and contact angle. In this section we outline the key literature results for anisotropic particles under the influence of an external field. It has been shown that by using an external field, it is possible to gain further control over the assembly of particles at liquid interfaces, opening up exciting opportunities for creating switchable surfaces.

Mittal et al.[52] have demonstrated the use of an alternating electric field on anisotropic nanoparticles. They used field and flow directed assembly to orientate ellipsoidal particles to create micrometre thick films of the particles with unique optical and mechanical properties and tuned particle orientation by changing the field frequency/strength.[52] Magnetic fields have been demonstrated to order ferromagnetic particles experimentally.[53, 54] Vandewalle et

al. demonstrated an ability to tune the equilibrium distance between soft ferromagnetic particles by varying the magnetic field and Lumay et al. induced periodic deformations of the assembly of ferromagnetic beads by adding a horizontal and oscillating magnetic field.[53, 54] Kimura et al. used a rotating magnetic field to create a uniaxial alignment of fibres, see Figure 2.10(a).[55] Snezhko et al. induced self-assembled asters by using a magnetic field which could be used to capture, transport and position target microparticles, see Figure 2.10(b).[56] Interfacial curvature can also be used as an external field to orientate anisotropic colloidal particles and has been demonstrated to induce assembly at preferred locations, see Figure 2.10(c).[27] Research has now extended into the use of anisotropic particles in liquid crystals, specifically, microbullets which are cylinders with one blunt end and one hemispherical end. They have been used to direct anisotropic particle orientation and assembly in nematic liquid crystals. The authors used an electrical field to orientate the dipoles to form two dimensional structures which offered new insights into the directed assembly of anisotropic particles.[14]

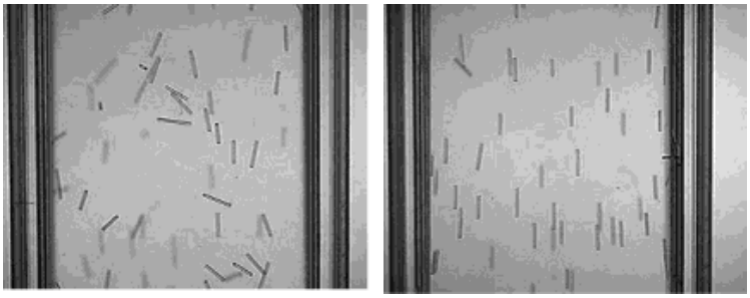

(a)

(b)

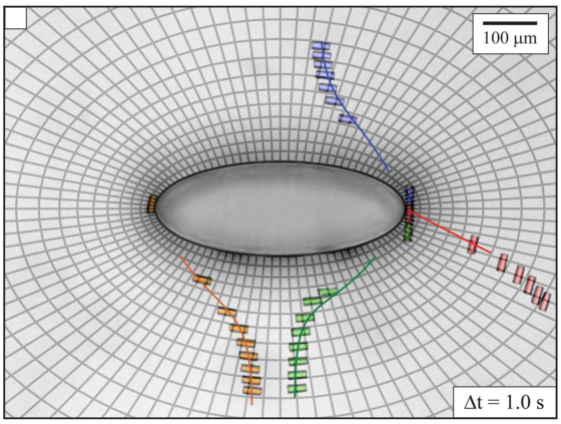

(c)

Figure 2.10: External field examples from the literature (a) fibres oriented randomly (left) alignment of fibres after exposure to static and rotating field (right) (b) Self-assembled asters [56] (c) Time lapsed images for four particles attaching to the interface (order of attachment red, green, blue and orange)[27].

In their seminal work, Bresme and co-workers[30, 57] analysed the effect of an external magnetic field on the orientation of a single ellipsoidal particle which has a semi-major axis of length z_m, two semi-minor axes of length r_m and aspect ratio $\alpha = z_m/r_m$. The ellipsoid has a permanent magnetic dipole, m, which is adsorbed at a liquid interface in the presence of a magnetic field, B, applied perpendicular to the interface, see Figure 2.11. They used a

simple thermodynamic model that assumes that the liquid interface remains planar and that the contact angle of the liquid interface at the particle surface is $\theta_w = 90°$ (we will refer to this theory as BF theory). For definiteness, we refer to the upper and lower liquid phases as oil and water, respectively. These authors found that at zero field strength the particle has a horizontal orientation (long axis of particle parallel to the interface). However, as the magnetic field, B, is increased, the tilt angle, θ_t, of the particle with respect to the interface gradually increases until, at a critical field strength, the particle undergoes a discontinuous phase transition to the vertical orientation (long axis of particle perpendicular to the interface). These authors also performed molecularly resolved computer simulations of nanoscale ellipsoids (roughly ten times larger than solvent molecules) and found *quantitative* agreement with BF theory across a wide range of field strengths and particle aspect ratios.[30, 57]

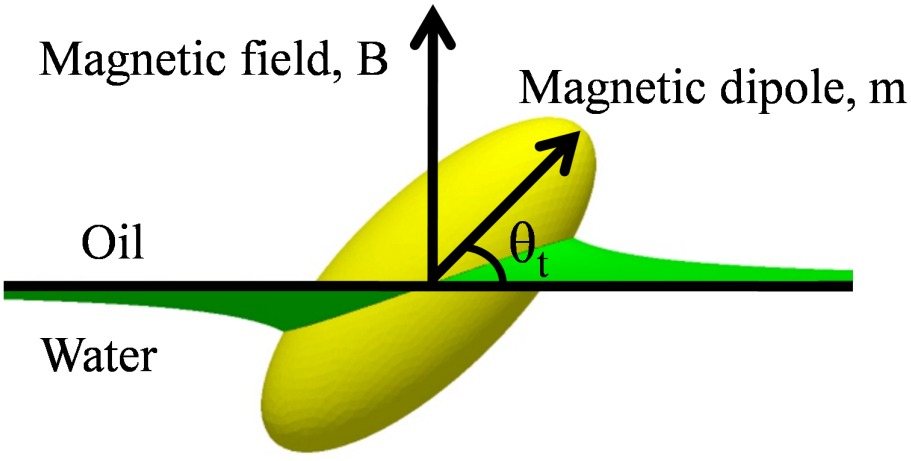

Figure 2.11: Geometry of an ellipsoidal particle adsorbed at an oil/water interface in the presence of an external field B applied perpendicular to the interface. The variables characterising the geometry of the tilted particle are discussed in the main text. The image is generated from Surface Evolver simulations of an ellipsoid with contact angle $\theta_w = 90°$, aspect ratio $\alpha = 3$ and tilt angle $\theta_t = 45°$, the deformation of the liquid meniscus has been taken into account.

However, as discussed in Chapter 1, Section 1.3, for a horizontal ellipsoidal particle with contact angle $\theta_w \neq 90°$, or a tilted ellipsoidal particle of any contact angle, Young's condition of a constant contact angle around the three phase contact line dictates that the liquid meniscus around the particle cannot remain flat. Instead, the liquid meniscus will be deformed with the amplitude of the deformation scaling with particle size. As can be seen from Figure 2.11 there is significant deformation of the interface caused by the tilting of the ellipsoid. The reason why the effect of such deformations was not observed in the simulations of Bresme et al.[30, 57] is presumably because for nano-particles, the amplitude of the capillary deformations is comparable to the thermal fluctuations of the liquid interface and therefore can be neglected to a first approximation. However, for micron-sized particles, where the amplitude of the capillary deformations is much greater than thermal fluctuations, we expect such deformations to lead to quantitative differences with BF theory.

Very recently, Davies et al. have studied this problem for micron-sized ellipsoidal particles with $\theta_w = 90°$ using lattice-Boltzmann simulations[32] which explicitly account for the deformation of the meniscus. These authors verified that ellipsoidal particles indeed undergo a discontinuous orientational transition with increasing magnetic field. However, they also found significant *quantitative* differences with BF theory and demonstrated that these differences are due to the deformation of the liquid meniscus.

Capillary deformation induced by tilting a particle has dipolar symmetry. The dipolar capillary interactions can be controlled by using an external field. Exploiting this fact, Davies et al. studied the effect of a magnetic field on

the self-assembly of multiple ellipsoids using lattice-Boltzmann simulations.[32] Their theoretical investigations have found switchable 'capillary caterpillars' (long chains of ellipsoidal particles in the side-to-side configuration) and have demonstrated, by applying a magnetic field, an ability to switch on and off dipolar capillary interactions, see Figure 2.12.[4] Specifically, in Figure 2.12(a) the initial configuration for side-on ellipsoids randomly distributed on an interface is shown. (b) demonstrates dipolar capillary interactions forming self-assembled chains when a magnetic field is applied perpendicular to the interface. (c) shows that once the critical field is exceeded all of the particles undergo a first order phase transition to the end-on state. Therefore, there is no deformation of the interface meaning no capillary interactions are present. Finally, (d) shows the particles randomly arranging after the first order phase transition. The authors suggested the ability to turn off and on the interactions leads to a potential use of them as switches e.g. interfacial sensors.[32]

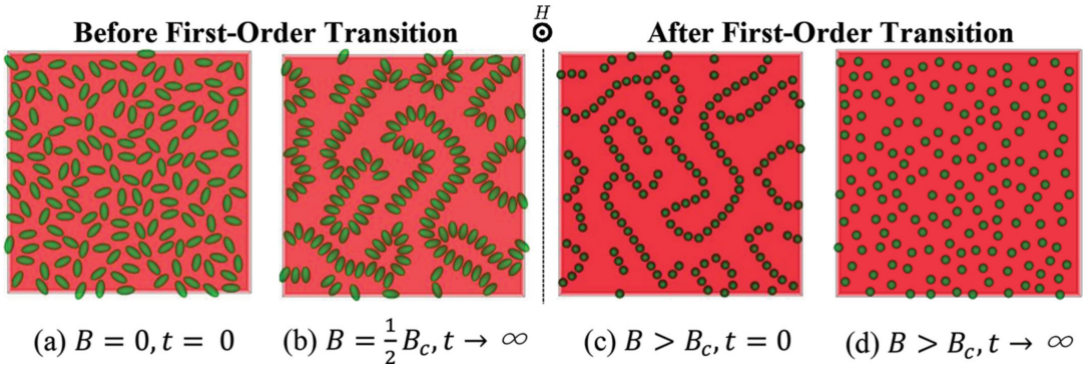

Figure 2.12: lattice-Boltzmann simulations for multiple ellipsoidal particles (a) randomly distributed ellipsoids in side-on orientation (b) self-assembled ellipsoids due to dipolar capillary interactions when a magnetic field is applied perpendicular to the interface (c) critical field exceeded therefore particles now in end-on orientation (d) randomly distributed end-on ellipsoids.[32]

Finally, Davies et al. followed up this work by investigating a small number of particles, under the influence of a magnetic field, finding interesting sym-

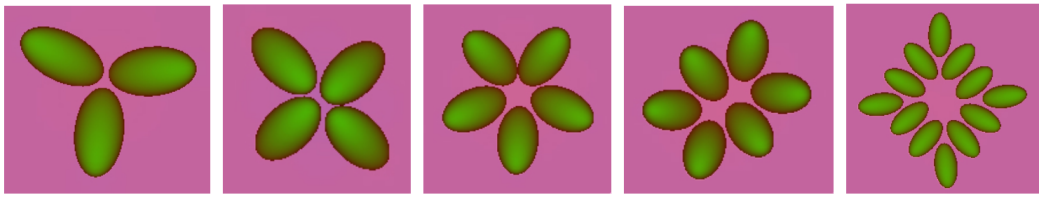

Figure 2.13: lattice-Boltzmann simulations for equilibrium clusters of ellipsoidal particles with aspect ratio $\alpha = 2$ and intermediate external field $B = 0.5B_c$. From left 3, 4, 5, 6 and 12 particles.[58]

metric clusters which appear to favour tip-to-tip configurations, see Figure 2.13.[58]

They also used Surface Evolver to analyse dipolar interactions for two ellipsoidal particles and found the side-to-side orientation to be a global minimum and the tip-to-tip orientation to be metastable, see Figure 2.14. This result seems counter intuitive since experimentally and theoretically it has been shown that side-on ellipsoids approaching tip-to-tip roll into a side-to-side orientation and will therefore be revisited in Chapter 6.[7, 34, 59]

In this thesis we focus on controlling the orientation and assembly of rod-like anisotropic particles using an external field in the geometry shown in Figure

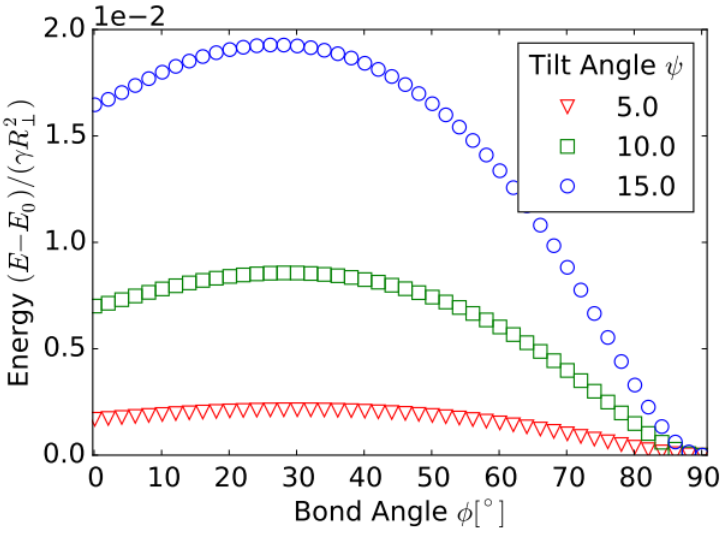

Figure 2.14: Energy profile as a function of bond angle for two ellipsoidal particle in contact with an $\alpha = 2$

2.11. One limitation of the lattice-Boltzmann method is the fact that the small degree of inherent noise present limits the resolution near the discontinuous transition, which is very sensitive to the presence of any fluctuations in the system. This is due to lattice-Boltzmann being based on a fixed Eulerian grid that does not allow for high accuracy in the evaluation of the area of the interface because of the requirement of a uniform surface mesh; the interface is typically ≈ 5 lattice sites wide at equilibrium.[4, 58] However, this method is beneficial for looking at large arrays of multiple particles at an interface.[32, 58] In order to overcome this problem, in Chapter 4, we use the finite element package Surface Evolver,[60] to analyse the region near the discontinuous transition of a single ellipsoidal particle much more accurately than previous studies. In Chapter 6, we use Surface Evolver to analyse the equilibrium configuration for a small number of ellipsoidal particles (up to three). The problem with ellipsoids is that any orientational transitions induced by an external field are lost when the external field is removed i.e. it is a volatile system. In order to overcome this, in Chapter 5, we analyse the orientation of cylinders in an external field. In the next Chapter we introduce Surface Evolver as the primary theoretical tool used to study these problems.

Chapter 3
Surface Evolver Method

In this Chapter we outline our simulation method which utilises the program Surface Evolver.[60, 61]

Surface Evolver is a finite element package designed as an interactive program for studying surfaces shaped by surface tension and other forces. All simulation results in this thesis have been performed using Surface Evolver which produces high resolution calculations due to the ability to have a finer mesh close to the particle and therefore, greater accuracy than other simulation methods.[60, 61]

3.1. Sphere at a Liquid Interface

To explain all of the stages required to create a Surface Evolver simulation we start by considering the relatively simple example of a sphere at a liquid interface.

The four basic elements used by Surface Evolver are vertices, edges, facets and bodies. Vertices are points in space represented by circles in Figure 3.1. Edges are straight lines joining pairs of vertices with their directions indicated by arrows, as shown. Facets are flat triangles bounded by three edges. A body is defined by the series of facets that bound it.

In our example, Surface Evolver divides the interface into a mesh of small triangles; the vertices of these triangles are then displaced to minimise the interfacial energy of the three-phase system. A typical set up for a spherical particle, with all the definitions required, is in Appendix A.

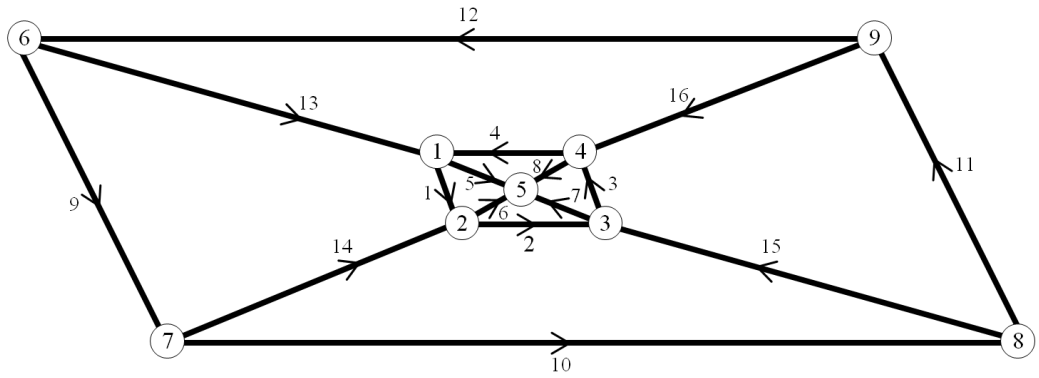

Figure 3.1: Example start point for a sphere geometry. The circled numbers are the vertices. The numbers next to the arrows are the edges and the arrows show the orientation of the edges which are used to define the facets.

In Surface Evolver the three phase contact angle, which is given by Young's equation, Equation 1.1, is implemented by using a constraint. The total free energy of the system, F_{int}, is given by

$$F_{int} = \gamma_{ow} A_{ow} + \gamma_{po} A_{po} + \gamma_{pw} A_{pw} \tag{3.1}$$

where γ_{ow},γ_{po},γ_{pw} are the interfacial tensions and A_{ow}, A_{po}, A_{pw} are the areas of the oil/water, particle/oil and particle/water interfaces respectively. Young's equation can be recast as $\gamma_{ow} \cos\theta_w + \gamma_{pw} = \gamma_{po}$, where θ_w is the contact angle. For the contact angle we need to specify two out of the three surface tensions; typically, $\gamma_{ow} = 1$ and $\gamma_{pw} = 0$. This sets $\gamma_{po} = \cos\theta_w$ which is implemented by applying the surface tension to the faces of the particle/oil interface on the contact line. For computational convenience and without loss of generality, the centre of the particle is fixed at the origin of the coordinate system used and the interface is free to move vertically to satisfy the contact angle.

As well as the contact line some other boundary conditions are required to correctly represent the particle at a liquid interface. The first is the three phase

contact line which requires an equation to represent the shape of the particle under investigation; in this case, the equation of a sphere

$$x^2 + y^2 + z^2 = r^2 \tag{3.2}$$

which is applied to the vertices $1-5$ and edges $1-8$ in Figure 3.1. x, y and z are the coordinates of the interface and r is the radius of the sphere. The homogeneous Neumann boundary condition is used at the outer boundary of the simulation domain to ensure a flat interface far from the particle.[12] This is where we apply a contact angle $\theta_w = 90°$ to vertices $6-9$ and edges $9-12$ in Figure 3.1.

Once all definitions are complete the file with the extension *.fe can be opened in Surface Evolver. Figure 3.2, shows the initial setup (a) evolving to the final minimised surface shown in (f).

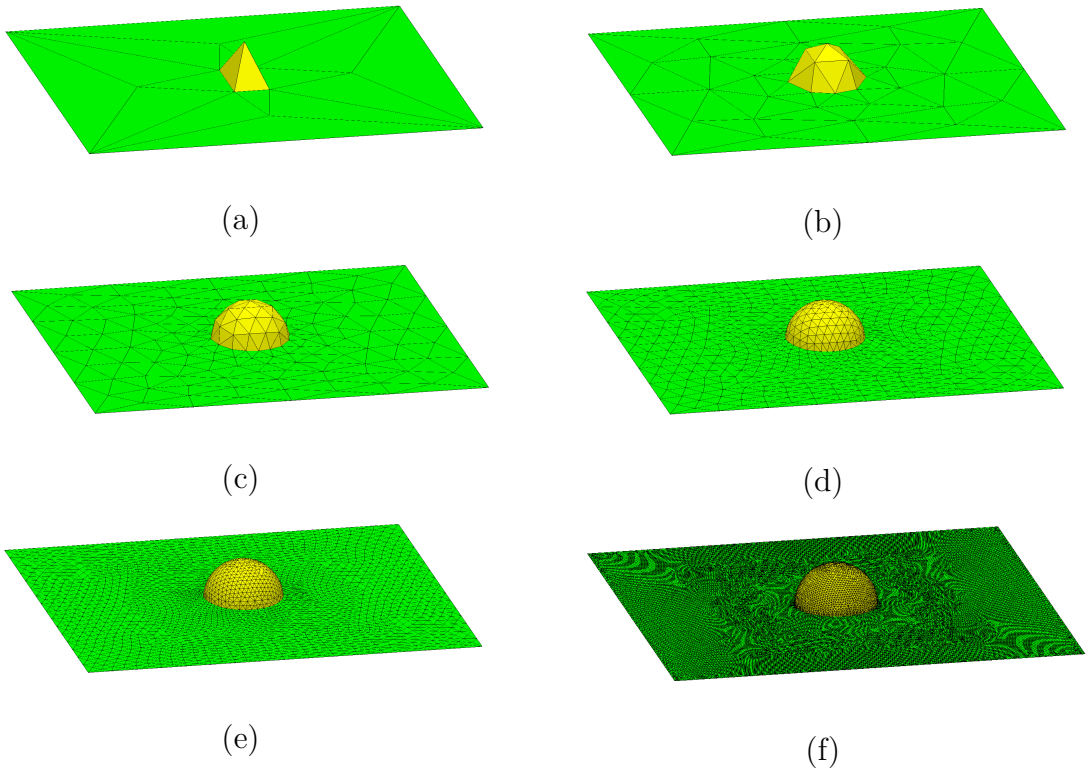

Figure 3.2: Evolution of a sphere as the surface is minimised.

For an isolated sphere with $\theta_w = 90°$ the interface remains flat and is at a height of $z = 0$. We can calculate from first principles the height of the interface for varying contact angle. Figure 3.3 shows the geometry we use to calculate the height of the interface.

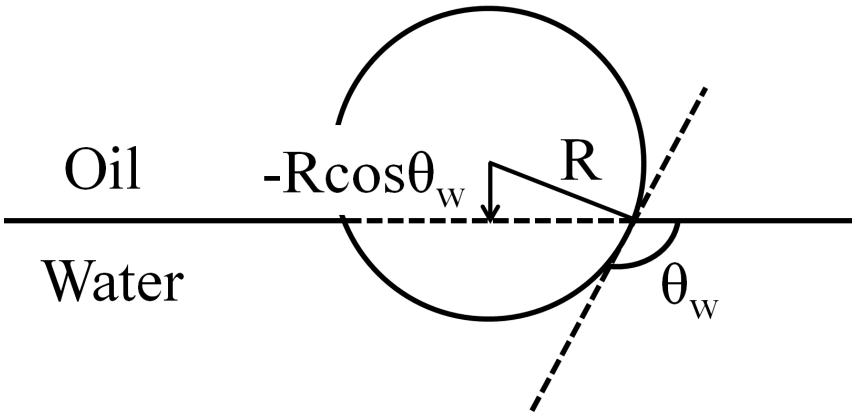

Figure 3.3: Spherical particle at an oil-water interface showing how to calculate the height of the interface for varying contact angle.

θ_w	$r\cos\theta_w$	Surface Evolver	Error/%
100	0.17365	0.17243	0.7
110	0.34202	0.34104	0.3
120	0.5000	0.49949	0.1
130	0.64279	0.64096	0.3

Table 3.1: Comparison of the interface height calculated using $r\cos\theta_w$ with the height predicted by Surface Evolver simulations including error.

In Table 3.1 we compare the height of the interface calculated for varying contact angle using $r\cos\theta_w$ with the height predicted by our Surface Evolver simulations shown in Figure 3.4. For all values there is a less than 1% error. Therefore, we have a simulation with a minimisation scheme that can predict very accurately the height of the interface. To calculate the height from our Surface Evolver simulation we outputted the 192 vertices on the contact line

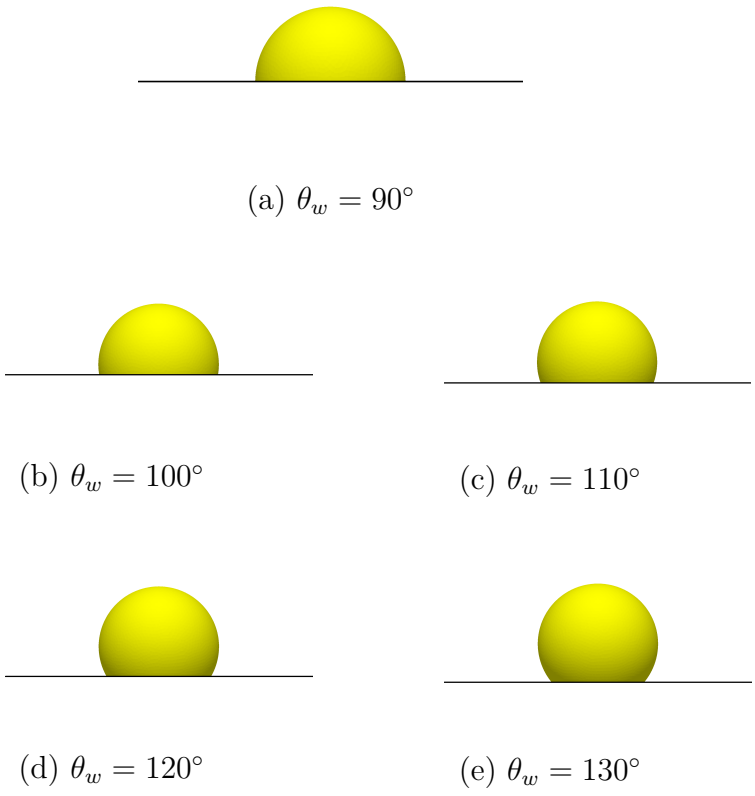

(a) $\theta_w = 90°$

(b) $\theta_w = 100°$

(c) $\theta_w = 110°$

(d) $\theta_w = 120°$

(e) $\theta_w = 130°$

Figure 3.4: Surface Evolver output for a sphere with varying contact angle.

and averaged the z values, shown in Table 3.1.

There are two ways of approaching simulating particles at an interface in Surface Evolver. The surface energy method, which we have shown here for the spherical particle case, is also used in Chapters 5 and 6. Whereas, the edge integral method is used in Chapter 4 in collaboration with Prof. Kenneth Brakke.[61] In the edge integral method, we omit the particle from the simulation and edges where the interface and particle would meet are represented by an energy integrand. Specifically, we use an ellipsoid area integrand that calculates strips from the contact line down to the south pole of the particle; this eliminates the need to explicitly include the particle/water or particle/oil interface. This is implemented by having a line integral as a constraint on the

edges where the interface would have met the ellipsoid. We have verified, for an ellipsoidal particle, that both methods produce the same results.

3.2. Coordinate Transformations

As described in Chapter 2, rod-like particles can have multiple orientations relative to the liquid interface. The most convenient way to implement this in a simulation is to use coordinate transformations that relate the local coordinate system aligned along the principle axis of the particle to the lab frame coordinate system aligned to the liquid interface.

If an anisotropic particle is tilted at an angle θ_t to the liquid-liquid interface an adaption of the mathematical formula, using the transform (x', y', z') to (x, y, z) , is required. To change (x', y', z') to (x, y, z) the following transformations will be used:-

$$x' = x$$

$$y' = y\cos\theta_t + z\sin\theta_t$$

$$z' = -y\sin\theta_t + z\cos\theta_t$$

The resulting equations are then inserted as constraints into the Surface Evolver program and the surface energies are minimised. In this thesis we investigate the effect of tilt angle on the orientational transition of a single ellipsoidal and a single cylindrical particle using this tilt angle transformation.

We also investigate the effect of tilt angle θ_t and bond angle θ_b on multiple ellipsoidal particles. In our case we apply the bond angle constraint first before tilting the particle. Specifically, in Figure 3.5 we show in (a) how we define the bond angle relative to the lab frame and in (b) how this is then used to

define both bond and tilt angles.

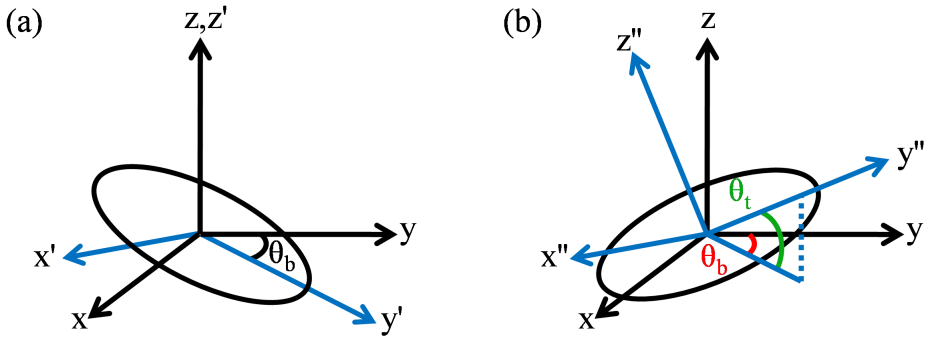

Figure 3.5: Schematic to show how the bond and tilt angle rotate in relation to the lab frame (x, y, z) (a) bond angle definition to the prime coordinate system (b) tilt angle definition to the double prime coordinate system.

The centre-to-centre distance required for multiple ellipsoidal particles, see Chapter 6 for details, is used in the definitions of the vertices and ellipsoid equations to ensure that the particles are always separated by the same amount for varying bond angle. In a similar way to the definitions outlined by Morris et al.[13] we apply the following transformations:-

$$x' = x\cos\theta_b + y\sin\theta_b$$

$$y' = -x\sin\theta_b + y\cos\theta_b$$

$$z' = z$$

$$x'' = x'$$

$$y'' = y'\cos\theta_t + z'\sin\theta_t$$

$$z'' = -y'\sin\theta_t + z'\cos\theta_t$$

3.3. Ellipsoids and Cylinders

In this section we compare our simulation with the data from published literature for anisotropic particles in the side-on orientation.

For an isolated ellipsoid with $\theta_w = 80°$ it has been reported that there is only weak contact line undulations with contact line heights z_{max} being the maximum and z_{min} being the minimum. In contrast, an isolated cylinder with the same contact angle gives a much stronger contact line undulation, around four times that of an ellipsoid. The comparison between literature and our Surface Evolver values are shown in Table 3.2 where $R = 1$.[34]

	α	$\triangle z = z_{max} - z_{min}$	Our Surface Evolver $\triangle z$	Error/%
Ellip	3	0.0674R	0.0669R	0.7
Ellip	2	0.042R	0.042R	0
Cyl	3	0.2574R	0.2580R	0.2

Table 3.2: Comparison between literature contact line height values and our Surface Evolver results.

In Figure 3.6 we show our Surface Evolver visualisation with the characteristic quadrupolar deformation observed around an ellipsoidal and a cylindrical particle. We have found excellent agreement between our Surface Evolver simulations and the literature.[34]

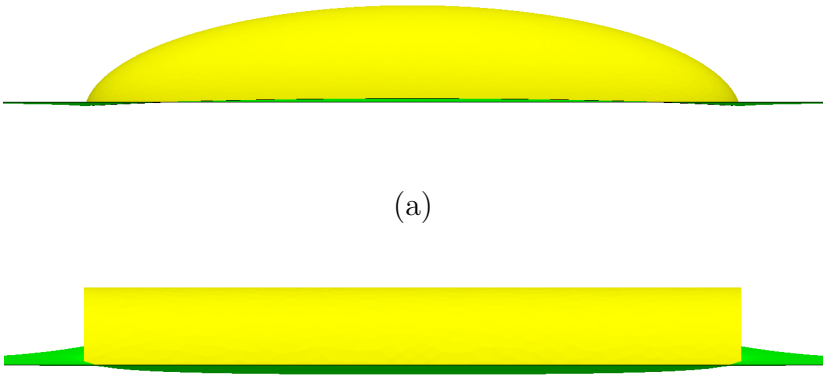

(a)

(b)

Figure 3.6: Surface Evolver visualisation for anisotropic particles with $\alpha = 3$ and $\theta_w = 80°$ (a) ellipsoidal particle and (b) cylindrical particle.

Chapter 4
Single Ellipsoid in an External Field

4.1. Introduction

In this Chapter, we investigate theoretically the effect of an external magnetic field on the orientation of a single ellipsoidal particle with a permanent magnetic dipole which is adsorbed at a liquid interface when the magnetic field is applied perpendicular to the interface. We compare our Surface Evolver results for varying aspect ratio with results from the literature and investigate the effect of changing contact angle.

Referring back to the seminal work of Bresme and Faraudo[30] and Bresme[57] (BF theory) who assumed that the liquid interface remains planar around an ellipsoidal particle with an embedded magnetic dipole that interacts with an external magnetic field applied perpendicular to the interface and $\theta_w = 90°$, see Chapter 2. They found that the initial orientation of the particle is with the long axis of the particle parallel to the interface. However, as the magnetic field is increased, the tilt angle of the particle with respect to the interface gradually increases until, at a critical field strength, the particle undergoes a discontinuous phase transition so that the long axis of the particle is now perpendicular to the interface. For micron-sized particles, where the amplitude of the capillary deformations is much greater than thermal fluctuations, we expect deformations to lead to quantitative differences with BF theory and this was confirmed by Davies et al. using lattice-Boltzmann simulations[32] which explicitly account for the deformation of the meniscus. These authors verified that ellipsoidal particles indeed undergo a discontinuous orientational

transition with increasing magnetic field. However, they also found significant *quantitative* differences with BF theory and demonstrated that these differences are due to the deformation of the liquid meniscus.

One limitation of the lattice-Boltzmann method is the fact that the small degree of inherent noise present limits the resolution near the discontinuous transition, which is very sensitive to the presence of any fluctuations in the system. In order to overcome this problem, we use the finite element package Surface Evolver,[60] which allows us to calculate the equilibrium meniscus around micron-sized particles and analyse the region near the discontinuous transition much more accurately. We also show for the first time that upon reducing the external field, the particle undergoes a second discontinuous transition from the perpendicular orientation to a different tilted state, i.e., we demonstrate that the tilt angle vs. magnetic field curve exhibits a hysteretic behaviour. Furthermore, we extend the studies in ref.[30, 32, 57] by considering particles with contact angles $\theta_w \neq 90°$, thus allowing us to study the effect of both particle aspect ratio and contact angle on the orientational transition.

The rest of this Chapter is organised as follows. In section 4.2 we discuss the theoretical model describing our Surface Evolver method and defining the key equations and boundary conditions for our simulation. In section 4.3 we present our results and discuss the feasibility of observing orientational transitions experimentally in these systems, and finally in section 4.4 we summarise our main conclusions.

4.2. Theoretical Model

When particles are adsorbed at an interface, the most stable configuration for the particle is the one that removes the maximum area of the liquid interface.[30] This is why, in the absence of an external field, the most stable configuration for an ellipsoidal particle is where the long axis of the particle is parallel to the interface (parallel configuration). This point is obvious if we make the simplifying assumption that the interface around the ellipsoid remains flat [30, 57] but is in fact also true even if we allow for deformations of the liquid interface. Conversely, configurations where the long axis of the particle makes a finite angle to the interface are only stable in the presence of an external field. Let us consider a prolate ellipsoidal magnetic particle adsorbed at a liquid interface, which has a semi-major axis of length z_m, two semi-minor axes of length r_m, aspect ratio $\alpha = z_m/r_m$ and whose long axis makes an angle θ_t with respect to the unperturbed liquid interface (Figure 4.1). For definiteness, we refer to the upper and lower liquid phases as oil and water respectively. The particle has an embedded magnetic dipole moment m which interacts with an external magnetic field B applied perpendicular to the liquid interface as shown in Figure 4.1.

The total free energy of this three phase system is given by

$$F_{int} = \gamma_{ow}A_{ow} + \gamma_{po}A_{po} + \gamma_{pw}A_{pw} - mB\sin\theta_t \tag{4.1}$$

where γ_{ow},γ_{po},γ_{pw} are the interfacial tensions and A_{ow}, A_{po}, A_{pw} are the areas of the oil/water, particle/oil and particle/water interfaces respectively. Using

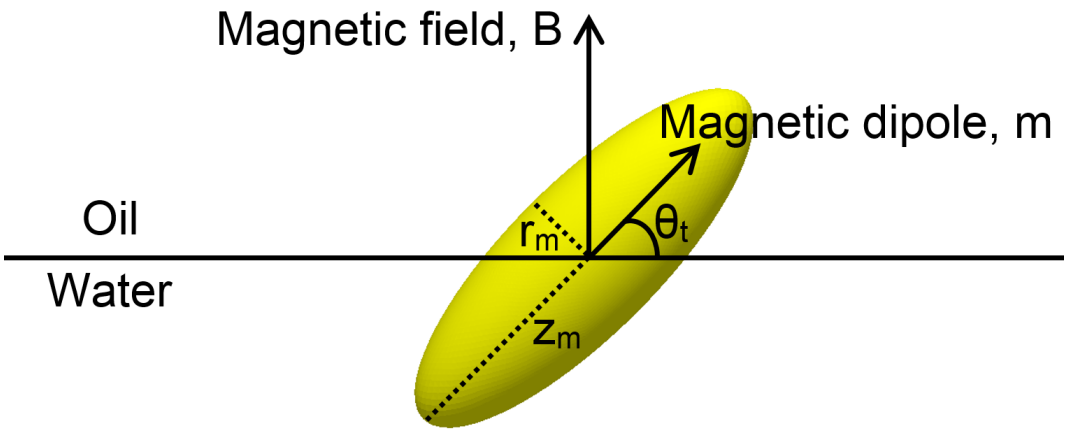

Figure 4.1: Geometry of an ellipsoidal particle adsorbed at an oil/water interface in the presence of an external field B applied perpendicular to the interface (for simplicity we show the unperturbed interface). The variables characterising the geometry of the tilted particle are discussed in the main text.

Young's equation $\gamma_{ow}\cos\theta_w = \gamma_{po} - \gamma_{pw}$ where θ_w is the contact angle of the oil/water interface at the particle surface, noting that $A_{po} = A_p - A_{pw}$, where A_p is the total area of the particle and dropping irrelevant constant terms, we can simplify Equation 4.1 to

$$F_{int} = \gamma_{ow}A_{ow} - \gamma_{ow}\cos\theta_w A_{pw} - mB\sin\theta_t. \tag{4.2}$$

Finally, it is convenient to divide the above equation through by $\gamma_{ow}A_p$ to obtain the dimensionless free energy of the system as

$$\overline{F}_{int} \equiv \frac{F_{int}}{\gamma_{ow}A_p} = \overline{A}_{ow} - \cos\theta_w\overline{A}_{pw} - \overline{B}\sin\theta_t \tag{4.3}$$

where $\overline{A}_{ow} = A_{ow}/A_p$, $\overline{A}_{pw} = A_{pw}/A_p$ and $\overline{B} = mB/\gamma_{ow}A_p$.

Minimising $\overline{F}_{int}$ with respect to θ_t for a given value of $\overline{B}$ allows us to determine the equilibrium tilt angle of the particle for a given magnetic field strength. Note that minimising $\overline{F}_{int}$ is equivalent to solving the equation

$$\frac{1}{\cos\theta_t}\frac{\partial \overline{F}_{st}}{\partial \theta_t} = \overline{B} \tag{4.4}$$

where

$$\overline{F}_{st} = \overline{A}_{ow} - \cos\theta_w \overline{A}_{pw} \tag{4.5}$$

is the free energy contribution from the interfacial tension terms. Note that the left hand side of Equation 4.4 is independent of $\overline{B}$. Thus, by calculating the interfacial energy $\overline{F}_{st}$ and $\frac{\partial \overline{F}_{st}}{\partial \theta_t}$ as a function of θ_t, we can determine the equilibrium tilt angle for a given $\overline{B}$ via Equation 4.4.

In order to calculate $\overline{F}_{st}$, Bresme and Faraudo[30] made the simplifying assumption that the oil/water interface remains flat in the presence of the adsorbed particle. This allowed them to derive an analytical expression for $\overline{A}_{ow}$ which is given by

$$\overline{A}_{ow} = \frac{A_0}{A_p} - \frac{\alpha}{4G(\alpha)}\sqrt{\frac{1}{\cos^2(\theta_t) + \alpha^2\sin^2(\theta_t)}} \tag{4.6}$$

where A_0 is the total area of the unperturbed oil/water interface in the absence of the adsorbed particle and

$$G(\alpha) = \frac{1}{2} + \frac{1}{2}\frac{\alpha}{\sqrt{1-\alpha^{-2}}}\arcsin\sqrt{1-\alpha^{-2}}. \tag{4.7}$$

Bresme and Faraudo further simplified the problem by considering the neutrally wetting case (i.e., $\theta_w = 90^\circ$) where the $\overline{A}_{pw}$ term in Equation 4.5 can be neglected. The BF theory predicts a discontinuous transition of the ellipsoidal particle from a finite tilt angle to the perpendicular orientation ($\theta_t = 90^\circ$) at a critical field strength. The theory also predicts that the critical field strength

increases with increasing particle aspect ratio α.

In our study, we calculate both $\overline{A}_{ow}$ and $\overline{A}_{pw}$ numerically using Surface Evolver.[60] This allows us to accurately account for the interfacial deformations caused when analysing the orientational transitions of the particle. Our Surface Evolver model is a finite element method that divides the oil/water interface into a mesh of small triangles; the vertices of these triangles are then displaced to minimise the interfacial energy of the three-phase system. This means that thermal fluctuations are neglected in Surface Evolver. Because of this, the method is accurate for modelling micron-sized particles, where thermal fluctuations are small compared to the amplitude of the meniscus deformation, but is less accurate for modelling nano-sized particles, where thermal fluctuations are comparable to the amplitude of the meniscus deformation. We define the x-y plane to lie along the unperturbed oil-water interface, the z axis to be perpendicular to the interface and work in length units such that the semi-minor axis length of the particle $r_m = 1$. In the physical system, the oil/water interface is fixed while the height of the particle relative to the interface is variable depending on the contact angle θ_w. In our simulations this fact is implemented by fixing the centre of the particle at the centre of the simulation cell but allowing the height of the oil/water interface to freely vary relative to the particle, which is equivalent to the physical system. The long axis of the particle is constrained to lie in the y-z plane at an angle of θ_t with respect to the y-axis. We use a square simulation cell with side length $12 \times z_m$ and impose a fixed contact angle of $\theta_w = 90^\circ$ at the outer edge of the cell. In order to confirm that finite size constraints are negligible, for selec-

ted simulations, the simulation cell length was increased by 50% and yielded essentially the same results for the critical tilt angle (within 2%) and critical field strength (within 0.1%).

The contact angle constraint at the three-phase contact line is imposed by using the edge integral method where the surface integral A_{pw} is partially integrated and represented as a line integral, see Chapter 3, Section 3.1.[60] For convenience, all simulation constraints are first represented in the particle reference frame (i.e., with coordinate axes aligned along the major and minor axes of the particle) before being transformed to the x-y-z frame via a coordinate transformation, details provided in Chapter 3, Section 3.2.[62, 63] In order to achieve good numerical accuracy, we used a high level of refinement for the oil/water surface, e.g., for particles with an aspect ratio $\alpha = 3$, contact angle $\theta_w = 90^\circ$ and tilt angle $\theta_t = 45^\circ$, we used 22500 triangles to represent the surface and 172 vertices to represent the contact line; the specific number of triangles and vertices used was varied depending on the values of α, θ_w and θ_t. The minimum-energy surface was found for tilt angles between 0° and 90° in increments of 1°. For each tilt angle, we record the location of the contact line and calculate A_{ow}, A_{pw} and hence $\overline{F}_{st}$ as a function of θ_t. The derivative $\frac{\partial \overline{F}_{st}}{\partial \theta_t}$ in Equation 4.4 was then calculated numerically for each simulated tilt angle using the central-difference formula;[64] values of the derivative at other tilt angles were obtained by interpolation.

4.3. Results & Discussion

We first consider the equilibrium orientation of the ellipsoidal particle as we increase the external field. In Figure 4.2, we plot the total free energy $\overline{F}_{int}$ given by Equation 4.3 (relative to the free energy at $\theta_t = 90°$) as a function of particle tilt angle θ_t for different field strengths $\overline{B}$ for a particle with aspect ratio $\alpha = 3$ and contact angle $\theta_w = 90°$. Figure 4.2(a) and (b) have been calculated using Surface Evolver and BF theory respectively. For each field strength, the equilibrium tilt angle is the one that minimises the total free energy. For both theories, we see that at zero field, the equilibrium configuration is the 'parallel' state where $\theta_t = 0°$ (black curves).

As we increase the field strength, the equilibrium state becomes the tilted state where the particle has a finite tilt angle that lies between $0° < \theta_t < 90°$ (e.g., blue curves). As we increase the field strength further, the free energy curve develops two local minima, one corresponding to the tilted state and the other to the perpendicular state, where $\theta_t = 90°$, but the equilibrium state (i.e., global minimum) is still the tilted state. However, at a threshold field strength $\overline{B}_0$, the free energy of the tilted state becomes equal to that of the perpendicular state (red curve). At this point, the particle *in principle* undergoes a first order phase transition from the tilted state to the perpendicular state. However, as first order phase transitions are activated processes, whether this transition can occur *in practice* depends on the magnitude of the energy barrier between the two local minima relative to the thermal energy k_BT. For nano-sized particles, where the energy barrier is of the order of k_BT, the first order phase transition can occur and evidence for such a transition

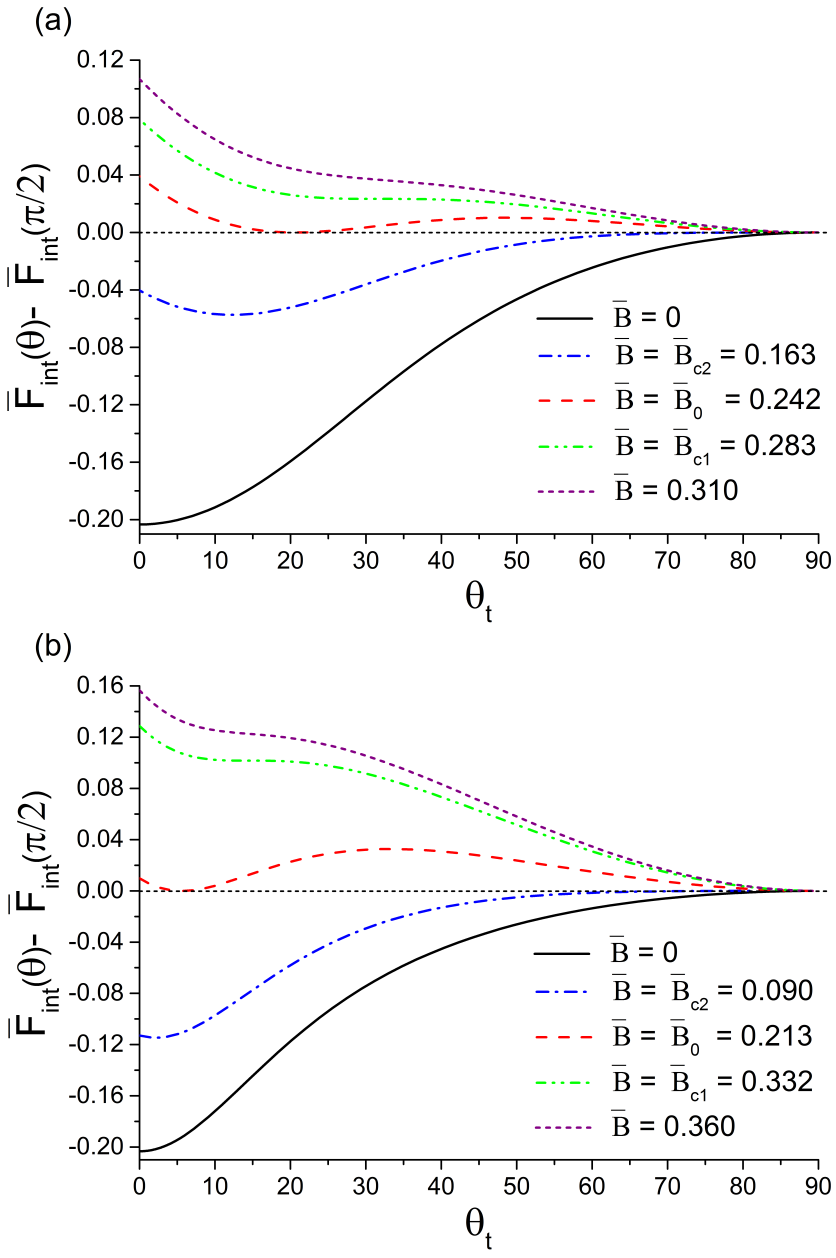

Figure 4.2: Dimensionless free energy as a function of tilt angle (relative to perpendicular state) for an ellipsoidal particle with $\alpha = 3$, $\theta_w = 90°$ for different field strengths: (a) Surface Evolver results (b) Bresme-Faraudo theory.

has been found in computer simulations of ellipsoidal nanoparticles.[30, 57] On the other hand for micron-sized particles, where the energy barrier is in general thousands of k_BT or more, thermal energy is insufficient to activate the first order phase transition and the particle remains trapped in the tilted state for $\overline{B} > \overline{B}_0$, even though the tilted state is no longer the equilibrium state (i.e., it is a metastable state). Finally, as we increase the field strength further, at a critical field $\overline{B}_{c1}$, the local minimum corresponding to the tilted state merges with the local maximum corresponding to the free energy barrier at the critical tilt angle θ_{c1} (green curve). At this point, the energy barrier disappears and the particle undergoes an irreversible transition from the tilted state to the perpendicular state.

Comparing Figures 4.2(a) and (b), we see that both Surface Evolver and BF predict the same qualitative features for the orientational transition. However, there are clearly significant *quantitative* differences between Surface Evolver and BF theory. These differences are illustrated more clearly in Figure 4.3 where we plot the equilibrium tilt angle θ_t as a function of the external field $\overline{B}$ for increasing fields for $\theta_w = 90^\circ$ and $\alpha = 1.5$ or $\alpha = 3$. Specifically, we compare the results for Surface Evolver, BF theory and the recent lattice-Boltzmann simulations of Davies et al.,[32] which explicitly account for the deformation of the liquid meniscus around the particle. Comparing Surface Evolver and BF theory, we see that both theories agree qualitatively and predict that the particle undergoes a discontinuous orientation transition above a critical field strength. However, there are clearly significant quantitative differences between BF theory and Surface Evolver. For example, for $\alpha = 1.5$,

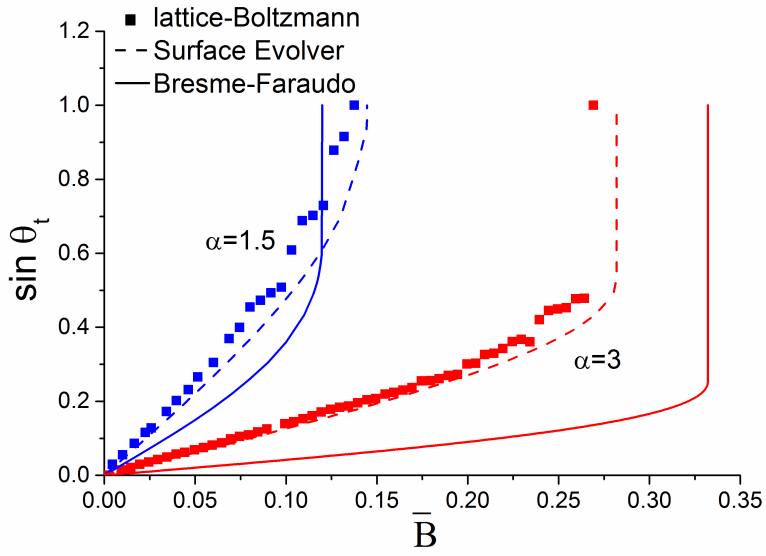

Figure 4.3: Equilibrium tilt angle as a function of dimensionless field strength for increasing fields calculated using Bresme-Faraudo theory (solid line), Surface Evolver (dashed line) and lattice-Boltzmann simulations[32] (points) for a contact angle $\theta_w = 90°$ and two different aspect ratios $\alpha = 1.5$ (blue) and $\alpha = 3$ (red).

Surface Evolver predicts a larger critical field $\overline{B}_{c1}$ and a larger critical tilt angle θ_{c1} compared to BF theory, while for $\alpha = 3$, Surface Evolver predicts a smaller critical field and larger critical tilt angle compared to BF theory. The results of Figures 4.2 and 4.3 demonstrate that assuming a flat fluid interface allows us to capture the essential *qualitative* features of the orientational transition. However, if we want to obtain *quantitative* results for the orientational behaviour of micron-sized anisotropic particles, we need to explicitly account for the deformation of the interface.

Next, we compare Surface Evolver with the lattice-Boltzmann simulations in Figure 4.3. We see that for both $\alpha = 1.5$, 3, there is excellent quantitative agreement between the two theories when we are far enough away from the orientational transition. However, discrepancies between the two theories begin to appear near the orientational transition where the lattice-Boltzmann results become noisy. We believe that these discrepancies are due to the small degree

of noise that is inherent in the lattice-Boltzmann method. While this noise does not have a significant effect when we are far enough away from the orientational transition, it has a big impact near the discontinuous transition, which is very sensitive to any fluctuations in the system. These results illustrate the necessity of very accurate numerics if we want to capture the behaviour near the orientational transition. In this context, Surface Evolver complements the lattice-Boltzmann scheme and allows us to analyse the region near the orientational transition to a much higher degree of resolution.

One very important feature for micron-sized particles that has not been discussed previously is the fact that the very large energy barrier between local minima states for such particles implies that there will be significant hysteresis in their orientational behaviour. This can be seen by analysing Figure 4.2(a) or (b) for the reverse case where we *decrease* the external field. For high external fields, the equilibrium state is the perpendicular state (e.g., purple curve). However, as we decrease the external field to less than $\overline{B}_{c1}$, the free energy curve develops two local minima, one corresponding to the perpendicular state and the other to the tilted state where $0^\circ < \theta_t < 90^\circ$, but the equilibrium state (i.e., global minimum) is still the perpendicular state. However, at the threshold field strength $\overline{B}_0$, the free energy of the tilted state becomes equal to that of the perpendicular state (red curve). At this point, the particle should undergo a first order phase transition from the perpendicular state to the tilted state. However, the very large energy barrier between the two states prevents the particle from doing so and it remains trapped in the (now metastable) perpendicular state for $\overline{B} < \overline{B}_0$. Finally, as we decrease the

field strength further, at a critical field $\overline{B}_{c2}$, the local maximum corresponding to the free energy barrier merges with the local minimum corresponding to the perpendicular state (blue curve). At this point, the energy barrier disappears and the particle undergoes an irreversible transition from the perpendicular state to the tilted state with tilt angle $\theta_{c2} < \theta_{c1}$. As can be seen from Figure 4.2(b), this second irreversible transition is also predicted by BF theory. However, as far as we are aware, the presence of hysteresis in the orientational transition of ellipsoidal magnetic particles at a liquid interface has not to date been discussed explicitly in the literature. We emphasise that we only expect such hysteretic behaviour to be seen for micron-sized particles, where the activation energy is large. For nano-sized particles, where the activation energy is small (order k_BT or less),[30, 57] we expect this hysteretic behaviour to disappear and the orientational transition to occur via an equilibrium first order transition.

Numerically, we have found that a convenient method for determining the equilibrium tilt angle, the critical fields $\overline{B}_{c1}$, $\overline{B}_{c2}$ and the critical tilt angles θ_{c1}, θ_{c2} is by solving Equation 4.4. This is illustrated in Figure 4.4, where we plot the curve $\frac{1}{\cos\theta_t}\frac{\partial \overline{F}_{st}}{\partial \theta_t}$ as a function of θ_t for $\alpha = 3$, $\theta_w = 90°$. For an arbitrary magnetic field $\overline{B}$, represented by the solid horizontal line in Figure 4.4, the intersection with the rising part of the curve represents the local minimum of the free energy curve corresponding to the tilted state; the value of θ_t at the intersection is therefore the equilibrium tilt angle. The intersection of the horizontal line with the falling part of the curve represents the local maximum of the free energy curve corresponding to the energy barrier (see Figure 4.2).

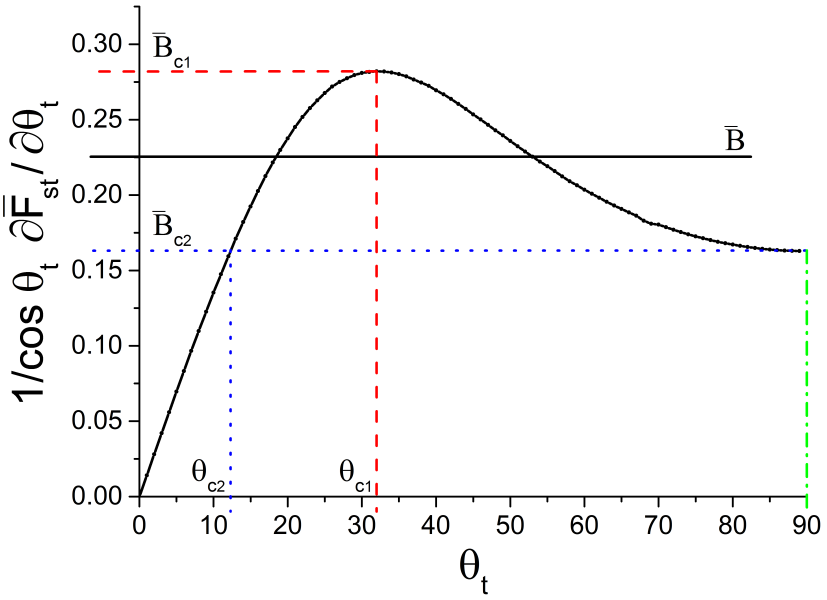

Figure 4.4: $\frac{1}{\cos\theta_t}\frac{\partial \overline{F}_{st}}{\partial \theta_t}$ as a function of tilt angle θ_t in radians ($\overline{F}_{st}$ is the dimensionless interfacial tension free energy of the system) for an ellipsoidal particle with $\alpha = 3$, $\theta_w = 90°$. The equilibrium tilt angle for a given external field $\overline{B}$ (represented by the solid horizontal line) is given by the intersection of the horizontal line with the rising part of the curve. The values of the critical fields and tilt angles can be determined from the curve as shown above.

The first irreversible transition occurs when the external field is such that the tilted state merges with the energy barrier which corresponds to the maximum of the curve in Figure 4.4. We can determine $\overline{B}_{c1}$ and θ_{c1} from the magnitude and position of the maximum, as shown in Figure 4.4. On the other hand, the second irreversible transition occurs when the external field is such that the energy barrier merges with the local minimum at $\theta_t = 90°$. We can therefore find $\overline{B}_{c2}$ from the value of the curve at $\theta_t = 90°$; the intersection of $\overline{B}_{c2}$ with the rising part of the curve then yields θ_{c2} as shown in Figure 4.4.

In Figure 4.5, we plot the equilibrium tilt angle as a function of magnetic field for both increasing fields (lower curve) and decreasing fields (upper curve) for $\alpha = 3$, $\theta_w = 90°$; (a) and (b) are calculated using Surface Evolver and BF theory respectively. The position of the irreversible orientational transitions

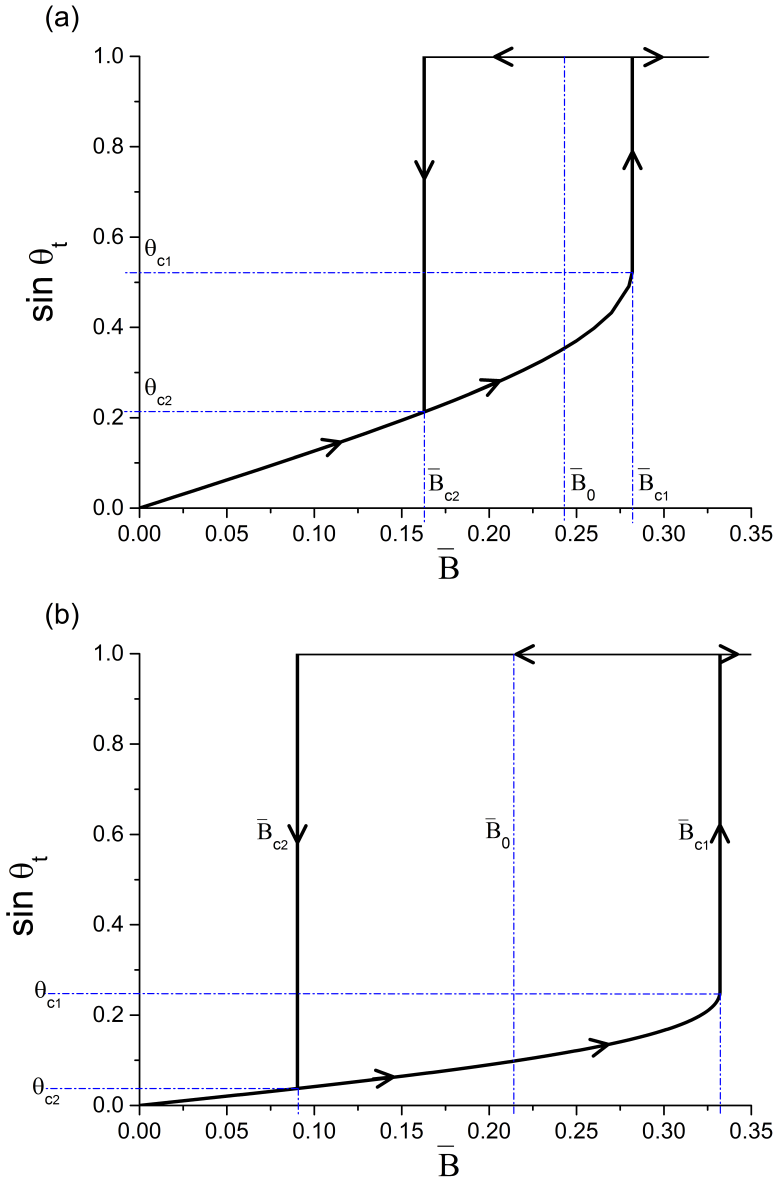

Figure 4.5: Hysteresis curve for the equilibrium tilt angle vs. dimensionless field strength for increasing and decreasing fields (as indicated by the direction of the arrows) for $\alpha = 3$, $\theta_w = 90°$ calculated using: (a) Surface Evolver (b) Bresme-Faraudo theory.

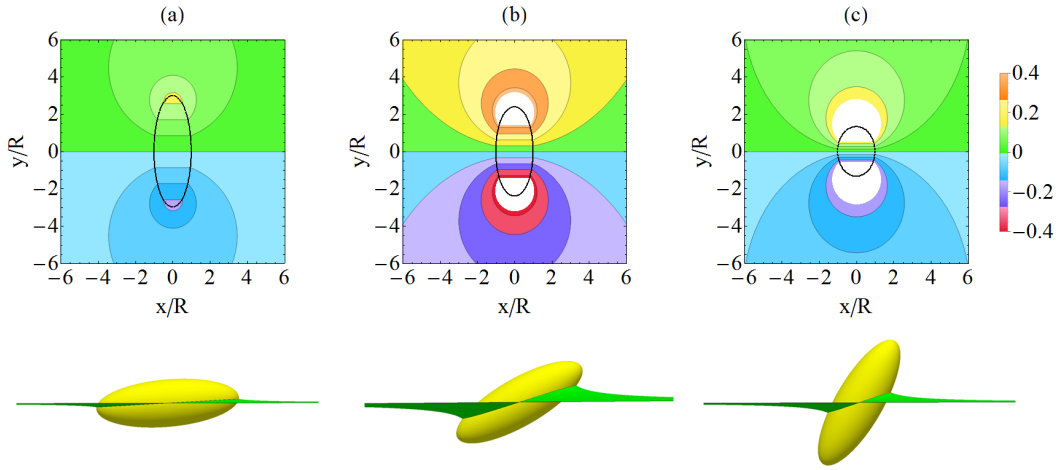

Figure 4.6: Contour plot (top) and 3D plot (bottom) of the deformation field for the oil/water interface calculated from Surface Evolver for three different tilt angles θ_t of a particle with $\alpha = 3$, $\theta_w = 90°$: (a)$\theta_t = 5°$ (b)$\theta_t = 30°$ (c)$\theta_t = 60°$.

at $\overline{B}_{c1}$ and $\overline{B}_{c2}$ are indicated on the plot. The position of the threshold field $\overline{B}_0$, where a reversible first order phase transition can occur (for particles with sufficiently large activation energy) is also indicated. Note that the lower curve is metastable for $\overline{B}_0 < \overline{B} < \overline{B}_{c1}$ while the upper curve is metastable for $\overline{B}_{c2} < \overline{B} < \overline{B}_0$. Once again we see that both Surface Evolver and BF theory agree qualitatively, predicting that there is a significant degree of hysteresis in the orientational transition of the particle. However, because of the different assumptions regarding the deformation of the meniscus, there are clearly significant quantitative differences between the two: firstly Surface Evolver predicts a much narrower hysteresis loop compared to BF theory; secondly the critical tilt angles predicted by Surface Evolver are significantly higher than the corresponding tilt angles predicted by BF theory.

Given the importance of the deformation of the liquid meniscus for quantitative calculations of the orientational transition,[32] it is instructive to analyse the deformation of the liquid meniscus around the particle as a function of the tilt angle using Surface Evolver. In Figure 4.6, we plot the deformation field

of the oil/water interface for a particle with $\alpha = 3$ and $\theta_w = 90°$ for some representative tilt angles as contour plots (top) and 3D plots (bottom); the solid oval outline in the contour plots represent the projection of the three-phase contour line onto the x-y plane. We have chosen a contact angle of $\theta_w = 90°$ for clarity since for this neutral wetting condition, any quadrupolar deformations due to contact angle constraints[7–9] are absent. The deformation field is clearly dipolar in nature, in agreement with the lattice-Boltzmann simulations of Davies et al.[32] We also note that the deformation is small for small (a) and large (c) tilt angles and is maximum for intermediate tilt angles (b). This is not surprising since (for $\theta_w = 90°$) the deformation is zero for $\theta_t = 0°$ and $90°$. Interestingly, the tilt angle at which the maximum deformation occurs ($\approx 30°$ in this case, i.e., case (b)) is essentially equal to θ_{c1}, the critical angle for the irreversible transition to the perpendicular state to occur. Qualitatively, this can be understood from the fact that the maximum deformation effectively corresponds to the maximum torque that can be generated by interfacial tension to oppose the magnetic torque. Increasing the tilt angle beyond this point leads to a further increase in the magnetic torque but a decrease in the interfacial tension torque and the particle therefore undergoes a discontinuous transition to the perpendicular state.

In Figure 4.7, we analyse the dependence of the critical fields and critical tilt angles on the aspect ratio of the particles α. Specifically, in Figure 4.7(a), we plot θ_{c1} and θ_{c2} as a function of α, while in Figure 4.7(b) we plot $\overline{B}_{c1}$ and $\overline{B}_{c2}$ as a function of α for $\theta_w = 90°$; the red lines are the predictions of Surface Evolver while the black lines are the predictions of BF theory. We see that BF

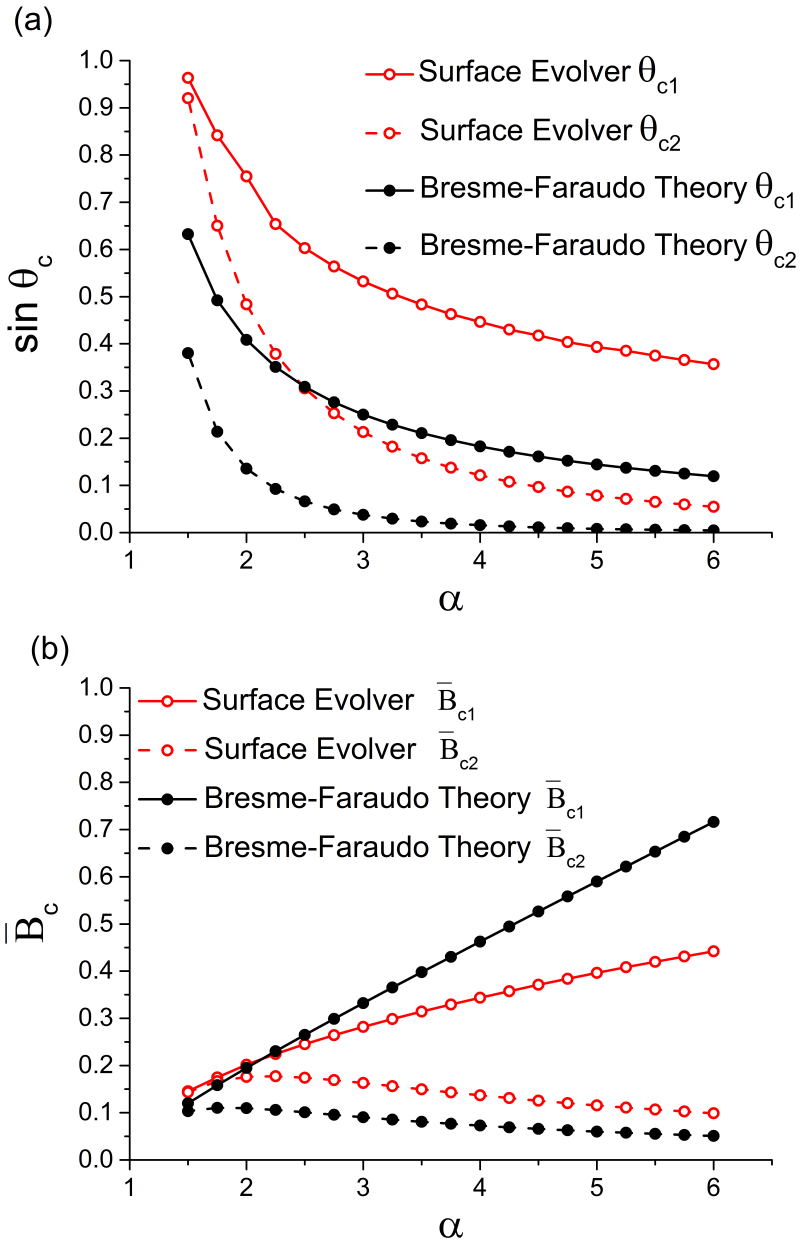

Figure 4.7: (a) Critical tilt angles θ_{c1}, θ_{c2} and (b) critical field strengths $\overline{B}_{c1}$, $\overline{B}_{c2}$ as a function of aspect ratio α for a particle with $\theta_w = 90°$ calculated using Surface Evolver and Bresme-Faraudo theory.

theory agrees qualitatively with Surface Evolver. Specifically, both theories predict that θ_{c1}, θ_{c2} decrease with increasing α and the width of the hysteresis curve $\overline{B}_{c1} - \overline{B}_{c2}$ increases with increasing α. Interestingly, for an aspect ratio of $\alpha = 1.5$, the width of the hysteresis curve falls to practically zero for both Surface Evolver and BF theory. However, as already noted in Figure 4.5, Surface Evolver predicts significantly lower critical tilt angles compared to BF theory for any given aspect ratio α (Figure 4.7(a)) and a significantly narrower width for the hysteresis curve compared to BF theory for any given α (Figure 4.7(b)).

In Figure 4.8, we use Surface Evolver to analyse the dependence of the critical fields and critical tilt angles on the contact angle of the particles θ_w. This represents an extension to BF theory[30, 57] and ref.[32] which were restricted to the neutral wetting condition $\theta_w = 90°$. Specifically, in Figure 4.8(a), we plot θ_{c1} and θ_{c2} as a function of θ_w while in Figure 4.8(b) we plot $\overline{B}_{c1}$ and $\overline{B}_{c2}$ as a function of θ_w for $\alpha = 3$. We see that for increasing contact angle away from 90°, both the critical tilt angle and the critical field strength decrease. This makes physical sense since for increasing contact angle, more of the particle enters the oil phase, thus reducing the area of the oil/water interface removed by the particle. This reduces the interfacial tension torque relative to the magnetic torque acting on the particle, resulting in a decrease for both the tilt angle and field strength needed for orientational transitions of the particle.

Finally, we consider the feasibility of observing the above orientational transitions experimentally. Firstly, for a typical micron-sized system possessing a

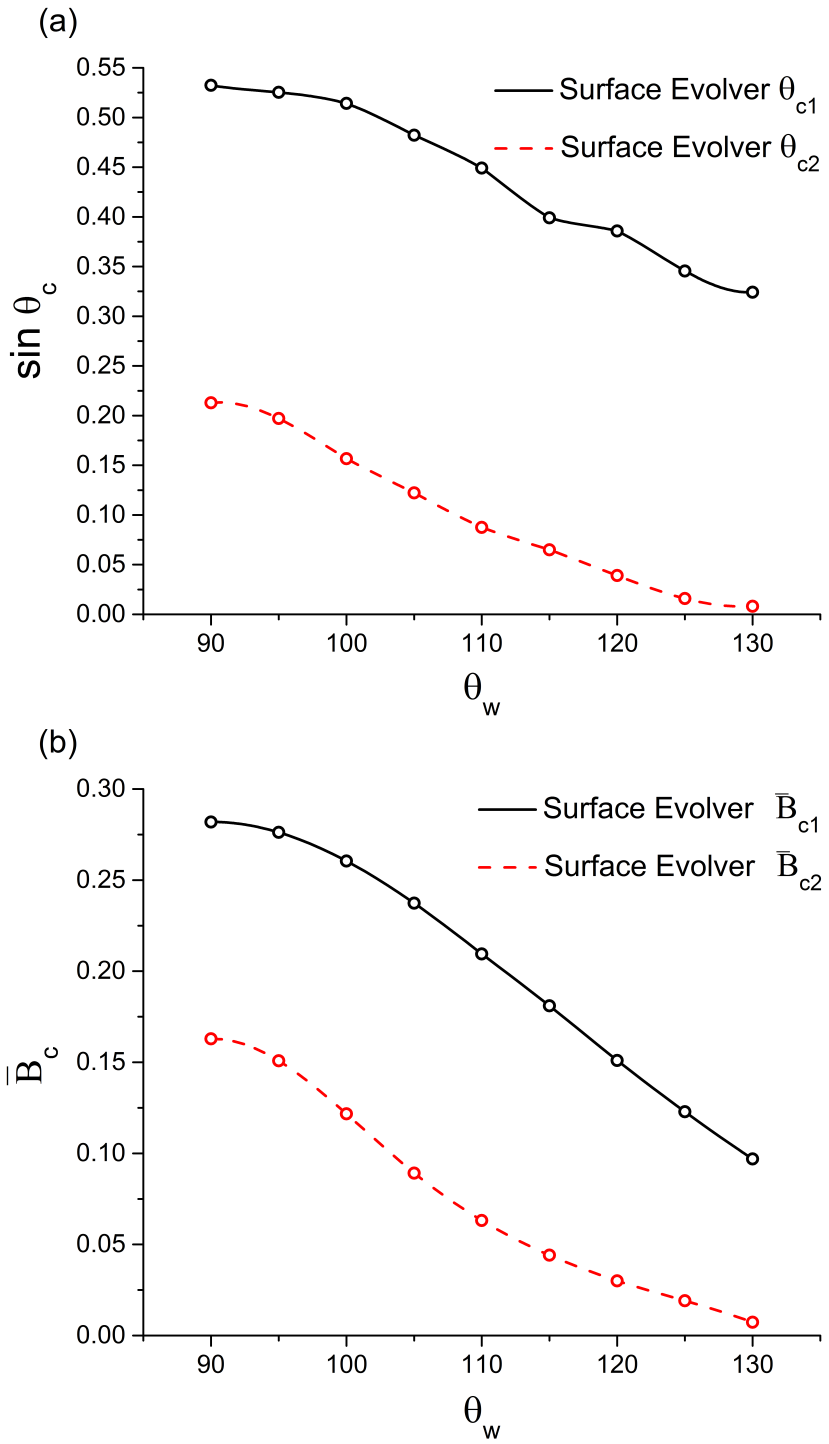

Figure 4.8: (a) Critical tilt angles θ_{c1}, θ_{c2} and (b) critical field strengths $\overline{B}_{c1}$, $\overline{B}_{c2}$ as a function of contact angle θ_w (in degrees) for a particle with aspect ratio $\alpha = 3$ calculated using Surface Evolver.

permanent magnetic dipole, we use parameters for anisotropic maghemite (γ-Fe_2O_3) particles[65] prepared by the group of Paul Clegg at the University of Edinburgh.[66] Assuming a typical rod length of $L = 3\mu m$ and aspect ratio of $\alpha = 10$, this yields a magnetic dipole moment $m = 4 \times 10^{-14}\text{A}\cdot\text{m}^{-2}$. Assuming a contact angle of $\theta_w = 90°$, for $\alpha = 10$ the dimensionless critical field for the tilt to perpendicular transition is $\overline{B}_{c1} \approx 0.5$ (by extrapolating Figure 4.7). Using a typical oil/water tension of $\gamma_{ow} = 30\text{mN}\cdot\text{m}^{-1}$, this translates to a real magnetic field of $B = 0.7\text{T}$, which is achievable experimentally.

Next, for a typical micron-sized parametric system, we use the parameters considered in ref.[30] with rod length $L = 3\mu m$, aspect ratio $\alpha = 1.7$, oil/water tension $\gamma_{ow} = 10\text{mN}\cdot\text{m}^{-1}$ and magnetic susceptibility $\chi = 10$. We further assume that the magnetic dipole is given by $m = \chi B/\mu_0 \cdot \pi d^2 L/4$, where B is the external magnetic field, μ_0 is the permeability of free space and d is the diameter of the rod. Assuming a contact angle of $\theta_w = 90°$, for $\alpha = 1.7$ we have $\bar{B}_{c1} \approx 0.1$, which translates to a real magnetic field of $B = 0.02\text{T}$. This is in excellent agreement with the estimate in ref.[30] and is easily achievable experimentally.

From Figures 4.7 and 4.8, we note that these critical fields can be readily tuned by a factor of up to 3 to 4 by changing particle aspect ratio or contact angle within a reasonable range. Interfacial magnetic ellipsoids are therefore a versatile system whose properties can be readily tailored for specific applications.

4.4. Conclusion

Using the finite element package Surface Evolver, we have studied the orientational transitions of an ellipsoidal magnetic particle adsorbed at a liquid interface due to an applied external field, explicitly accounting for the deformation of the liquid meniscus around a particle. We find that when the magnetic field is increased beyond a critical field $\overline{B}_{c1}$, the particles undergo a discontinuous transition to the perpendicular state (tilt angle $\theta_t = 90°$). Our results are in qualitative agreement with the simplified model of Bresme and Faraudo[30, 57] (which assumes a flat liquid interface) and in quantitative agreement with recent lattice-Boltzmann simulations[32] (which account for deformation of the liquid interface). Our calculations demonstrate that whilst assuming a flat interface allows us to capture the essential qualitative features of the orientational transition, it is important to explicitly include the deformation of the liquid interface for quantitative calculations of the transition. We also show that there is significant hysteresis in the orientational transition of micron-sized ellipsoidal particles due to the very large energy barriers that exist between the tilted and perpendicular states for this system. This hysteresis is in fact also predicted by the model of Bresme and Faraudo but has not been explicitly discussed previously. For currently available micron-sized anisotropic magnetic particles, we show that the critical magnetic fields required to induce the orientational phase transitions discussed above are achievable experimentally. Furthermore, we demonstrate that these critical fields can be readily tuned by a factor of 3 to 4 by changing the aspect ratio or contact angle of the magnetic particles. This interfacial system therefore represents

a versatile platform which can be used to design switchable materials with specific mechanical, optical or magnetic properties.

Chapter 5
Single Cylinder in an External Field

5.1. Introduction

As discussed in the previous Chapter, recent studies have shown that for magnetic ellipsoidal particles adsorbed at a liquid interface, when an external field is applied perpendicular to the liquid interface, it is possible to stabilise tilted configurations of the ellipsoidal particles, and above a critical field strength, the ellipsoidal particles undergo an irreversible orientational transition to the end-on state.[30, 32] For neutrally wetting ellipsoidal particles ($\theta_w = 90°$), where quadrupolar deformations of the meniscus are absent, Davies et al.[4, 58] have shown in their seminal work that the tilted orientation of the particles leads to dipolar capillary interactions between particles that can be used to create a switchable system where the self-assembled structure can be controlled using an external field.[4] However, one drawback of ellipsoidal particles is that because the side-on state is the only stable orientation in the absence of an external field, as soon as the external field is removed, the ellipsoidal particles revert to the side-on state and all memory of particle orientation and self-assembled structure is lost, i.e., the switching effect is *volatile*.

In order to overcome this problem, in this Chapter we study the orientation of magnetic *cylindrical* particles adsorbed at a liquid interface in an external field. The advantage of cylindrical particles is that, because of their flat ends, cylinders can possess multiple locally stable orientations in the absence of an external field, including side-on and end-on states, as shown by Lewandowski et al.[11] This means that for cylindrical particles, orientational transitions

induced by an external field will not necessarily disappear when the external field is removed, i.e., the switching effect can be *non-volatile*.

We will analyse this problem theoretically using both a simplified thermodynamic model which assumes the liquid meniscus around the particle is flat and a high resolution finite element method (Surface Evolver[60]) which accurately captures the meniscus deformation around the particle. In contrast to previous studies, which only considered end-on and side-on states,[11] we also consider all intermediate particle orientations and find that the behaviour for cylindrical particles is even richer than hitherto anticipated. For example, we find that even in the absence of an external field, cylindrical particles can possess not only stable side-on and end-on states, but also stable *tilted* states, depending on the aspect ratio $\alpha = L/2r$ of the particle (where L and r are the length and radius of the cylinder respectively). Our calculations show that tilted configurations with perceptible tilt angles occur for aspect ratios in the range $0.5 \lesssim \alpha \lesssim 2$; this would explain why these tilted states have not been observed previously in experimental studies, as only smaller and larger α were investigated in detail.[11] Such tilted states have been predicted for exotic anisotropic Janus particles,[16, 50, 51] but to our knowledge this is the first time that their existence has been demonstrated for cylinders with homogeneous surface chemistry. In addition, by tuning both the aspect ratio α and contact angle θ_w, we show that it is possible to engineer cylindrical particles to have two, three or even four locally stable orientations which can be accessed by varying the external field. Such a system allows us to create switchable functional colloidal monolayers where we can induce multiple *non-volatile* changes

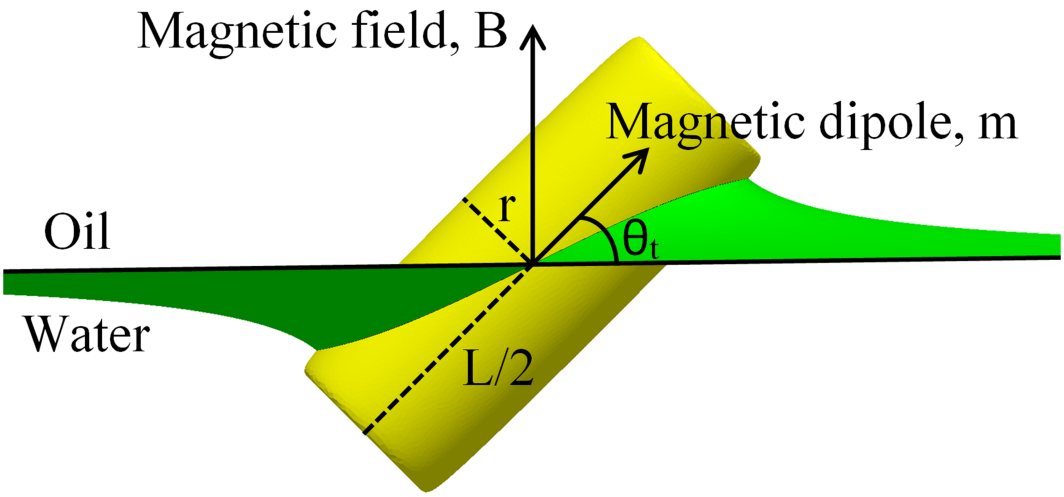

Figure 5.1: Configuration of a cylindrical particle adsorbed at an oil/water interface in the presence of an external field B applied perpendicular to the interface. The variables characterising the geometry of the tilted particle are discussed in the main text. The image is generated from Surface Evolver simulations of a cylinder with contact angle $\theta_w = 90°$, aspect ratio $\alpha = 2.5$, tilt angle $\theta_t = 45°$ and sharpness parameter $\eta = 20$ and the deformation of the liquid meniscus has been taken into account.

in optical, magnetic and mechanical properties using an external field.

5.2. Theoretical Model

In this section, we discuss the thermodynamics of the system and provide details of the flat interface model which we then compare with our Surface Evolver simulations which account for deformations of the interface.

We consider a cylindrical particle with length L and radius r adsorbed at an interface between two immiscible liquids (Figure 5.1). For convenience, we will refer to the top liquid as 'oil' and the bottom liquid as 'water' in what follows. The cylinder has an embedded magnetic dipole m along the long axis of the particle and the particle is tilted such that the magnetic dipole is at an angle θ_t with respect to the unperturbed interface. The aspect ratio of the cylindrical particle is defined as $\alpha = L/2r$, and the magnetic dipole interacts

with an external magnetic field B applied perpendicular to the interface.

The total free energy of the three phase system is given by

$$F_{int} = \gamma_{ow}A_{ow} + \gamma_{po}A_{po} + \gamma_{pw}A_{pw} - mB\sin\theta_t \tag{5.1}$$

where γ_{ow},γ_{po},γ_{pw} are the interfacial tensions and A_{ow},A_{po},A_{pw} are the areas of the oil/water, particle/oil and particle/water interfaces respectively. The free energy in Equation 5.1 can be simplified to the dimensionless form

$$\bar{F}_{int} \equiv \frac{F_{int}}{\gamma_{ow}A_p} = \overline{A}_{ow} + \cos\theta_w\overline{A}_{po} - \overline{B}\sin\theta_t \tag{5.2}$$

where $\overline{A}_{ow} = A_{ow}/A_p$, $\overline{A}_{po} = A_{po}/A_p$ are the dimensionless oil/water and particle/oil areas respectively, A_p is the surface area of the cylindrical particle, $\overline{B} = mB/\gamma_{ow}A_p$ is the dimensionless magnetic field strength and θ_w is the contact angle of the oil/water interface at the particle surface. Obviously, we can readily convert the dimensionless free energy to the free energy in units of k_BT by multiplying the dimensionless free energy with the factor $\gamma_{ow}A_p/k_BT$ for the relevant particle.

Minimizing $\overline{F}_{int}$ with respect to θ_t for a given value of $\overline{B}$ allows us to determine the equilibrium tilt angle of the particle for a given magnetic field strength. Note that minimizing $\overline{F}_{int}$ is equivalent to solving the equation

$$\frac{1}{\cos\theta_t}\frac{\partial\overline{F}_{st}}{\partial\theta_t} = \overline{B} \tag{5.3}$$

where

$$\overline{F}_{st} = \overline{A}_{ow} + \cos\theta_w \overline{A}_{po} \tag{5.4}$$

is the free energy contribution from the interfacial tension terms. Thus, by calculating the interfacial energy $\overline{F}_{st}$ and $\frac{\partial \overline{F}_{st}}{\partial \theta_t}$ as a function of θ_t, we can determine the equilibrium tilt angle for a given $\overline{B}$ via Equation 5.3. This is the method we use to calculate the magnetic response of the cylindrical systems in this paper, including equilibrium tilt angles, critical fields and critical tilt angles (see Appendix B).

The interfacial free energy $\overline{F}_{st}$ is calculated in two ways in this paper. In the first approach, following Bresme and Faraudo, we assume that the oil/water meniscus around the adsorbed cylinder is flat.[30] This simplifying assumption allows us to calculate $\overline{A}_{ow}$ analytically and we will use this method to study the case of neutrally wetting cylinders ($\theta_w = 90°$), where the $\overline{A}_{po}$ term in Equation 5.4 can be neglected. In the second approach, we calculate both $\overline{A}_{po}$ and $\overline{A}_{ow}$ numerically using the finite element method Surface Evolver.[60] This approach allows us to accurately model the deformation of the oil/water meniscus around the particle and we will use this method to analyse both neutrally wetting and non-neutrally wetting cylinders ($\theta_w \neq 90°$).

We calculate the interfacial free energy (Equation 5.4) for a cylinder of length L, radius r, assuming the liquid interface remains flat in the presence of the adsorbed cylinder. To simplify our calculation, we consider the neutrally wetting case $\theta_w = 90°$ where the cylinder centre is located at the interface plane and the particle rotates about its centre and we can neglect the $\overline{A}_{po}$ term in Equation 5.4. In the flat interface model, the area of the oil/water

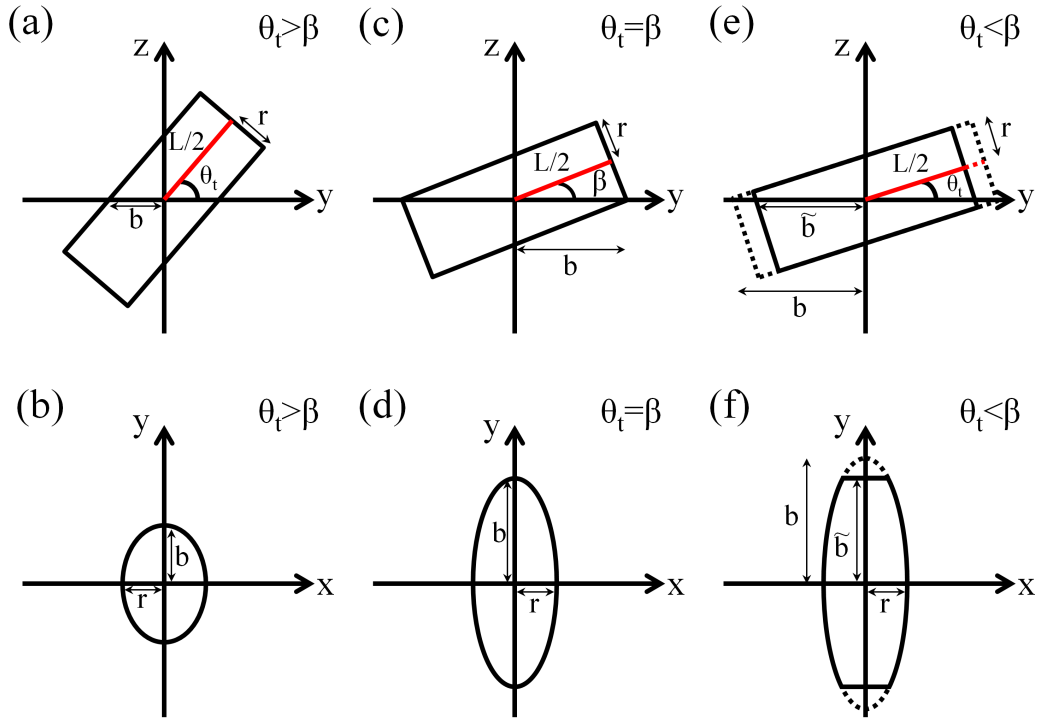

Figure 5.2: Configuration of a cylinder with $\theta_w = 90°$ at an oil/water interface for different tilt angles, assuming the oil/water interface remains flat. Here $\beta = \tan^{-1} 2r/L$ is the critical tilt angle where the liquid interface just intersects the flat ends of the cylinder. (a), (c), (e) represent the side view of the cylinder while (b), (d), (f) represent the intersection between the flat interface and the cylinder.

interface in the presence of the adsorbed particle is simply given by

$$A_{ow} = A_0 - A_{st} \tag{5.5}$$

where A_0 is an (uninteresting) constant representing the total area of the oil/water interface in the absence of the adsorbed particle and A_{st} is the intersection area between the cylinder and the flat interface. Our task is therefore to calculate A_{st} as a function of tilt angle θ_t. Without loss of generality, we assume that the particle centre is at the origin, the interfacial normal is in the z direction, the particle rotates about the x-axis and the long axis of the cylinder is in the y direction when it is in the side-on state (Figure 5.2).

We first define the critical tilt angle β as the angle where the liquid interface just intersects the flat ends of the cylinder (Figure 5.2(c) and (d)). From simple geometry, $\tan\beta = 2r/L$. For $\theta_t > \beta$, the liquid interface does not intersect the flat ends of the cylinder (Figure 5.2(a)) and the intersection between the interface and the cylinder is therefore an ellipse with semi-minor axis $a = r$ and semi-major axis $b = r/\sin\theta_t$ (Figure 5.2(b)). In this case, the intersection area is given by

$$A_{st} = \pi ab = \frac{\pi r^2}{\sin\theta_t}, \ (\theta_t > \beta) \tag{5.6}$$

For $\theta_t \leq \beta$, the liquid interface intersects the ends of the cylinder (Figure 5.2(e)) and the intersection between the interface and the cylinder is therefore an ellipse with semi-minor axis $a = r$ and semi-major axis $b = r/\sin\theta_t$ which is truncated at $y = \pm\tilde{b}$ (Figure 5.2(f)), where $\tilde{b} = L/(2\cos\theta_t)$. Noting that the equation for the ellipse is $(x/r)^2 + (y/b)^2 = 1$, the intersection area in this case is given by

$$\begin{aligned} A_{st} &= 4\int_0^{\tilde{b}} x(y)dy = 4a\int_0^{\tilde{b}} \sqrt{1-\tfrac{y^2}{b^2}}dy \\ &= \tfrac{Lr}{\cos\theta_t}\left[\sqrt{1-f(\theta_t)^2} + \tfrac{\sin^{-1} f(\theta_t)}{f(\theta_t)}\right], \ (\theta_t \leq \beta) \end{aligned} \tag{5.7}$$

where $f(\theta_t) = \alpha\tan\theta_t$.

We now provide details for the finite element package Surface Evolver[60] that we use to calculate the interfacial free energy and equilibrium meniscus shape around a cylindrical particle. One problem with using finite element methods to analyse the orientational behaviour of cylinders is that the method becomes numerically unstable when the three phase contact line crosses the

sharp edge of the cylinder. To overcome this problem, we approximate the cylinder using the super-ellipsoid equation[34]

$$\left(\frac{z^2}{r^2}+\frac{x^2}{r^2}\right)^{\eta}+\left(\frac{2y}{L}\right)^{2}=1 \tag{5.8}$$

where η is the sharpness parameter, with $\eta = 1$ and $\eta = \infty$ corresponding to an ellipsoid and a cylinder with infinitely sharp edges respectively. In our calculations, we use $\eta = 20$ which corresponds to a cylinder with slightly rounded edges (see Figure 5.1); we find that this value of η represents a good compromise between numerical accuracy and stability (see Appendix C). From an experimental point of view, studying cylinders with slightly rounded edges is also interesting in its own right since cylinders with infinitely sharp edges are an idealised limiting case and real cylinders will inevitably have slightly rounded edges.

In our simulations, the cylinder is gradually tilted from 0° to 90° in 1° increments; only tilt angles $0° \leq \theta_t \leq 90°$ need to be explicitly calculated since, in the absence of an external field, the orientational free energy is symmetrical about $\theta_t = 0°$. The oil-water and particle-oil interfaces are divided into a mesh of small triangles which are displaced to minimise the interfacial energy subject to appropriate constraints. Specifically, we apply the super-ellipsoid equation (Equation 5.8) on the vertices representing the particle and the contact line where the particle meets the oil-water interface. For computational convenience and without loss of generality, the centre of the particle is fixed at the origin of the coordinate system used and the interface is free to move vertically to satisfy the contact angle. Also, the homogeneous Neumann boundary

condition is used at the outer boundary of the simulation domain to ensure a flat interface far from the particle.[12] We calculate the area of the interface by adding up the individual facets of the triangulated mesh. We compared results for $\eta = 1$ (i.e., ellipsoidal particle) with results from the previous Chapter to confirm that the method gave the same results. In order to achieve good numerical accuracy we used a mesh that has a higher level of refinement close to the particle. In the last stages of the evolution we change the model type from linear to quadratic which adds vertices at the midpoints of each edge followed by further minimisation which allows us to evaluate the areas with high accuracy. For example, for particles with an aspect ratio $\alpha = 2.5$, contact angle $\theta_w = 90^\circ$ and tilt angle $\theta_t = 45^\circ$, we used 140000 triangles to represent the surface and 848 vertices to represent the contact line; the specific number of triangles and vertices used was varied depending on the values of α, θ_w and θ_t. We use a square simulation box which has length $12 \times L$ for $\alpha > 1$, or length $12 \times r$ for $\alpha < 1$, and we work in units of length where $r = 1$. In order to confirm that finite size constraints are negligible, for selected simulations, the simulation cell size was increased by 50% and yielded essentially the same results for the critical tilt angles (within 0.5%) and critical field strengths (within 0.3%).

5.3. Results & Discussion

In this section we present results for the orientational behaviour of magnetic cylinders at liquid interfaces and discuss their relevance for creating switchable functional surfaces and the feasibility of realising these results experimentally.

We first study the equilibrium orientation of neutrally wetting cylinders ($\theta_w = 90°$) adsorbed at the interface in the absence of an external field. In contrast to previous studies, which only considered the side-on and end-on states,[11] we also consider all intermediate particle orientations. In Figure 5.3(a)-(c), we plot the dimensionless free energy vs. tilt angle θ_t for $\theta_w = 90°$ for three different aspect ratios $\alpha = 2.5$, 1.0, 0.25 respectively. The dashed lines are the predictions of the flat interface model while the solid lines are the predictions of Surface Evolver, which takes into account the deformation of the meniscus. Figure 5.3(d)-(h) are the equilibrium orientations for the different values of α predicted by Surface Evolver. Focussing first of all on the predictions of the flat interface theory, we see that for large α (e.g., $\alpha = 2.5$, Figure 5.3(a)), the side-on state ($\theta_t = 0°$) is the equilibrium state, i.e., the global minima of the free energy. In addition, as we decrease α, the side-on state becomes less stable relative to the end-on state ($\theta_t = 90°$) such that for small α (e.g., $\alpha = 0.25$, Figure 5.3(c)) the end-on state is more stable than the side-on state. These results are in good agreement with previous studies.[11]

However, our fuller analysis reveals the surprising result that for small aspect ratios α (below a critical value $\alpha_c \approx 2$), the equilibrium state is not the end-on state anticipated in previous studies,[11] but a tilted configuration (Figure 5.3(b),(c)). Furthermore, the equilibrium tilt angle increases with decreasing α such that for very small α the equilibrium tilt angle is very close to $\theta_t = 90°$. All the qualitative features predicted by the flat interface theory are corroborated by the Surface Evolver results (Figure 5.3(a)-(c) solid lines), with the quantitative differences between the two theories being due to the fact that

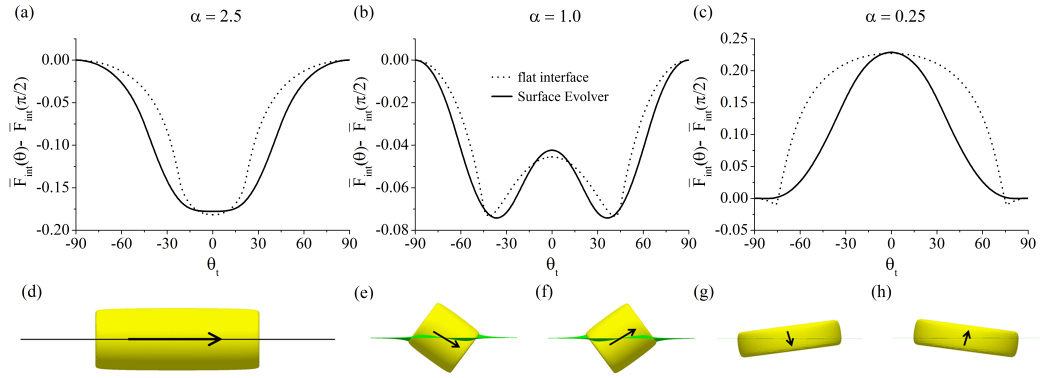

Figure 5.3: (a)-(c) Dimensionless free energy (relative to the end-on configuration) as a function of tilt angle for cylindrical particles in the absence of an external field with contact angle $\theta_w = 90°$ and different aspect ratios α calculated from flat interface theory (dashed line) and Surface Evolver simulations with $\eta = 20$ (solid line); (d)-(h) Equilibrium configurations of the particle for the different values of α obtained from Surface Evolver simulations. The specific tilt angles are (d) 0°; (e) −36.4°; (f) +36.4°; (g) −82.6°; (h) +82.6°.

Surface Evolver explicitly accounts for interfacial deformation and uses slightly rounded edges. Note that both flat interface theory and the Surface Evolver calculations predict that tilted configurations with perceptible tilt angles only occur for aspect ratios in the range $0.5 \lesssim \alpha \lesssim 2$; this would explain why these tilted states have not been observed previously in experimental studies of neutrally wetting cylinders,[11] as only smaller and larger α were investigated in detail in these studies.

We note the striking resemblance between the free energy curves in Figure 5.3 and those for spontaneous symmetry breaking in ferromagnets under zero field conditions.[67] Making this analogy between the two systems, the side-on state (Figure 5.3(a)) corresponds to the paramagnetic state, the tilted state (Figure 5.3(b),(c)) corresponds to the ferromagnetic state and the aspect ratio α plays the role of temperature. We emphasise that this analogy is purely mathematical, since we are performing single particle simulations throughout this paper, while in real ferromagnets, the spontaneous magnetisation is

due to many-body interactions between neighbouring magnetic dipoles. Notwithstanding this important *physical* difference between the two systems, our mathematical analogy is nevertheless useful in helping us anticipate the magnetic response of single cylinders at liquid interfaces. Specifically, it suggests that the response of cylinders with $\alpha > \alpha_c$ and $\alpha < \alpha_c$ to an external magnetic field should be similar to that of paramagnets and ferromagnets respectively, an expectation which is confirmed later on (see Figure 5.5).

By performing a series expansion (i.e., Landau expansion) of $\overline{F}_{st}$ in θ_t about $\theta_t = 0^\circ$ for the flat interface theory (i.e., using Equations (5.5) and (5.7) in Equation (5.4)) to quadratic order, we find

$$\overline{F}_{st} = \text{const} + \frac{\alpha^2}{3\pi\,(1+2\alpha)}(\alpha^2 - 3)\theta_t^2. \tag{5.9}$$

Noting that the critical aspect ratio is the aspect ratio where the quadratic coefficient in the Landau expansion vanishes, Equation (5.9) predicts that $\alpha_c = \sqrt{3}$. This value for α_c from the flat interface theory is slightly lower that the value deduced from our Surface Evolver calculations for neutrally wetting cylinders, i.e., $\alpha_c \approx 2.3$ (see Figure 5.12 and Table 5.1).

An interesting question concerns the symmetry of meniscus deformations around particles in the equilibrium tilted state for $\alpha < \alpha_c$. Naively, one might expect the leading order deformation to be dipolar. However, dipolar deformations are forbidden as there is no external torque acting on the particle at equilibrium.[23, 41] In Figure 5.4(a) and (b), we plot the Surface Evolver results for the deformation field and contact line respectively around a cylindrical particle in the equilibrium tilted state with $\theta_w = 90^\circ$ and $\alpha = 1$.

We see that the deformation is in fact neither dipolar nor quadrupolar but *hexapolar*. Under zero bond number conditions (i.e., where gravity is negligible), the leading order distortion that is allowed is quadrupolar,[23, 41] and indeed for simple anisotropic shapes like ellipsoids, the leading order distortion is always quadrupolar.[7–9] However, for more complex particles shapes, it is possible to have leading order deformations which are of a higher order multipole. For example, the leading order distortion for cuboidal particles has recently been shown to be octupolar.[33] The theoretical framework for the interaction between capillary multipoles of arbitrary order has been worked out by Danov et al.[68]

Next, we consider the response of neutrally wetting cylindrical particles to an external field applied perpendicular to the liquid interface. In Figure 5.5(a), we plot the Surface Evolver results for the free energy as a function of tilt angle for cylinders with $\alpha = 2.5 > \alpha_c$. At zero field, the equilibrium state is the side-on state (black curve), but as we increase the field strength, the equilibrium state shifts to a tilted state with finite tilt angle (e.g., blue curve), with the equilibrium tilt angle increasing with increasing field strength. As the field strength is further increased above a critical field $\overline{B}_{c1}$, the free energy curve develops a second minima at $\theta_t = 90°$ corresponding to the end-on state, and at a field strength of $\overline{B} = \overline{B}_0 = 0.288$, the free energy of the tilted state becomes equal to that of the end-on state (green curve, see inset). At this point, the particle in principle undergoes a first order phase transition from the tilted state to the end-on state. The filled circles on the green curve with tilt angles $\theta_0 = 33.8°$ and $90°$ are therefore binodal points of the system. However,

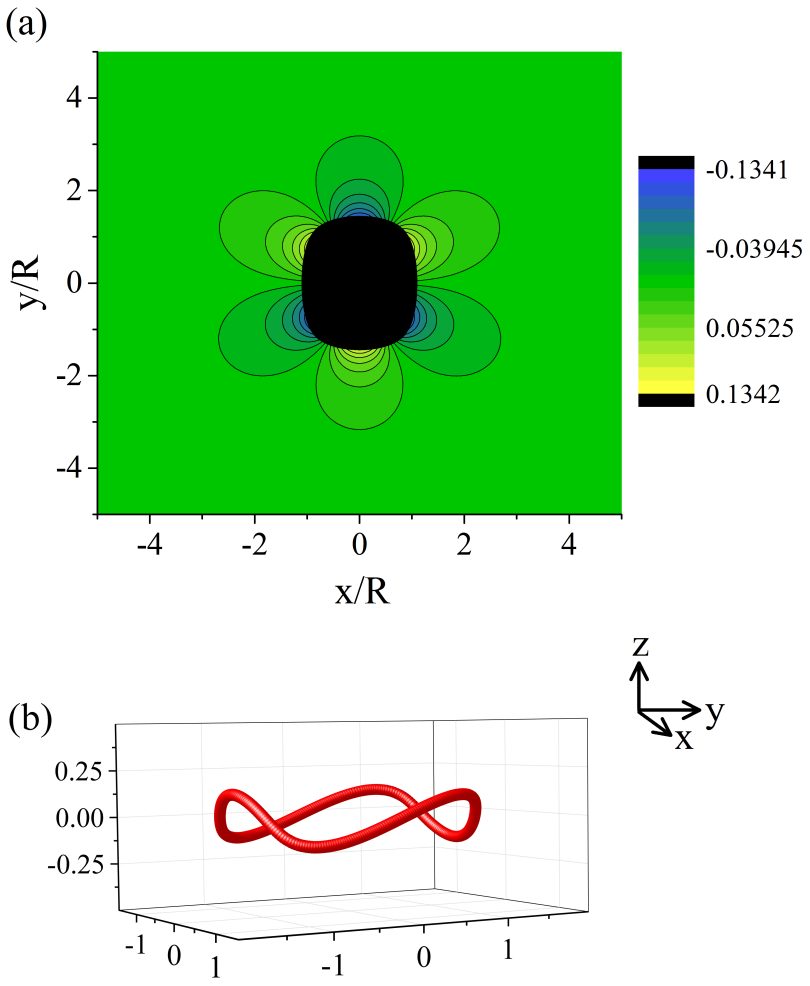

Figure 5.4: Surface Evolver results for (a) the meniscus deformation (contour plot) and (b) contact line around a cylindrical particle in the equilibrium tilted configuration with $\theta_w = 90°$, $\alpha = 1$, $\eta = 20$ ($\theta_t = 36.4°$). Note the clear hexapolar symmetry of the deformation.

for micron-sized particles (which is the focus of this Chapter), the very large energy barrier between the two local minima means that in practice there is significant hysteresis in the orientational transition. Specifically, for increasing magnetic fields, the particle only undergoes an irreversible transition from the tilted state to the end-on state when $\overline{B} = \overline{B}_{c2}$, where the local minima for the tilted state disappears (red curve, see inset), while for decreasing field strengths, the particle only undergoes an irreversible transition from the end-on state to the tilted state when $\overline{B} = \overline{B}_{c1}$, where the local minima for the end-on state disappears (blue curve). The open circle on the red curve with tilt angle $\theta_{c2} = 43.1^\circ$ and the end on state ($\theta_t = 90^\circ$) on the blue curve are therefore spinodal points of the system. Analogous behaviour to everything discussed above also occurs for $\overline{B} < 0$.

The magnetic response of the long cylinder ($\alpha > \alpha_c$) is summarised in Figure 5.5(b) where we plot the Surface Evolver results for the locally stable tilt angle ($\sin\theta_t$) as a function of the external field ($\overline{B}$) (see Appendix B for details of how the magnetic response was calculated). We note that, as anticipated earlier for $\alpha > \alpha_c$, the response of the cylinder is paramagnetic-like at low fields ($|\overline{B}| < \overline{B}_{c1}$), with the equilibrium tilt angle θ_t (or $\sin\theta_t$) playing the role of magnetisation in magnetic systems.[69] Specifically, as we increase the magnetic field from negative to positive values, the tilt angle increases *continuously* from negative to positive. On the other hand, the response of the system exhibits significant hysteresis at higher fields ($|\overline{B}_{c1}| \leq |\overline{B}| \leq |\overline{B}_{c2}|$), as discussed earlier.

From the point of view of creating switchable materials, the key feature of

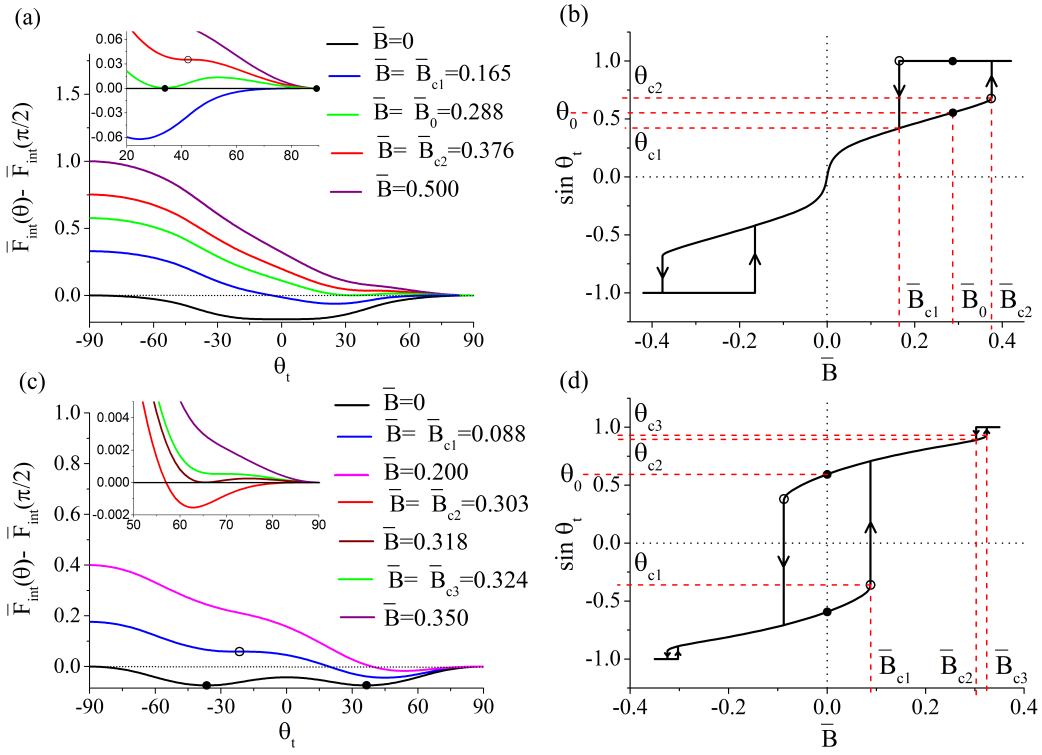

Figure 5.5: Surface Evolver results for the magnetic response of cylinders with $\theta_w = 90°$, $\eta = 20$. (a and c) Dimensionless free energy as a function of tilt angle for different field strengths for: (a) $\alpha = 2.5$; (c) $\alpha = 1.0$. The insets in (a) and (c) zoom in on the large tilt angle region of the free energy curves where there is a first order orientational transition between the tilted and end-on states at large fields. (b and d) Locally stable tilt angle as a function of field strength for: (b) $\alpha = 2.5$; (d) $\alpha = 1.0$. In (b and d), the vertical lines represent irreversible orientational transitions, with the direction of the transition as indicated by the arrows. For all the other solid lines in (b) and (d), it is possible to change the tilt angle along the line in either direction by changing the external field. In (a - d), the filled and open circles represent binodal and spinodal points of the orientational transitions respectively. Note that in (a), there is a spinodal point at the end-on state ($\theta_t = 90°$) on the blue curve. See main text for details.

Figure 5.5(b) is the fact that any particle orientations induced by an external field will disappear when the external field is removed ($\theta_t = 0$ for $\overline{B} = 0$), i.e., the switching effect is *volatile*. The magnetic response of neutrally wetting long cylinders is thus qualitatively the same as that of ellipsoidal particles as we have seen in the previous Chapter.[30, 32]

In Figure 5.5(c), we plot the Surface Evolver results for the free energy as a function of tilt angle for cylinders with $\alpha = 1.0 < \alpha_c$. As discussed earlier, at zero field the cylinder can adopt either one of two equivalent tilted states (filled circles on black curve). For definiteness, let us assume that the particle is initially in the tilted state with negative tilt angle. As we increase the field strength, the degeneracy between the two tilted states is broken and the negative tilted state is no longer the global minimum. Therefore, in principle, the particle should undergo a first order phase transition to the positive tilted state. The filled circles in the zero-field free energy curve, which have tilt angles of $\pm\theta_0$, are therefore *binodal* points of the system. However, the very large energy barrier between the local minima for micron-sized particles means that in practice the orientational transition does not occur until the field strength is equal to $\overline{B}_{c1}$ where the local minima for the negative tilted state merges with the energy barrier and the local minima disappear (open circle on blue curve). The open circle on the blue curve, which has a tilt angle of $-\theta_{c1}$, are therefore *spinodal* points of the system for positive external field. Similarly, if the particle is in the positive tilted state, upon decreasing the external field, the orientational transition to the negative tilted state does not occur until the field strength is equal to $-\overline{B}_{c1}$. To complete the picture, as we increase

the field strength above $\overline{B}_{c3}$ (or decrease the field strength below $-\overline{B}_{c3}$), there is a further (small) first order orientational transition in the large field regime (see inset to Figure 5.5(c)) which leads to a small degree of hysteresis in the magnetic response between $\overline{B}_{c2} \leq |\overline{B}| \leq \overline{B}_{c3}$ (Figure 5.5(d)).

The magnetic response of the short cylinder ($\alpha < \alpha_c$) is summarised in Figure 5.5(d) where we plot the Surface Evolver results for the locally stable tilt angle ($\sin\theta_t$) as a function of the external field ($\overline{B}$). The most striking feature of Figure 5.5(d) is the fact that the response of short cylinders at low fields ($|\overline{B}| < \overline{B}_{c3}$) is ferromagnetic-like rather than paramagnetic-like. Specifically, assuming the cylinder is initially in the negative tilted state, as we increase the magnetic field from negative to positive, thermodynamically the tilt angle undergoes a reversible, discontinuous transition from $-\theta_0$ to $+\theta_0$ at $\overline{B} = 0$ (i.e., bottom filled circle to top filled circle in Figure 5.5(d)). However, as discussed earlier, in practice the tilt angle undergoes an irreversible transition to the positive tilted state only when the magnetic field exceeds $\overline{B}_{c1}$ (i.e., bottom open circle in Figure 5.5(d)). Analogous behaviour is also observed when we decrease the magnetic field starting from the positive tilted state.

Applying the terminology for ferromagnetic systems to Figure 5.5(d), the tilt angles at the binodal points, i.e., θ_0 (filled circles in Figure 5.5(d)), correspond to the 'remanence' of the cylinder while the magnetic field at the spinodal points, i.e., $\overline{B}_{c1}$ (open circles in Figure 5.5(d)), corresponds to the 'coercivity' of the system.[69] From the point of view of creating switchable materials, the key feature of Figure 5.5(d) is the fact that the system possesses two locally stable orientations (corresponding to the filled circles) which do not disappear

when the the external field is removed and which can be accessed by varying the external field, i.e., the switching effect is *non-volatile*. This means that neutrally wetting short cylinders ($\alpha < \alpha_c$) can be used to create switchable functional surfaces with non-volatile switching.

In Figure 5.6, we study the magnetic response of neutrally wetting cylinders to low external fields over a more comprehensive range of α values, both above and below α_c. Specifically, we plot the Surface Evolver results for the stationary tilt angles (i.e., tilt angles corresponding to minima or maxima of the free energy curves) as a function of the external field $\overline{B}$ for different values of α, with the solid (dashed) lines corresponding to locally stable (unstable) tilt angles. The filled and unfilled circles in Figure 5.6 correspond to the binodal and spinodal points respectively when $\alpha < \alpha_c$. Note that the solid curves between the binodal and spinodal points are metastable while the rest of the solid curves are stable. Details of how the magnetic response for different α was calculated, including the tilt angles and magnetic fields at the binodal and spinodal points, are provided in Appendix B.

The magnetic response curves in Figure 5.6 clearly resemble the magnetisation curves for a ferromagnet as it goes through the Curie temperature. Specifically, for $\alpha > \alpha_c$, the magnetic response is paramagnetic-like (c.f. Figure 5.5(b)) while for $\alpha < \alpha_c$, the response becomes ferromagnetic-like (c.f. Figure 5.5(d)). Note that in Figure 5.6 we have explicitly plotted the unstable part of the magnetic response curves (dashed lines). In reality, micron-sized magnetic cylinders will undergo an irreversible orientational transition when the magnetic field is reduced below the left most spinodal point or increased

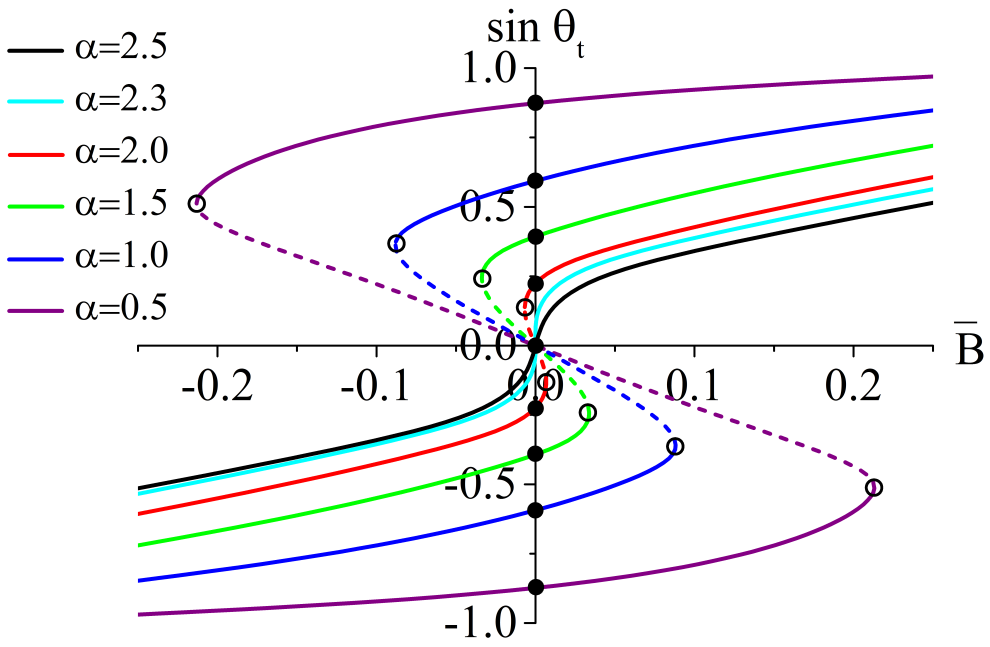

Figure 5.6: Surface Evolver results for the stationary tilt angles (i.e., tilt angles corresponding to minima or maxima of the free energy curves) as a function of the external field $\overline{B}$ in the low field regime for different values of α for neutrally wetting cylinders with $\eta = 20$. The solid (dashed) lines correspond to locally stable (unstable) tilt angles. The filled and unfilled circles correspond to the binodal and spinodal points respectively when $\alpha < \alpha_c$. Note that the solid curves between the binodal and spinodal points are metastable while the rest of the solid curves are stable. See main text for details.

above the right most spinodal point (see Figure 5.5(d)).

In Figure 5.7 we plot the phase diagram for orientational transitions of neutrally wetting magnetic cylinders in the $\overline{B} - \alpha$ plane, including the binodal line (solid line), the spinodal line (dashed line) and the critical point $(\alpha_c, 0)$. Referring to the phase diagram, for $\overline{B} > 0$ and $\overline{B} < 0$, the thermodynamically stable tilt angle is positive and negative respectively. For magnetic cylinders with $\alpha > \alpha_c$, as we increase the magnetic field from negative to positive, the tilt angle changes continuously from negative to positive. In contrast, for magnetic cylinders with $\alpha < \alpha_c$, as we increase the magnetic field from negative to positive, *thermodynamically*, the tilt angle changes discontinuously from negative to positive at the binodal line. However, for micron-sized magnetic cylinders, *kinetically*, the tilt angle will change discontinuously from negative to positive only at the upper spinodal line. For all values of α, analogous behaviour also occurs as we decrease the magnetic field from positive to negative. Finally, we can find the locally stable tilt angle in all the cases discussed above by using the magnetic response curve for the relevant α value given in Figure 5.6.

In order to analyse the response of the meniscus deformation to particle tilt, in Figure 5.8 we plot Surface Evolver results for the difference in the maximal and minimal height along the contact line at the particle (normalised with respect to r), i.e., $\Delta z/r$, as a function of tilt angle for cylinders with $\theta_w = 90^\circ$ and different values of α. Only positive values of θ_t are considered in Figure 5.8 since the plots are symmetrical about $\theta_t = 0^\circ$. We note that $\Delta z/r$ can be measured experimentally using phase shift interferometry (PSI).[33, 59] Referring to Figure 5.5(b) and (d), only some tilt angles θ_t are accessible

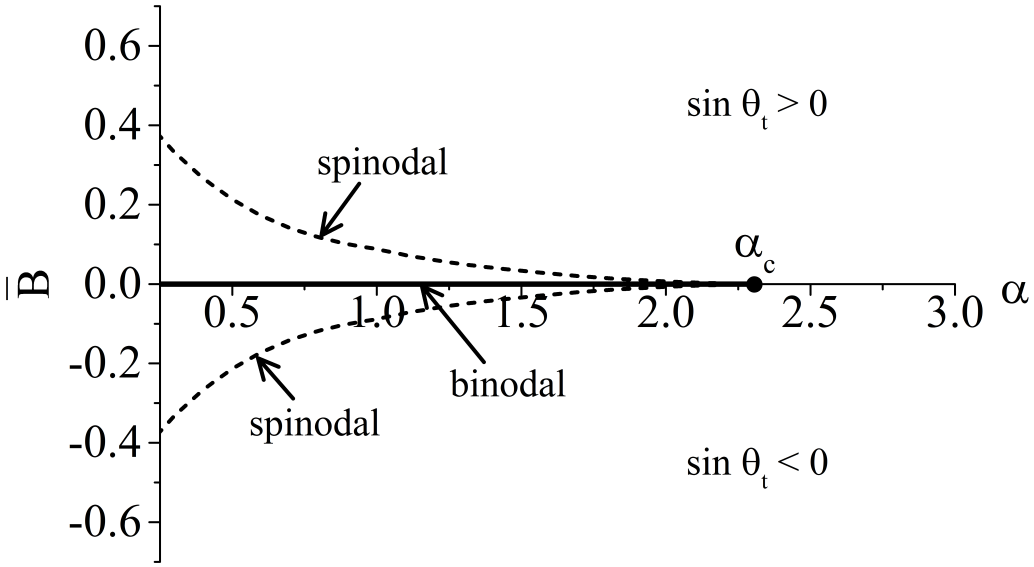

Figure 5.7: Phase diagram for orientational transitions of neutrally wetting magnetic cylinders in the $\overline{B} - \alpha$ plane calculated from Surface Evolver, including the binodal line (solid line), the spinodal line (dashed line) and the critical point. The thermodynamically stable tilt angle above (below) the $\overline{B} = 0$ line is positive (negative).

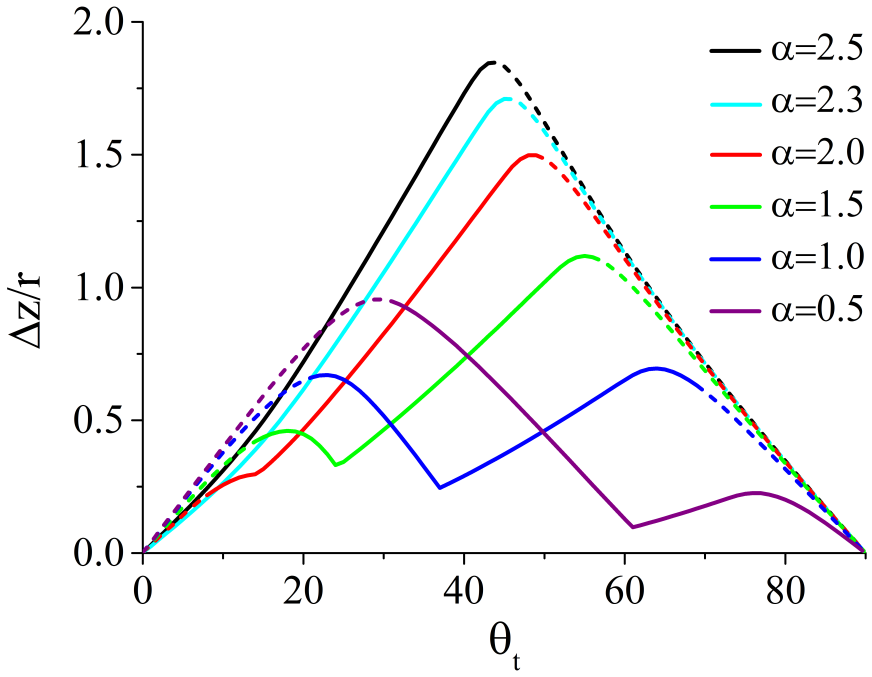

Figure 5.8: The difference in the maximal and minimal height along the contact line (normalised with respect to r) $\Delta z/r$ as a function of tilt angle for neutrally wetting cylinders for different values of α. Tilt angles which are accessible (inaccessible) through varying the external field are plotted as solid (dashed) lines. See main text for details.

through varying the external field, specifically $|\theta_t| \leq |\theta_{c2}|$ for $\alpha > \alpha_c$ and $|\theta_{c1}| \leq |\theta_t| \leq |\theta_{c3}|$ for $\alpha < \alpha_c$ and the accessible (inaccessible) tilt angles are plotted as solid (dashed) lines in Figure 5.8. We see that for $\alpha > \alpha_c$, the $\Delta z/r$ curves do not exhibit any minima (except for the trivial one at $\theta_t = 0°$), while for $\alpha < \alpha_c$, the curves exhibit a minima at the equilibrium tilt angle for that α. The minima in $\Delta z/r$ thus serve as a signature for equilibrium tilted states which can be readily verified experimentally.

To further analyse the response of the meniscus deformation on particle tilt, in Figure 5.9 we plot Surface Evolver results for the area enclosed by the undulating contact line projected onto the unperturbed interfacial plane S as a function of tilt angle for cylinders with $\theta_w = 90°$ and for the same range of

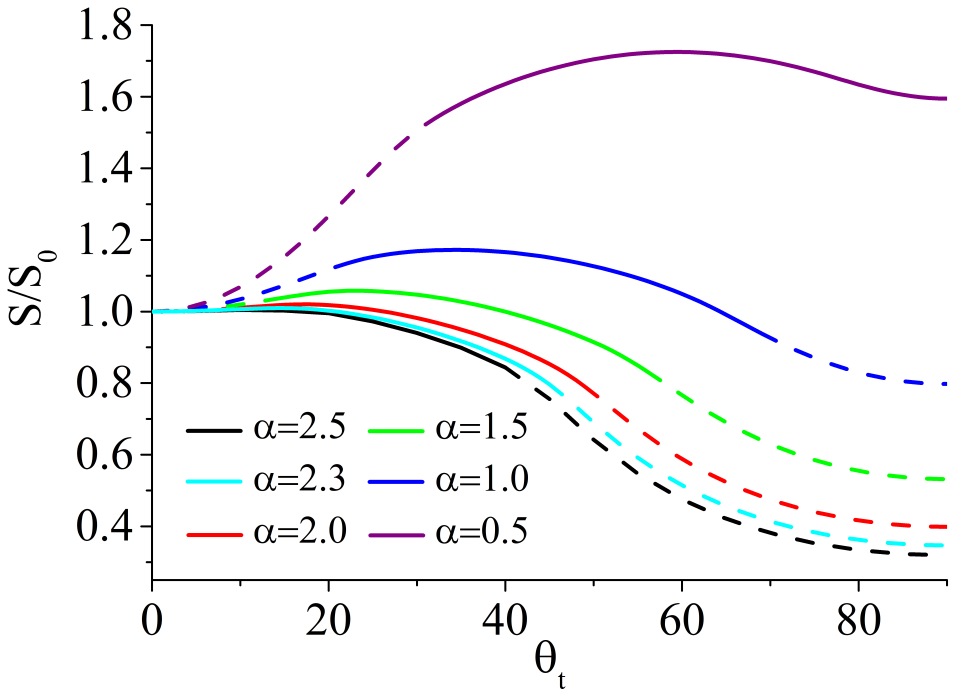

Figure 5.9: Surface Evolver results for the (normalised) projected area enclosed by the undulating contact line as a function of tilt angle for neutrally wetting cylinders with the same range of α as shown in Figure 5.8. Tilt angles which are accessible (inaccessible) through varying the external field are plotted as solid (dashed) lines. See main text for details.

α as shown in Figure 5.8. The projected area S for each α is normalised with respect to the projected area at zero tilt angle S_0. Once again, only positive values of θ_t are considered in Figure 5.9 since the plots are symmetrical about $\theta_t = 0°$ and accessible (inaccessible) tilt angles are plotted as solid (dashed) lines. Note that the quantity S/S_0 can also be measured experimentally using PSI under reflection illumination.[33, 59] We see that for $\alpha > \alpha_c$, the S/S_0 curves do not exhibit any maxima (except for the trivial one at $\theta_t = 0°$), while for $\alpha < \alpha_c$, each curve exhibits a broad maxima at the equilibrium tilt angle for that α. The maxima in S/S_0 thus serve as an additional signature for tilted states which can be readily verified experimentally.

We next study the orientation and magnetic response of non-neutrally wet-

ting particles ($\theta_w \neq 90°$). Lewandowski et al.[11] showed that for a given aspect ratio α, changing the contact angle θ_w away from 90° stabilises the end-on state relative to the side-on state. This is because when $\theta_w \neq 90°$, the contact line in the end-on state is positioned at the corner of the cylinder so that, as we change θ_w away from 90°, the area of liquid interface removed by the cylinder is essentially unchanged for the end-on state, but it is decreased for the side-on state. This means that we can use θ_w, in addition to α, to engineer the orientational free energy landscape, and hence the magnetic response, of cylindrical particles.

In Figure 5.11 we plot Surface Evolver results for the dimensionless free energy as a function of tilt angle for contact angles $\theta_w = 100°$, 110° and aspect ratios $\alpha = 2.5$, 1.0, 0.5 in the absence of an external field. In Figure 5.10, we plot the Surface Evolver results for the dimensionless free energy as a function of tilt angle for cylinders with $\eta = 20$ in the absence of an external field for $\theta_w = 90° \rightarrow 110°$ and aspect ratios $\alpha = 0.5 \rightarrow 2.5$ in order to obtain a systematic picture of how changing θ_w and α impacts the orientational free energy landscape.

The free energy curves are plotted over the same range of α and θ_w but for more intermediate values in order to obtain a higher resolution picture of how changing θ_w and α impacts the orientational free energy landscape. From these results, we see that for a given $\theta_w \neq 90°$, as we reduce α below a critical value α_c, the free energy curve at small tilt angles undergoes spontaneous symmetry breaking into two equivalent tilted states as before. However, these results also suggest that increasing the contact angle away from $\theta_w = 90°$ leads to a

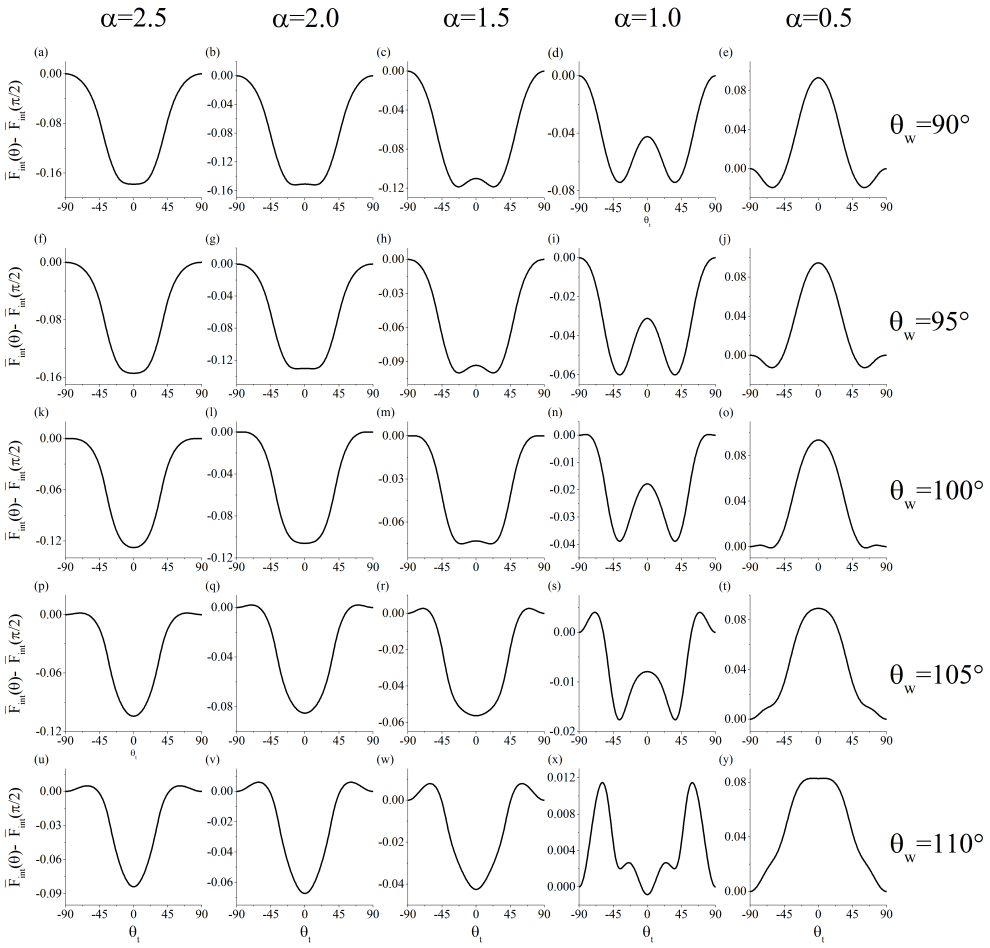

Figure 5.10: Surface Evolver results for the dimensionless free energy (relative to the end-on state) as a function of tilt angle for cylinders with $\eta = 20$ in the absence of an external field and different aspect ratios α and contact angles θ_w.

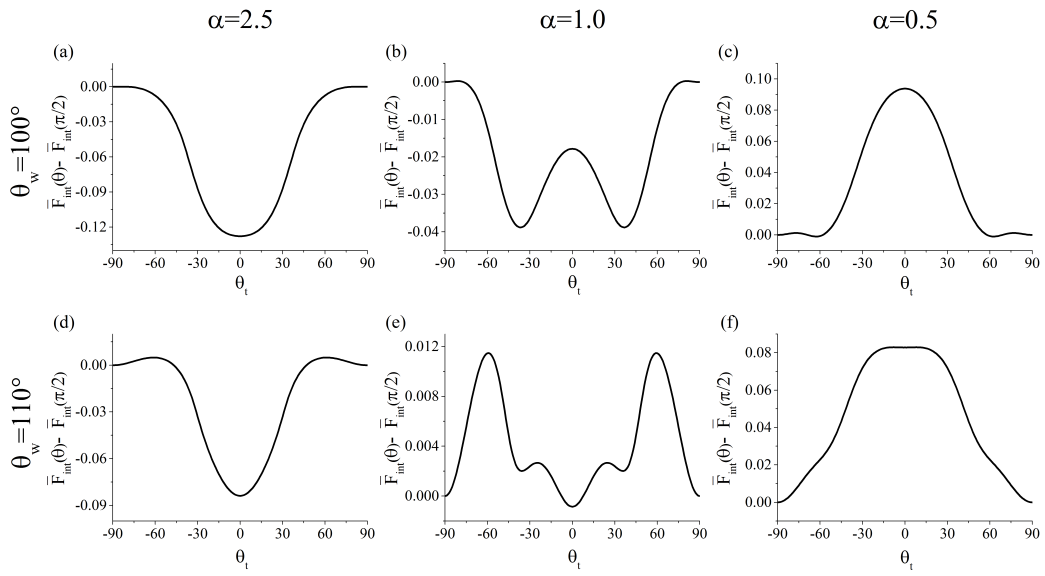

Figure 5.11: Surface Evolver results for the dimensionless free energy (relative to the end-on state) as a function of tilt angle for cylinders in the absence of an external field with $\eta = 20$ and different aspect ratios α and contact angles θ_w.

decrease in α_c.

In order to determine the value of α_c at each contact angle θ_w, we performed Surface Evolver simulations at small θ_t with a resolution of 0.1 in α. The critical aspect ratio was then determined from the value of α where the curvature at $\theta_t = 0$ changed sign. The results for α_c as a function of θ_w are tabulated in Table 5.1.

$\theta_w(^\circ)$	α_c
90	2.3
95	2.2
100	1.8
105	1.2

Table 5.1: Surface Evolver results for the critical aspect ratio α_c as a function of contact angle θ_w for cylinders

Note that we only need to perform simulations for $\theta_w > 90^\circ$ since the α_c values are symmetrical about $\theta_w = 90^\circ$. These results confirm that α_c indeed decreases as we change the contact angle away from $\theta_w = 90^\circ$. Note that for

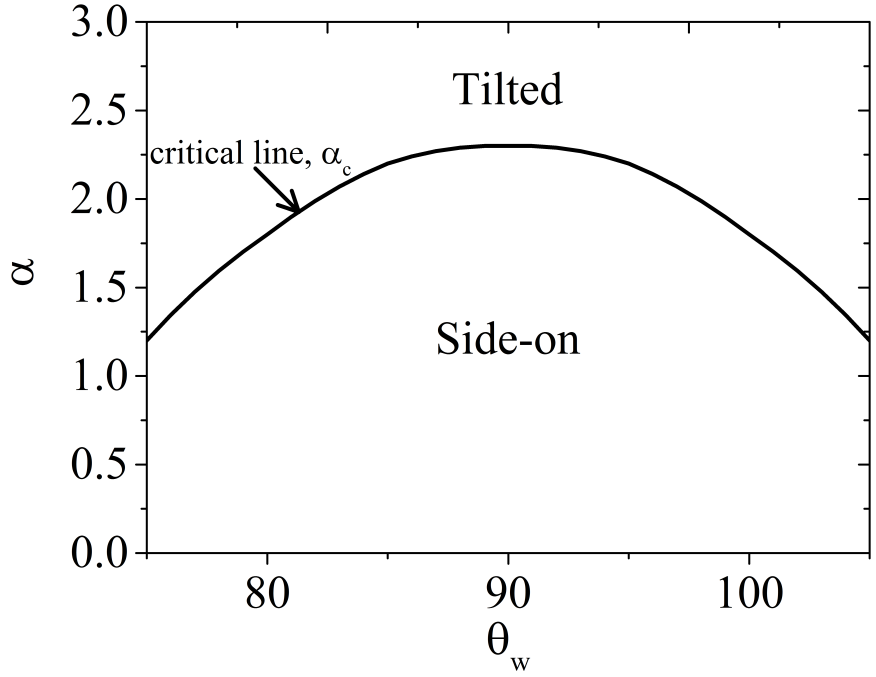

Figure 5.12: Phase diagram for magnetic cylinders in the $\alpha - \theta_w$ plane for zero external field calculated from Surface Evolver, including the critical line for the side-on to tilted state transition.

$\theta_w > 105°$ and small values of α, the shape of the free energy curve at small tilt angles θ_t becomes increasingly complex such that a simple curvature analysis of the free energy curves at $\theta_t = 0°$, from which α_c is derived, is no longer very meaningful (see last row of Figure 5.10). We have therefore only calculated α_c for contact angles in the range $\theta_w = 75° \rightarrow 105°$. In Figure 5.12, we plot the phase diagram for magnetic cylinders in the $\alpha - \theta_w$ plane for zero external field, including the critical line for the side-on to tilted state transition. Note that the phase diagram in Figure 5.12 looks very different from the one given in ref.[11] because the authors in ref.[11] only considered cylinders in the end-on or side-on states while we have included the possibility of the cylinders being in intermediate tilted states.

Next, from Figures 5.3 and 5.11 and Figure 5.10 we see that for a given

α, increasing θ_w stabilises the end-on state relative to the side-on state, in good agreement with the predictions of Lewandowski et al.[11] However, by analysing all particle orientations and not just the end-on and side-on states, our calculations show that increasing θ_w also causes the end-on state to become *locally* stable, e.g., compare Figure 5.11(a) to Figure 5.11(d) and Figure 5.3(b) to Figure 5.11(b). Indeed for $\alpha = 0.5$, increasing the contact angle from $\theta_w = 100^\circ$ to $\theta_w = 110^\circ$ causes the end-on state to become the globally stable state (Figure 5.11(f)). Thus, by tuning *both* θ_w and α, we can design cylindrical systems with more than two stable orientations and hence create switchable materials with unique magnetic responses that have no analogs in simple paramagnetic or ferromagnetic systems.

We first consider the case $\alpha = 2.5$ and $\theta_w = 110^\circ$ (Figure 5.11(d)). Since $\alpha > \alpha_c$, the side-on state is stable while the fact that $\theta_w = 110^\circ$ means that the two end-on states are also (locally) stable. We therefore have a system with *three* stable orientations in the absence of an external field. The response of this system to an external field is shown in Figure 5.13(a). For definiteness, let us assume that the magnetic cylinder is initially in the negative end-on state ($\theta_t = -90^\circ$) in zero field, i.e., bottom filled circle in Figure 5.13(a). As we increase the external field, the cylinder remains in the negative end-on state until the field is equal to the critical value $\overline{B}_{c1}$, when the cylinder undergoes an irreversible transition to a positive tilted state. At this point, if we decrease the field to zero, we can access the side-on state of the cylinder, i.e., the middle filled circle in Figure 5.13(a). On the other hand, if we increase the field from $\overline{B}_{c1}$, the equilibrium tilt angle will increase until the field is equal to the

critical value $\overline{B}_{c2}$, when the particle undergoes an irreversible transition to the positive end-on state ($\theta_t = 90°$). At this point, if we decrease the field to zero, the positive end-on state remains stable, i.e., top filled circle in Figure 5.13(a). Analogous behaviour to everything discussed above will also occur for $\overline{B} < 0$ (see Figure 5.13(a)).

We next consider the case $\alpha = 1.0$ and $\theta_w = 100°$ (Figure 5.11(b)). Since $\alpha < \alpha_c$, two equivalent tilted states are stable while the fact that $\theta_w = 100°$ means that the two end-on states are also stable. Note that although the dimensionless energy barrier stabilising the end-on states are small ($\Delta\overline{F}_{int} \approx 2.5 \times 10^{-4}$), for micron-sized particles (say $r = 1\mu$m) at an oil/water interface (say $\gamma = 30$mN/m), this barrier corresponds to a value of $4 \times 10^4 k_B T$ so that the end-on state is thermally stable. We therefore have a system with *four* stable orientations in the absence of an external field. The response of this system to an external field is shown in Figure 5.13(b). For definiteness, let us assume that the magnetic cylinder is initially in the negative end-on state ($\theta_t = -90°$) in zero field, i.e., bottom filled circle in Figure 5.13(b). As we increase the external field, the cylinder remains in the negative end-on state until the field is equal to the critical value $\overline{B}_{c1}$, when the cylinder undergoes an irreversible transition to a negative tilted state. At this point, if we decrease the field to zero, we can access the negative tilted state of the cylinder corresponding to the second filled circle from the bottom in Figure 5.13(b). On the other hand, if we increase the field from $\overline{B}_{c1}$, the equilibrium tilt angle will increase until the field is equal to the critical value $\overline{B}_{c2}$, when the particle undergoes an irreversible transition to a positive tilted state. At

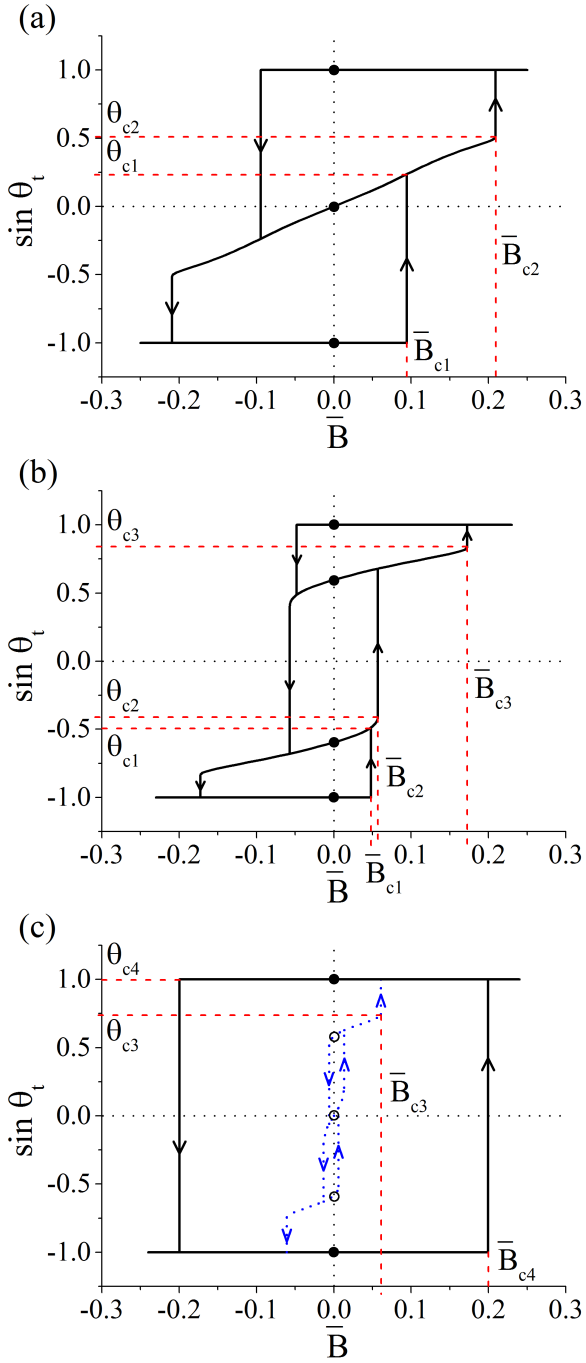

Figure 5.13: Surface Evolver results for the locally stable tilt angle as a function of field strength for cylinders with $\eta = 20$ and different combinations of α and θ_w. (a) $\alpha = 2.5$, $\theta_w = 110°$; (b) $\alpha = 1.0$, $\theta_w = 100°$; (c) $\alpha = 1.0$, $\theta_w = 110°$. The vertical lines represent irreversible orientational transitions, with the direction of the transition indicated by the arrows. For all the other solid lines, it is possible to change the tilt angle along the line in either direction by changing the external field. The filled circles represent locally stable particle orientations at zero field. In (c), the dashed lines and open circles represent parts of the magnetic response that are not accessible once the external field exceeds $\overline{B}_{c3}$. See main text for details.

this point, if we decrease the field to zero, we can access the positive tilted state of the cylinder corresponding to the third filled circle from the bottom in Figure 5.13(b). On the other hand, if we increase the field from $\overline{B}_{c2}$, the equilibrium tilt angle will increase until the field is equal to the critical value $\overline{B}_{c3}$, when the particle undergoes an irreversible transition to a positive tilted state. At this point, if we decrease the field to zero, the positive end-on state remains stable, i.e., top filled circle in Figure 5.13(b). Once again, analogous behaviour to everything discussed above will also occur for $\overline{B} < 0$ (see Figure 5.13(b)).

We now consider the case $\alpha = 1.0$ and $\theta_w = 110^\circ$ (Figure 5.11(e)). The orientational energy landscape in this case is very complex, with *five* stable orientations in the absence of an external field, including the side-on state, two tilted states and two end-on states. However, from the magnetic response of this system in Figure 5.13(c), we see that, regardless of the initial state of the cylinder, once the magnetic field exceeds the critical value $\overline{B}_{c3}$, only the two end-on states (i.e., filled circles in Figure 5.13(c)) are accessible while the other three states (i.e., open circles in Figure 5.13(c)) are no longer accessible. In summary, from the point of view of creating non-volatile switchable materials, the key feature of Figure 5.13 is the fact that it is possible to use both α and θ_w to engineer cylinders that have three or even four locally stable orientations which can be accessed by varying the external field.

We can then assess the feasibility of inducing the above orientational transitions experimentally. For definiteness, we will focus on the three stable state system shown in Figure 5.13(a). For a typical micron-sized system possessing

a permanent magnetic dipole, we use parameters for anisotropic maghemite (γ-Fe_2O_3) particles.[65] Assuming cylinders with radius $r = 1\mu$m and aspect ratio $\alpha = 2.5$, this yields a magnetic dipole moment $m = 5 \times 10^{-12}$A·m^{-2}. The dimensionless critical field for the tilt to perpendicular transition is $\overline{B}_{c2} \approx 0.2$. Using a typical oil/water tension of $\gamma_{ow} = 30$mN/m, this translates to a magnetic field of $B = 0.05$T, which is readily achievable experimentally. Interestingly, the estimated magnetic field required to induce re-orientation of cylindrical particles is of the same order as those predicted in the previous Chapter for ellipsoidal particles made from the same material with a similar size and aspect ratio. This fact points to the generality of the predicted orientational transitions and the feasibility of observing such transitions in a variety of particle shapes.

Finally, although the primary focus of this Chapter has been to use an external field to control the *orientation* of individual cylindrical particles at a liquid interface, since orientation is coupled to meniscus deformation and hence capillary interactions between particles, we can also use an external field to control the *self-assembly* of multiple particle systems. Switchable self-assembly has already been demonstrated in the work of Davies et al. for magnetic ellipsoids[4] and we can exploit the same effect to control the self-assembly of magnetic cylinders. For example, for the three state system shown in Figure 5.13(a), the particles interact with each other via quadrupolar capillary interactions when they are in the side-on state[12] but they do not interact with each other in the end-on state because the meniscus is flat in this case. Similarly, for the four state system shown in Figure 5.13(b), the particles in-

teract with each other via hexapolar capillary interactions when they are in the tilted state (Figure 5.4)[68] but they do not interact with each other in the end-on state. The key advantage of using cylinders instead of ellipsoids in this context is that the switching of the self-assembly for cylinders is again *non-volatile*.

5.4. Conclusion & Future Work

We have studied the influence of an external magnetic field on the orientation of single magnetic cylinders at a liquid interface using a simple flat interface model as well as high resolution Surface Evolver simulations which take into account the deformation of the liquid meniscus around the particle. We have shown that, in the absence of an external field, as we reduce the aspect ratio α of the cylinders below a critical value, the particles undergo spontaneous symmetry breaking from a stable side-on state to one of two equivalent stable tilted states, similar to the spontaneous magnetisation of a ferromagnet going through the Curie point. Similar tilted states have been predicted for Janus particles[3, 16, 50, 51] but to our knowledge this is the first time that their existence has been discussed explicitly for anisotropic colloids with homogeneous surface chemistry.

Furthermore, by tuning both the aspect ratio and contact angle of the cylinder, we have shown that it is possible to engineer particles that have one, two, three or four locally stable orientations and we can induce non-volatile transitions between these states by varying the external field. We found that the magnetic response of systems with one or two stable states is similar to that

of paramagnets and ferromagnets respectively, while the magnetic response of systems with three or four stable states have no analogs in simple magnetic systems. We have also shown that for micron-sized cylinders with realistic magnetic moments, the critical fields required to access the different stable orientations are accessible experimentally.

Finally, although this Chapter focusses on using external fields to control the orientation of individual magnetic cylinders, since particle orientation at a liquid interface is coupled to capillary interactions between particles, it is also possible to use an external field to control the *self-assembly* of multiple cylinders. Therefore, magnetic cylinders at liquid interfaces provide an exciting new approach for creating switchable functional surfaces where we can use an external field to induce multiple *non-volatile* changes in optical, magnetic and mechanical properties. Note that the detailed structure of the self-assembled aggregates is governed by near-field capillary interactions[23, 34, 36] and many body forces[70] but our understanding of how these forces control the self-assembly of anisotropic particles is still at an early stage. For future work, we will study both orientation and capillary deformations in systems consisting of multiple anisotropic particles.

Chapter 6
Self-Assembly of Multiple Ellipsoidal Particles in an External Field

6.1. Introduction

In the previous two chapters, we have seen that for anisotropic particles in an external field, the leading order meniscus deformation is dipolar, as the external field generates a torque on the particle. This meniscus deformation in turn leads to dipolar capillary interactions between the tilted particles which can be switched on and off using an external field.[32] In this Chapter, we study the effect of these switchable dipolar interactions on the self-assembly of multiple ellipsoidal particles.

Before presenting our results in this area, we recall briefly previous results on the self-assembly of multiple tilted particles, see Chapter 2, Section 2.5. Davies and Botto studied the self-assembly of two ellipsoidal particles using Surface Evolver. They only considered a contact angle $\theta_w = 90°$ which means that the deformation of the interface will be dipolar and no quadrupolar deformation due to the particle being anisotropic will be present in the far field. They found that although the side-to-side configuration was the global energy minimum the tip-to-tip configuration was a metastable state.[58] This result seems counter intuitive since in experimental and theoretical studies by Loudet[59] and Botto[23], it was found that side-on ellipsoidal particles approaching each other tip-to-tip, tend to roll into a preferred side-to-side configuration. In order to clarify this surprising result, in this Chapter we revisit the self-assembly of two tilted ellipsoidal particles using Surface Evolver in collaboration with a

summer project student Rizwaan Mohammed.

Davies and Botto also studied the self-assembly of a small number of particles, using lattice-Boltzmann simulations, to find potential global minimum or metastable orientations for three or more particles tilted at the interface, see results in Chapter 2, Section 2.5, Figure 2.13. They found the particles forming ring-like structures in tip-to-tip configurations, with $3, 4, 5$ and 6 particles seeming to preferentially align tip-to-tip rather than side-to-side as has been observed experimentally for a large number of ellipsoidal particles.[58, 59] The problem with lattice-Boltzmann is that there is a small degree of inherent noise present in the system limiting the resolution of the method close to any transitions, as we have already seen in Chapter 4, Section 4.3. Results for three ellipsoidal particles have been presented using lattice-Boltzmann simulations, where three pronged propellor like shapes have been found to be a stable orientation for many ellipsoidal particles[32] and for three randomly arranged particles.[58] In order to overcome this problem, we present preliminary results for the self-assembly of three tilted ellipsoidal particles using Surface Evolver. An earlier work of Fournier and Galatola[70] studied the capillary attraction and equilibrium configurations of near spherical particles. They were the first to include many-body interactions in their calculations to find equilibrium configurations and interestingly found metastable states for three and four particles that are purely due to these many body effects. This confirmed that many body effects and higher-order multipoles contribute significantly to the deformation of the interface when close to the particle surface.[70]

Davies et al. studied the self-assembly of multiple ellipsoidal particles using

lattice-Boltzmann simulations.[32] They found that they could tune the dipolar capillary interactions by varying the dipole-field strength and induce a first order phase transition by exceeding a critical field strength which then turned the dipolar interactions off as there is no deformation when the particle is perpendicular to the interface, see Chapter 2, Section 2.5, Figure 2.12.[32]

6.2. Theoretical Model

In this section we outline the Surface Evolver model used to investigate two and three tilted ellipsoidal particles at a liquid interface. We also present the interaction potential between capillary dipoles in elliptical coordinates which was developed by Dr. Lorenzo Botto, Queen Mary University London.

In Figure 6.1 we introduce key parameters needed for our Surface Evolver simulations. Figure 6.1(a) shows a side view of an ellipsoidal particle with the particle tilted with respect to the interface at a tilt angle θ_t. In Figure 6.1(b) we show a top view looking down on two ellipsoidal particles that have arbitrary bond angles $\theta_{b1,}\, \theta_{b2}$ with their centres separated by an arbitrary length r_{12}. In Chapter 3 we presented the coordinate transformations required to change the tilt angle and bond angle of the particles. We apply these coordinate transformations in our Surface Evolver code here. A thorough investigation of the lowest free energy of the system for varying θ_b and θ_t would be computationally expensive. Therefore, we explore a restricted view for varying the bond angle in a mirror symmetric configuration i.e. $\theta_b = \theta_{b1}$, $\theta_{b2} = \pi - \theta_b$. From the polar expression for the dipolar interaction, Equation 6.2, the interaction potential is minimized when $\theta_{b1} + \theta_{b2} = \pi$ i.e. mirror symmetric configuration.

For mirror symmetric configuration, the capillary force is attractive. Therefore, we expect particles in minimum energy configuration to be in contact. The centre-to-centre distance r_{c-c} for the particles in closest contact clearly depends on both the bond angle θ_b and the tilt angle θ_t. To derive an analytical expression for r_{c-c}, we express the surface of the ellipsoidal particles in terms of the local coordinate system x'', y'', z'' which is aligned along the principle axes of the ellipsoid

$$f(x,y,z) = \left(\frac{x''^2}{r^2}\right) + \left(\frac{y''^2}{l^2}\right) + \left(\frac{z''^2}{r^2}\right) = 1 \tag{6.1}$$

where x'', y'', z'' are expressed in terms of the lab frame coordinate system x, y, z see Section 3.2 in Chapter 3, r is the semi-minor axes of the ellipsoids and l is the length of the ellipsoid. Note that in Equation 6.1, we assume y'' is aligned along the long axis of the ellipsoid. The surface normal vector is given by $\underline{\nabla} f$. At contact the x and z components of $\underline{\nabla} f$ are zero, i.e. $\frac{\partial f}{\partial x}$, $\frac{\partial f}{\partial z} = 0$. Together with Equation 6.1 this gives us three simultaneous equations which can be solved to find the contact coordinates with the y contact coordinate yielding r_{c-c}. The final expression for r_{c-c} is rather long and is given in Appendix D. In Figure 6.1(c) we show the top view looking down on two ellipsoidal particles in a mirror symmetric configuration with bond angles θ_b and centre-to-centre distance at contact, $r_{12} = r_{c-c}$. In (d) we define an exclusion zone of thickness $\Delta/2$, which is used because simulating particles in contact causes numerical issues for Surface Evolver. By simulating varying values for Δ, the results can then be extrapolated to contact. In this Chapter, we use a constant $\Delta = 0.1r$. By varying Δ, we estimate that the interaction energies calculated using this

value of Δ agrees with the contact value to within 2% .

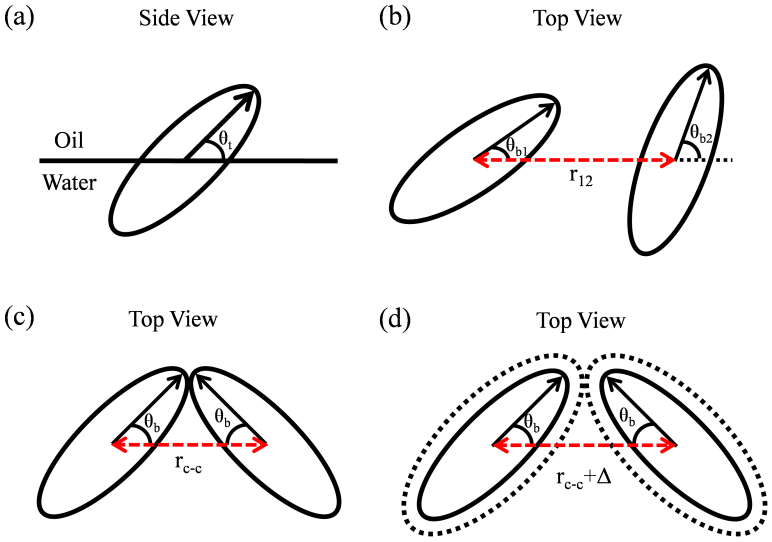

Figure 6.1: (a) Side view of an ellipsoid tilted with respect to the oil-water interface (b) Top view of two ellipsoidal particles showing arbitrary bond angles θ_{b1} and θ_{b2} with centres of the particles separated by length r_{12} (c) mirror symmetric configuration with bond angles θ_b with a centre-to-centre distance r_{c-c} (d) mirror symmetric configuration with an exclusion zone Δ needed for the simulation in Surface Evolver, see text for details.

In our Surface Evolver simulations we consider two ellipsoidal particles with an aspect ratio $\alpha = 2$, a semi-minor axis $r = 1$ and a contact angle $\theta_w = 90°$. Therefore, there is no quadrupolar deformation due to a constant contact angle constraint. Figure 6.2 shows our Surface Evolver output for these two ellipsoidal particles; (a) is a side-view showing the resulting deformation when the particles are at a tilt angle $\theta_t = 15°$ and bond angle $\theta_b = 0°$. (b)-(d) are top views showing the effect of varying bond angle θ_b. (b) $\theta_b = 0°$ represents a tip-to-tip configuration, (c) $\theta_b = 45°$ represents an intermediate bond angle and finally (d) $\theta_b = 90°$ represents the side-to-side configuration. In all our simulations θ_b is varied from $0° \rightarrow 90°$ in $5°$ steps.

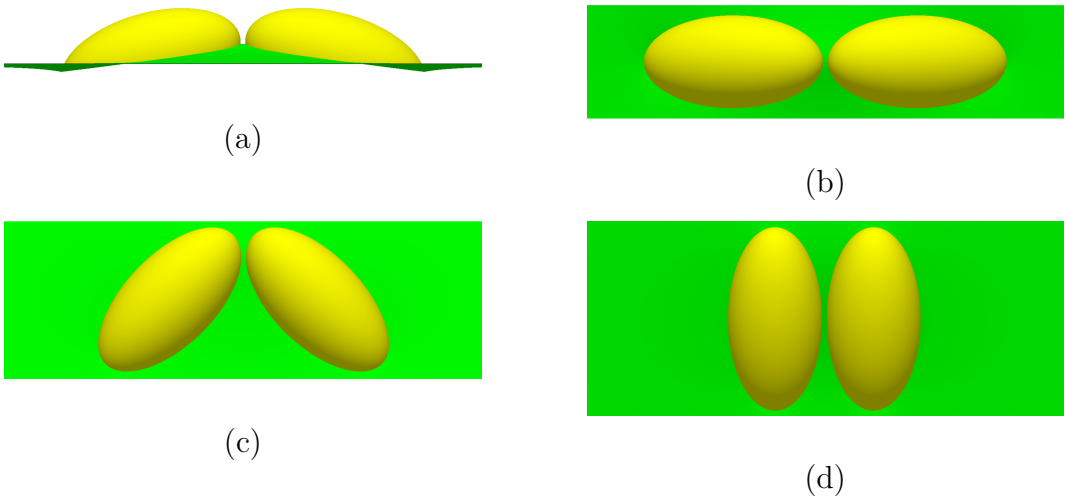

Figure 6.2: Surface Evolver simulation output for two ellipsoidal particles with aspect ratio $\alpha = 2$, tilt angle $\theta_t = 15°$ and $\Delta = 0.1r$ (a) side view to show the ellipsoids tilted in a tip-to-tip configuration $\theta_b = 0°$ (b)-(d) top view to show (b) tip-to-tip orientation $\theta_b = 0°$ (c) intermediate bond angle $\theta_b = 45°$ (d) side-to-side orientation$\theta_b = 90°$.

The number of variables required to fully specify an arbitrary configuration of three tilted ellipsoidal particles is even larger, i.e. three bond angles and two centre-to-centre distances. In order to make a Surface Evolver analysis of three tilted ellipsoidal particles tractable, we restrict ourselves to the subset of three particle configurations shown in Figure 6.3.

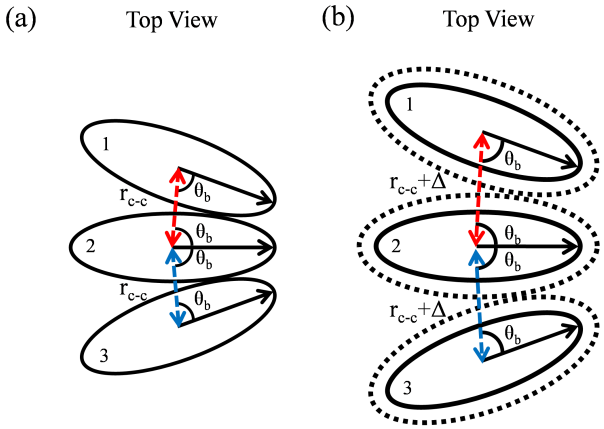

Figure 6.3: Top view of three ellipsoidal particles showing (a) mirror symmetric configuration with bond angles θ_b and a centre-to-centre distance r_{c-c} (b) mirror symmetric configuration with an exclusion zone Δ needed for the simulation in Surface Evolver, see text for details.

For three ellipsoidal particles in Surface Evolver we simulate an exclusion zone $\Delta = 0.1r$, see Figure 6.3b. The particles have an aspect ratio $\alpha = 2$, with a semi-minor axis $r = 1$ and a contact angle $\theta_w = 90°$. Figure 6.4 shows our Surface Evolver output for these three ellipsoidal particles; (a) is a side-view showing the resulting deformation when the particles are at a tilt angle $\theta_t = 15°$ and a bond angle $\theta_b = 90°$. (b)-(d) are top views showing the effect of varying bond angle θ_b. (b) $\theta_b = 90°$ represents a side-to-side configuration, (c) $\theta_b = 60°$ represents an intermediate bond angle and finally (d) $\theta_b = 30°$ represents the tip-to-tip configuration. In all our simulations θ_b is varied from $30° \rightarrow 90°$ in $5°$ steps. For details on how the particles tilt and bond angles are implemented, see Chapter 3.

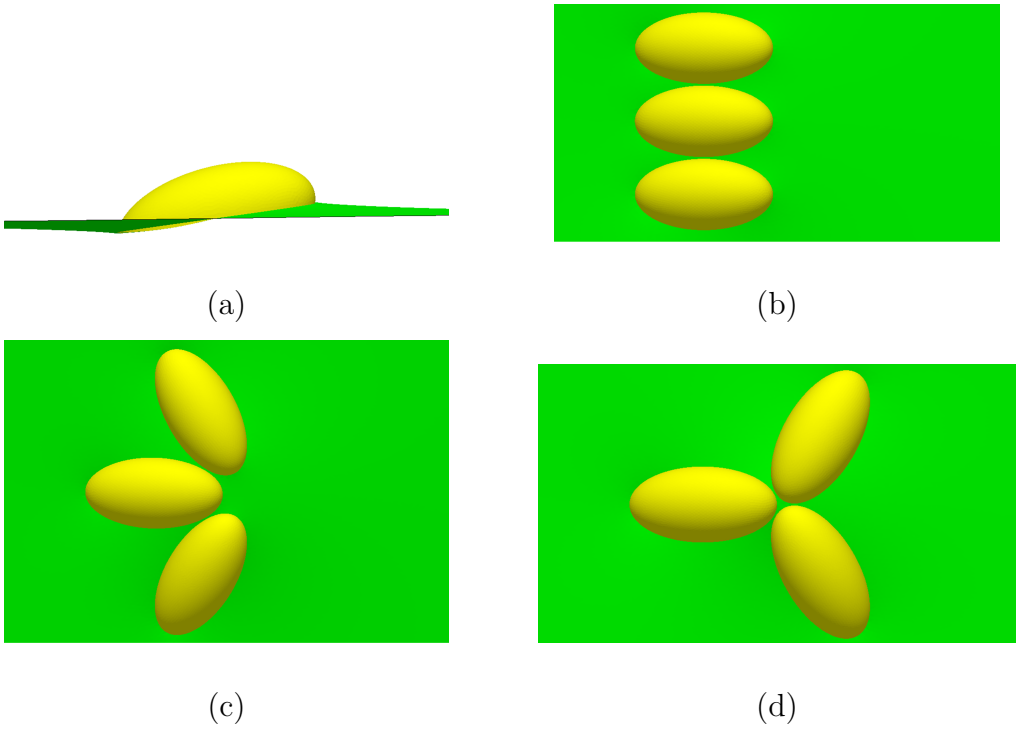

Figure 6.4: Surface Evolver simulation output for three ellipsoidal particles with aspect ratio $\alpha = 2$, tilt angle $\theta_t = 15°$ and $gap = 0.1r$ (a) side view to show the ellipsoids tilted in a tip-to-tip configuration $\theta_b = 90°$ (b)-(d) top views showing (b) side-to-side bond angle $\theta_b = 90°$ (c) intermediate bond angle $\theta_b = 60°$ (d) tip-to-tip bond angle $\theta_b = 30°$.

As well as using Surface Evolver to analyse the equilibrium orientation we use an analytical theory for pair interactions between capillary dipoles in elliptical coordinates. Elliptical coordinates are used rather than polar coordinates because in a mirror symmetric configuration the particles have the same energy independent of bond angle θ_b, Equation 2.15 in Chapter 2. Therefore, in order to distinguish between the side-to-side ($\theta_b = 90°$) and tip-to-tip ($\theta_b = 0°$) orientation we use elliptical coordinates. These results were derived by Dr Lorenzo Botto at Queen Mary University London and are included in this thesis for completeness. The dipolar capillary interactions between two tilted ellipsoids which are arbitrarily orientated with respect to each other (Figure 6.1) will depend on θ_t, θ_{b1}, θ_{b2}, r_{12}. In polar coordinates, the dipolar capillary interaction is[58, 68]

$$U_{polar}\left(\theta_t\, \theta_{b1},\, \theta_{b2},\, r_{12}\right) = \gamma_{12} 2\pi H_e\left(\theta_t\right)^2 \frac{R_c^2}{r_{12}^2} \cos\left(\theta_{b1} + \theta_{b2}\right) \tag{6.2}$$

where γ_{12} is the surface energy between fluid 1 and fluid 2, $H_e\left(\theta_t\right)$ is the amplitude of the contact line undulation which is a function of θ_t, R_c is the nominal contact line radius, r_{12} is the centre-to-centre separation and θ_{b1} and θ_{b2} are the bond angles.

In elliptical polar coordinates, Dr L. Botto has derived the expressions for dipolar potential with the form

$$U_{ellip}\left(\theta_t\, \theta_{b1},\, \theta_{b2},\, r_{12}\right) = -\gamma_{12} 2\pi H_e\left(\theta_t\right)^2 R_c^2 f\left(\theta_{b1},\, \theta_{b2},\, r_{12}\right) \tag{6.3}$$

$f\left(\theta_{b1},\, \theta_{b2},\, r_{12}\right)$ is a function of θ_{b1}, θ_{b2}, r_{12}; the expression is long and it is

presented in Appendix E.

For large r_{12}, U_{ellip} should agree with dipolar potential in polar coordinates $U_{polar}\left(\theta_t\, \theta_{b1},\, \theta_{b2},\, r_{12}\right)$ Equation 6.2. In Figure 6.5 we plot a log graph for both U_{ellip} and U_{polar} for varying separation of r_{12} and find good agreement for the polar and elliptical expressions for large r_{12}.

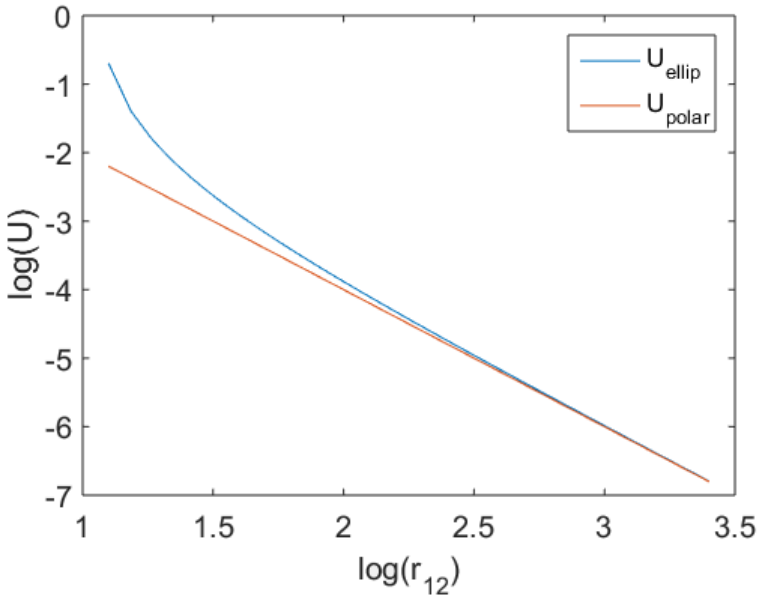

Figure 6.5: log graph for two ellipsoidal particles for an aspect ratio $\alpha = 3$ comparing U_{ellip} and U_{polar} for varying r_{12}

For the three particle configurations shown in Figure 6.3, assuming all interactions are pairwise additions (i.e. neglecting many body effects), the total interaction potential is

$$U_{tot}\left(\theta_t,\, \theta_b\right) = -\gamma_{12} 2\pi H_e \left(\theta_t\right)^2 R_c^2 2\left(f\left(\theta_{b1},\, \theta_{b2},\, r_{12}\right)\right) + f\left(\theta_{b3},\, \theta_{b4},\, rr_{12}\right) \quad (6.4)$$

where $\theta_{b3} = 2\theta_{b1} - \frac{\pi}{2}$, $\theta_{b4} = \pi - \theta_{b3}$ and $rr_{12} = 2r_{12}\sin\theta_{b1}$. We require two lots of $f\left(\theta_{b1},\, \theta_{b2},\, r_{12}\right)$ as particles 1 & 2 and 2 & 3 interact with each

other, see Figure 6.3. We then need to add $f(\theta_{b3}, \theta_{b4}, rr_{12})$ as particles 1 & 3 also interact with one another. We will use U_{ellip} and U_{tot} to analyse the stability of the two particle configuration in Figure 6.7 and the three particle configurations in Figure 6.8 respectively.

6.3. Results & Discussion

We first considered two ellipsoidal particles at a liquid interface because we wanted to confirm whether the local energy minimum for a tip-to-tip configuration presented in a recent paper by Davies et al. is correct.[58] For our Surface Evolver model we used the same constraints outlined in Chapter 3 to represent the ellipsoidal particles and outer simulation domain. In Figure 6.6 we plot the total free energy (relative to the free energy at $\theta_b = 90°$) as a function of the particles bond angle θ_b at a tilt angle $\theta_t = 5°$ for particles in a mirror symmetric configuration (i.e. Figure 6.1). The particles have an aspect ratio of $\alpha = 2$ with an exclusion zone $\Delta = 0.1r$. In contrast to the results of Davies and Botto,[58] our results showed no local minima for the tip-to-tip configuration. To check if there was a mistake in our code, we contacted the authors who sent us their Surface Evolver program for further investigation. In collaboration with Rizwaan Mohammed (summer project student) we have used the Surface Evolver code of Davies and Botto, which has a different setup and minimisation scheme, to carry out the same calculations. As shown in Figure 6.6, their simulation code (red dashed curve) gave exactly the same result as ours, i.e. there is only one minimum corresponding to a side-to-side configuration.

From this analysis, we conclude that there is an error in their post processing procedure. It is worth noting that no local minima for the tip-to-tip configuration was found by Botto et al. [23] for ellipsoidal particles in contact with aspect ratio $\alpha = 3$, contact angle $\theta_w = 80°$ and tilt angle $\theta_t = 0°$. Experimentally, Loudet et al. also found that identical ellipsoidal particles in the tip-to-tip configuration tend to roll into the side-to-side configuration.[59] Davies and Botto are currently investigating why their earlier simulations yielded a local minimum at the tip-to-tip configuration.

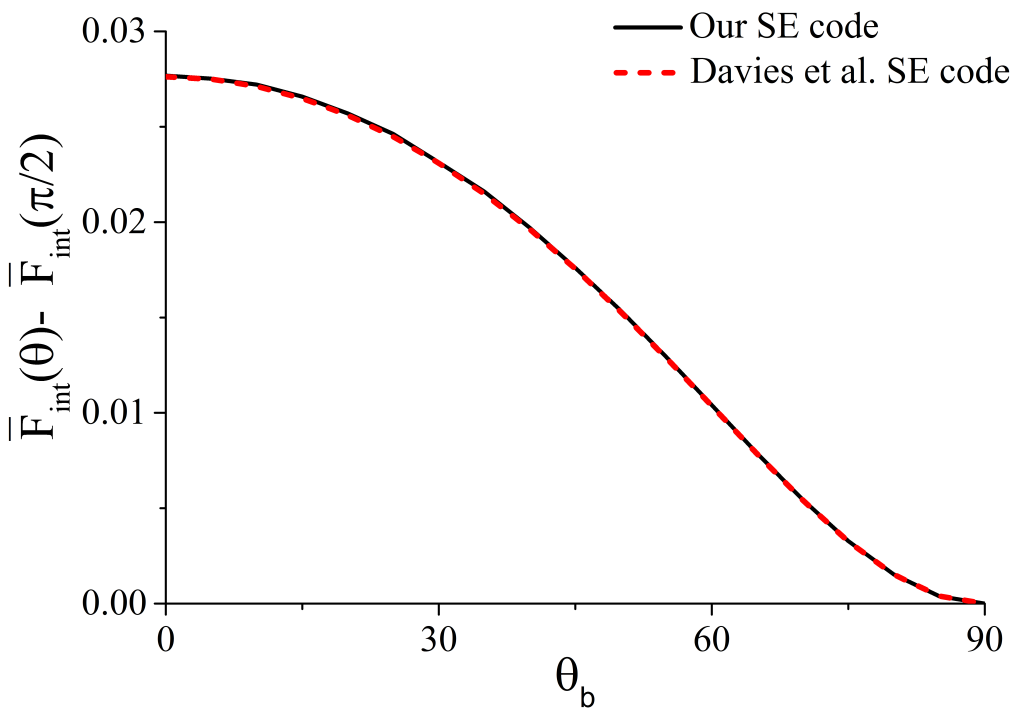

Figure 6.6: Comparison between two different Surface Evolver codes (our Surface Evolver code is black solid line, with Davies and Botto code the red dashed line) for the dimensionless free energy as a function of bond angle relative to the side-to-side state ($\theta_b = 90°$) for two ellipsoids with aspect ratio $\alpha = 2$, tilt angle $\theta_t = 5°$ and $gap = 0.1r$.

As we have now confirmed that our Surface Evolver program appears to be correct, in Figure 6.7 we plot the total free energy (relative to the free energy at $\theta_b = 90°$) as a function of the particles bond angle θ_b with aspect ratio

$\alpha = 2$ and exclusion zone $\Delta = 0.1r$ for three different tilt angles; $\theta_t = 5°$(in red), $\theta_t = 10°$(in green) and $\theta_t = 15°$(in blue). All of our Surface Evolver simulations (dashed line in Figure 6.7) show that the lowest free energy of the system is always the side-to-side configuration for two identical ellipsoidal particles independent of θ_t. Also plotted in Figure 6.7 is the analytical theory in elliptical coordinates for capillary dipoles $U_{ellip}\left(\theta_b - \theta_b,\, r_{c-c} + \Delta\right)$ (solid line). Given that there are no fitting parameters in the analytical theory, the agreement between the Elliptical Potential and the Surface Evolver results is remarkably good. This means that we can use our analytical theory to pick up the qualitative and even semi-qualitative features for two ellipsoidal particles in or close to contact. This theory will therefore be invaluable for a more thorough investigation of the energy landscape of two ellipsoidal particles, as it will allow us to identify the interesting minimum energy configurations in addition to the mirror symmetric configurations considered here, without using expensive computational simulations to find them.

To calculate $H_e\left(\theta_t\right)$ we used our single ellipsoidal particle code with an aspect ratio $\alpha = 2$ for varying tilt angle. This is in fact an approximation since when two ellipsoids approach each other, H_e will be modified due to non-linear interactions between the two particles. The results for H_e for different θ_t are presented in Table 6.1 where we see that H_e increases with increasing θ_t. However, since $H_e = 0$ for $\theta_t = 90°$, H_e will go through a maximum at some intermediate value of θ_t between 0° and 90°.

Next, we investigate three ellipsoidal particles at a liquid interface varying the bond angle, going from a syzygy of ellipsoidal particles (aligned in a side-

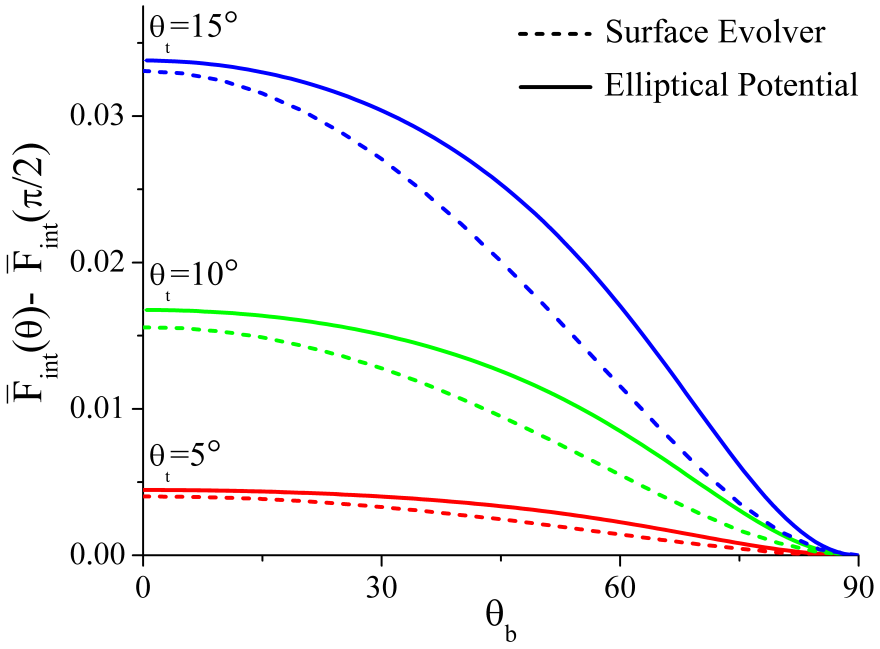

Figure 6.7: Energy profile as a function of the bond angle θ_b for two particles in a mirror symmetric configuration (i.e. Figure 6.1) with a separation between particles $\Delta = 0.1r$ with aspect ratio $\alpha = 2$ for tilt angles $\theta_t = 5°$(red), $\theta_t = 10°$(green), $\theta_t = 15°$(blue). Surface Evolver simulation results are represented by the dashed line and the analytical theory by the solid line.

$\theta_t/°$	H_e
5	0.087231
10	0.170368
15	0.245471

Table 6.1: Surface Evolver simulation to calculate the amplitude of the contact line for a single ellipsoidal particle tilted with respect to the interface

to-side configuration $\theta_b = 90°$) to a three pronged propellor shape of the three particles in a tip-to-tip configuration $\theta_b = 30°$, see Figure 6.4. In Figure 6.8 we plot the total free energy (relative to the free energy at $\theta_b = 90°$) as a function of the particles' bond angles θ_b with aspect ratio $\alpha = 2$ and exclusion zone $\Delta = 0.1r$ for three different tilt angles; $\theta_t = 5°$(in red), $\theta_t = 10°$(in green) and $\theta_t = 15°$(in blue). We can see that the lowest free energy of the system is when the particles are in a side-to-side configuration. However, in contrast

to the two particle case we also find that the tip-to-tip configuration is now a metastable state. This agrees with Davies et al. lattice-Boltzmann simulations that found stable three particle tip-to-tip configurations (see Figure 2.13 from Chapter 2).[4, 58]

Again we can compare our Surface Evolver results (dashed line) with the elliptical potential results (solid line) and find that the elliptical potential captures the qualitative features of the energy landscape correctly. Specifically, it shows that a metastable tip-to-tip orientation is indeed present. However, in contrast to the two particle case , we find a larger difference between the simulation and analytical theory. This discrepancy is presumably due to non-linear effects (the contact line will move different to the predictions for a single ellipsoidal particle, therefore affecting H_e used in the analytical theory) and also because of many-body effects which are not taken into account in the analytical theory which uses the summation of pairwise interactions. The pairwise approximation is not necessarily correct for particles in close contact, as found by Fournier and Galatola.[70] Nevertheless, our results suggest that the analytical theory is accurate enough to help us to identify interesting minimum energy configurations for three particles. This is very useful since an exhaustive exploration of the energy landscape of three particles using Surface Evolver is computationally prohibitive.

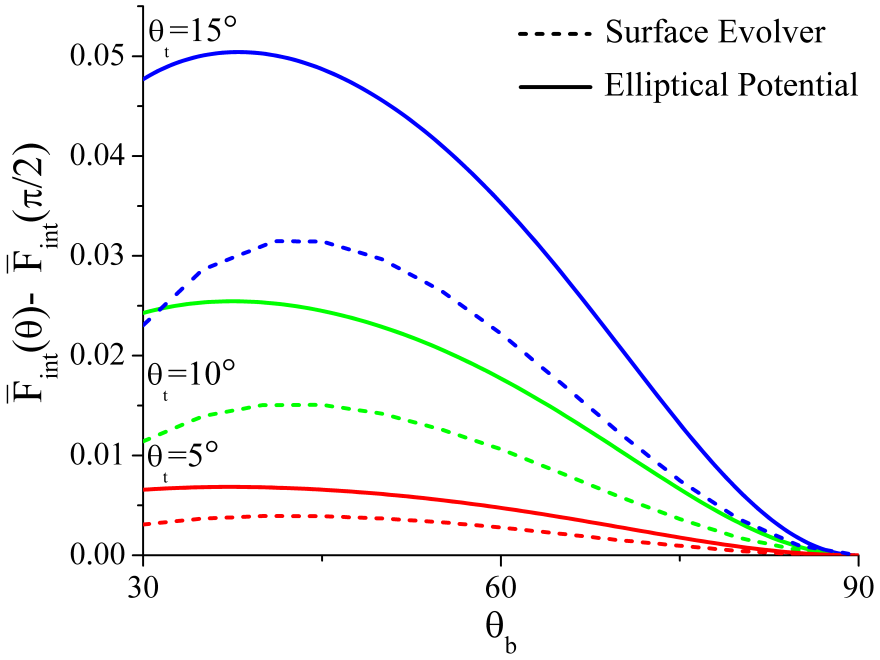

Figure 6.8: Energy profile as a function of the bond angle for three particles with a separation between particles $\Delta = 0.1r$ with aspect ratio $\alpha = 2$ for tilt angles $\theta_t = 5°$(red), $\theta_t = 10°$(green), $\theta_t = 15°$(blue). Surface Evolver simulation results are represented by the dashed line and the analytical theory by the solid line.

6.4. Conclusion & Future Work

In this Chapter we have studied the interactions between two and three ellipsoidal particles that are tilted with respect to the interface for varying bond angles. The dipolar capillary interactions for two ellipsoidal particles have been studied previously by Davies and Botto.[58] However, we found discrepancies between the results of Davies and Botto and our results. Specifically, we did not find a metastable tip-to-tip configuration for two ellipsoidal particles. Having rerun their simulation code, we conclude that there is in fact a mistake in the results of Davies and Botto and the metastable tip-to-tip configuration is spurious. This discrepancy is currently being investigated by the authors.

For two identical ellipsoidal particles we found that the most stable orientation is a side-to-side orientation. For three ellipsoidal particles the global energy minimum is again for the side-to-side orientation. However, we found that the tip-to-tip configuration (similar to a three pronged propellor) to be a local minimum. We have also compared our Surface Evolver simulation to the theoretical model for the dipolar interaction potential in elliptical coordinates. Both Surface Evolver and the elliptical potential showed good semi-quantitative agreement for two ellipsoidal particles with no fitting parameters. For three ellipsoidal particles, there is qualitative agreement between the Surface Evolver simulation and the analytical theory. In particular both simulation and theory predict that the side-to-side configuration is the global minimum, but the tip-to-tip configuration is now a metastable state. However, larger quantitative discrepancies between Surface Evolver and the elliptical potential are present for three ellipsoidal particles. We attribute these discrepancies to non-linear and many-body effects.[70]

The logical progression for multiple ellipsoidal particles is to investigate four or more particles at a liquid interface. At some point the tip-to-tip configuration will become the global minimum of the system rather than the side-to-side orientation which we have found to be the global minimum for two and three particles. Davies et al. used lattice-Boltzmann simulations to find equilibrium clusters for three or more particles, Chapter 2 Figure 2.13, which shows that the tip-to-tip configuration either becomes a locally stable orientation, as we have found for a three particle system, or possibly the global minimum for four or more ellipsoidal particles. In this Chapter, we found that for two el-

lipsoidal particles the side-to-side orientation will always be favoured. Also, for three particles the side-to-side orientation is the global minimum but there is a local minima with the particles in a tip-to-tip configuration. For multiple ellipsoidal particles the metastable tip-to-tip configuration, found for three particles, should eventually become the lowest free energy of the system for more ellipsoidal particles, which is why simulating four or more particles is the next extension of this work currently being studied by our summer student Rizwaan.

Finally, for multiple ellipsoids we simulated a restricted mirror symmetric configuration by varying bond angle by the same amount for all particles. In an interesting work by Fournier and Galatola, who examined thoroughly the energy landscape for three and four near circular particles, they found metastable structures for a variety of configurations at similar energies. Following a similar approach it would be worthwhile simulating multiple ellipsoidal and cylindrical particles to give us a greater understanding of the self-assembled structures formed.[70] Using an analytical theory to focus on the most intriguing configurations for varying the bond, tilt and contact angles would reduce the cost of expensive computational simulations.

Chapter 7
Conclusions & Future Work

7.1. Conclusions

In this thesis we investigated the orientation, capillary forces and self-assembly of ellipsoidal and cylindrical colloidal particles at liquid interfaces under the influence of an external field. This was investigated theoretically using both analytical theory and finite element simulations.

In Chapter 4 we used Surface Evolver to study the orientational transitions of an ellipsoidal magnetic particle adsorbed at a liquid interface, explicitly accounting for the deformation of the liquid meniscus around a particle. We found that when the magnetic field is increased beyond a critical field, the particles undergo a discontinuous transition to the perpendicular state to align the embedded magnetic dipole with the magnetic field. Our results confirmed the orientational transition predicted by Bresme and Faraudo who used a simplified model which assumed a flat liquid interface and we demonstrated the importance of accounting for deformation of the interface results which were in agreement with lattice-Boltzmann simulations.[32] We also showed that there is significant hysteresis in the orientational transition of micron-sized ellipsoidal particles due to the very large energy barriers that exist between the tilted and perpendicular states for the system. This hysteresis is in fact also predicted by the model of Bresme and Faraudo but has not been explicitly discussed previously. Furthermore, we demonstrated that critical fields can be readily tuned by a factor of 3 to 4 by changing the aspect ratio or contact angle of the magnetic particles.

In Chapter 5 we studied the influence of an external magnetic field on the orientation of single magnetic cylinders at a liquid interface using a simple flat interface model and comparing these to high resolution Surface Evolver simulations which account for the deformation of the liquid meniscus around the particle. We have shown that, in the absence of an external field, as we reduce the aspect ratio α of the cylinders below a critical value, the particles undergo spontaneous symmetry breaking from a stable side-on state to one of two equivalent stable tilted states. To our knowledge this is the first time that their existence has been discussed explicitly for anisotropic colloids with homogeneous surface chemistry. By tuning both the aspect ratio and contact angle of the cylinder, we showed that it is possible to engineer particles that have one, two, three or four locally stable orientations and we are able to access these states by varying the external field. For micron-sized cylinders with realistic magnetic moments, the critical fields required to access the different stable orientations are accessible experimentally.

In Chapter 6 we studied the interactions between two and three ellipsoidal particles that are tilted with respect to the interface for varying bond angles. For two identical ellipsoidal particles we found that the most stable orientation is a side-to-side orientation. For three ellipsoidal particles the global energy minimum is again for the side-to-side orientation. However, we found that the tip-to-tip configuration (similar to a three pronged propellor) to be a local minimum. We compared our Surface Evolver simulation to the theoretical model for the dipolar interaction potential in elliptical coordinates. Both Surface Evolver and the elliptical potential showed good semi-quantitative agreement

for two ellipsoidal particles with no fitting parameters. For three ellipsoidal particles, there is qualitative agreement between the Surface Evolver simulation and the analytical theory. In particular both simulation and theory predict that the side-to-side configuration is the global minimum, but the tip-to-tip configuration is now a metastable state. However, larger quantitative discrepancies between Surface Evolver and the elliptical potential are present for three ellipsoidal particles and we attribute these discrepancies to non-linear and many-body effects.

7.2. Future Work

In Chapters 4 and 5 we investigated the effect an external field has on the orientational transition for isolated ellipsoids and cylinders. Looking at the effect multiple particles have on this orientational transition and the potential hysteresis of the system is a logical next step. Understanding how the orientational transition is affected by the presence of many ellipsoidal/cylindrical particles will lead to a better understanding of how to manipulate anisotropic particles into directed self-assembled structures.

For multiple ellipsoids we simulated a restricted mirror symmetric configuration by varying bond angle by the same amount for all particles. Completing a more thorough examination of the energy landscape for multiple ellipsoidal and cylindrical particles to give us a greater understanding of the self-assembled structures formed would be beneficial. To reduce the cost of computational simulations it would be best to use the analytical theory to focus on the most intriguing configurations for varying the bond, tilt and contact angles.

The logical progression for multiple ellipsoidal particles is to investigate four or more particles at a liquid interface. At some point the tip-to-tip configuration will become the global minimum of the system rather than the side-to-side orientation which we have found to be the global minimum for two and three particles. Looking at multiple cylindrical particles and their preferred orientation will also be interesting as ellipsoids and cylinders behave differently.

Appendix A
Surface Evolver Sphere Program

```
#define radp 1 //radius of the particle

  //define the tension to represent the contact angle using Young's equation

  PARAMETER angle = 90

  PARAMETER tens = (cos(angle*pi/180))

  //set as a parameter so that it can be changed at runtime

  //define equation to represent the sphere

  constraint sphere

  formula: (x^2 + y^2 + z^2 = radp^2)

  // fix outer edge of the interface

  constraint xc1

  formula: x=-15

  constraint xc2

  formula: x=15

  constraint yc1

  formula: y=-15

  constraint yc2

  formula: y=15

  vertices

  //oil-water interface

  1 -radp -radp 0 constraint sphere

  2 radp -radp 0 constraint sphere

  3 radp radp 0 constraint sphere
```

4 -radp radp 0 constraint sphere

//particle

5 0 0 radp constraint sphere // one vertex representing the p-o surface

//outer square simulation domain

6 -15 -15 0 constraints xc1, yc1

7 15 -15 0 constraints xc2, yc1

8 15 15 0 constraints xc2, yc2

9 -15 15 0 constraints xc1, yc2

edges

//oil-water interface

1 1 2 constraint sphere

2 2 3 constraint sphere

3 3 4 constraint sphere

4 4 1 constraint sphere

//particle/oil interface

5 1 5 constraint sphere

6 2 5 constraint sphere

7 3 5 constraint sphere

8 4 5 constraint sphere

//outer simulation

9 6 7 constraint yc1

10 7 8 constraint xc2

11 8 9 constraint yc2

12 9 6 constraint xc1

```
//particle

13 6 1

14 7 2

15 8 3

16 9 4

faces

//oil-water interface

1 9 14 -1 - 13 color green

2 10 15 -2 -14 color green

3 11 16 -3 -15 color green

4 12 13 -4 -16 color green

//particle-oil interface

5 1 6 -5 color yellow constraint sphere tension tens

6 2 7 -6 color yellow constraint sphere tension tens

7 3 8 -7 color yellow constraint sphere tension tens

8 4 5 -8 color yellow constraint sphere tension tens
```

Appendix B
Numerical Method for Determining Magnetic Response of Particles

In our study, the magnetic response of the system, including the stationary tilt angles (i.e., tilt angles corresponding to local minima or maxima in the free energy) for a given magnetic field, and the magnetic fields and tilt angles at the binodal points or points where irreversible orientational transitions occur (including spinodal points) are determined by solving Equation 5.3 in Chapter 5. To illustrate this method, in Figure B.1, we plot $\frac{1}{\cos\theta_t}\frac{\partial\overline{F}_{st}}{\partial\theta_t}$ for different state points, with (a) and (b) corresponding to state points reported in Figure 5.5 (a) & (c) and (e),(d), (f) corresponding to state points reported in Figure 5.13(a), (b), (c). For an arbitrary magnetic field $\overline{B}$, which is represented by a horizontal line in Figure B.1, the intersection of the horizontal line with the $\frac{1}{\cos\theta_t}\frac{\partial\overline{F}_{st}}{\partial\theta_t}$ curve corresponds to either a local minimum or maximum of the free energy curve. The binodal tilt angles are obtained from the intersection between the $\overline{B}=0$ line and the $\frac{1}{\cos\theta_t}\frac{\partial\overline{F}_{st}}{\partial\theta_t}$ curve (filled circles in Figure B.1(b and d)). On the other hand, the maxima and minima in the $\frac{1}{\cos\theta_t}\frac{\partial\overline{F}_{st}}{\partial\theta_t}$ curves correspond to the field strengths and tilt angles where local maxima and minima in the free energy curve merge, i.e., where local minima disappear. We can therefore use the the maxima or minima of the $\frac{1}{\cos\theta_t}\frac{\partial\overline{F}_{st}}{\partial\theta_t}$ curves to determine the spinodal points (open circles in Figure 5.3(b and d)) or the position of the irreversible orientational transitions at higher fields. This is illustrated in the plots in Figure B.1, where the critical angles and field strengths for the state points reported in Figures 5.5 and 5.13 of Chapter 5 are explicitly labelled.

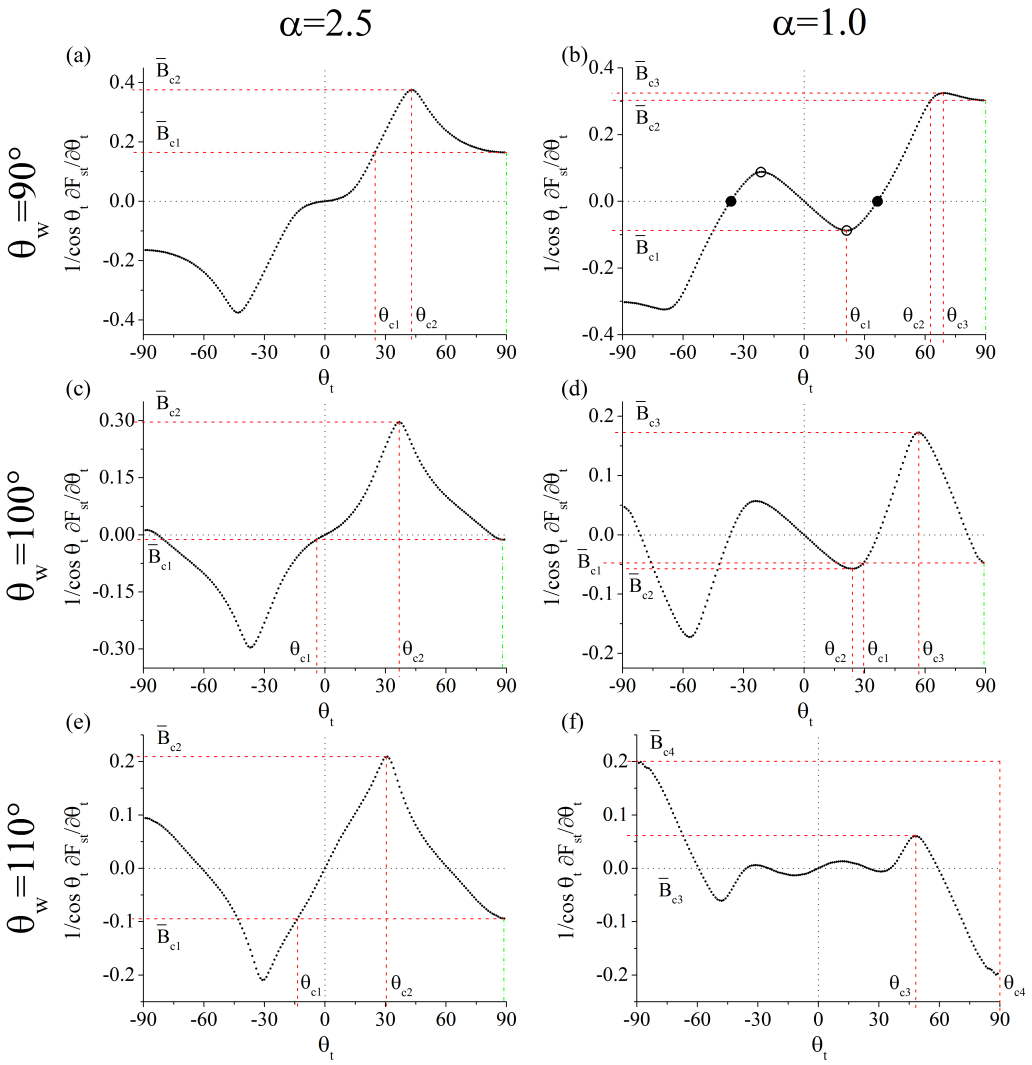

Figure B.1: Surface Evolver results for $\frac{1}{\cos\theta_t}\frac{\partial \bar{F}_{st}}{\partial \theta_t}$ vs. θ_t for cylinders with $\eta = 20$ for different combinations of contact angles θ_w and aspect ratios α. The critical field strengths and tilt angles where the cylindrical particles undergo an irreversible transition to a different local minima correspond to the maxima or minima of the curves and are explicitly labelled. The filled and open circles in (b) refer to the binodal and spinodal points respectively. See main text for details.

Numerical values from Surface Evolver simulations for the binodal and spinodal points for neutrally wetting cylinders with different aspect ratios are in Table B.1.

α	$\theta_0(^\circ)$	$\theta_{c1}(^\circ)$	$\overline{B}_{c1}$
2.0	13.0	7.6	0.007
1.5	23.1	14.1	0.034
1.0	36.4	21.1	0.088
0.5	60.8	30.7	0.213
0.25	82.6	42.0	0.370

Table B.1: Surface Evolver results for binodal tilt angles θ_0 and spinodal points $(\theta_{c1}, \overline{B}_{c1})$ for neutrally wetting cylinders with different aspect ratios α.

Appendix C
Accuracy of Approximating Cylinders as Super-Ellipsoids

As discussed in Chapter 5, one numerical problem when analysing the orientational behaviour of cylinders is the fact that Surface Evolver becomes unstable when the three phase contact line crosses the sharp edge of the cylinder. In order to overcome this problem, in our Surface Evolver simulations, we approximate the cylinders as super-ellipsoids (Equation 5.8 in Chapter 5) with a sharpness parameter $\eta = 20$. In this section, we estimate the accuracy of this approximation. In Figure C.1(b), we plot the projection of the particle surface onto the horizontal x-y plane for different values of η for super-ellipsoids with $\alpha = 2.5$. We see that $\eta = 20$ yields a reasonably accurate approximation to the shape of an infinitely sharp cylinder. In Figure C.1(a), we plot $\frac{1}{\cos\theta_t}\frac{\partial \overline{F}_{st}}{\partial \theta_t}$ as a function of θ_t for different values η for cylinders with $\alpha = 2.5$, $\theta_w = 90°$, assuming the liquid meniscus around the particle remains flat. The reason for assuming a flat meniscus is because exact results for the orientational behaviour are known in this case. Specifically, in Figure C.1(a), the infinitely sharp cylinder curve was calculated using the flat interface model, while the results for all other values of η were calculated using Surface Evolver with the interface constrained to remain flat. Note that the position and magnitude of the maxima in $\frac{1}{\cos\theta_t}\frac{\partial \overline{F}_{st}}{\partial \theta_t}$ corresponds to the critical angle and critical field for the irreversible transition from the tilted state to the end-on state (see next section). We see that the Surface Evolver calculations with $\eta = 20$ reproduces the exact curve accurately except for very close to the maximum. Specifically,

the $\eta = 20$ curve under predicts the magnitude of the maximum (and hence the critical field) by around 25% but it under predicts the position of the maximum (and hence the critical angle) by only 2%. Considering the fact that in the exact theory, the maximum is a cusp which is extremely challenging to capture numerically, this level of accuracy is reasonably good. Indeed, in order to reduce the error in the critical field to 10%, we would need to increase the sharpness parameter to $\eta = 120$ (see Figure C.1(a)), which is not achievable numerically if we incorporate realistic deformations of the liquid meniscus. Finally, for cylinders in the side-on state, it is possible to use Surface Evolver to calculate meniscus deformations around cylinders with infinitely sharp corners. For typical cylinders in the side-on state (say $\alpha = 3$, $\theta_w = 80°$), we find that the difference $z_{max} - z_{min}$ between the maximum and minimum contact line heights using Surface Evolver simulations with $\eta = 20$ deviates only by around 10% from the results for an infinitely sharp cylinder. Taking all these estimates into account, we conclude that the value $\eta = 20$ represents a good compromise between numerical stability and accuracy in our Surface Evolver simulations.

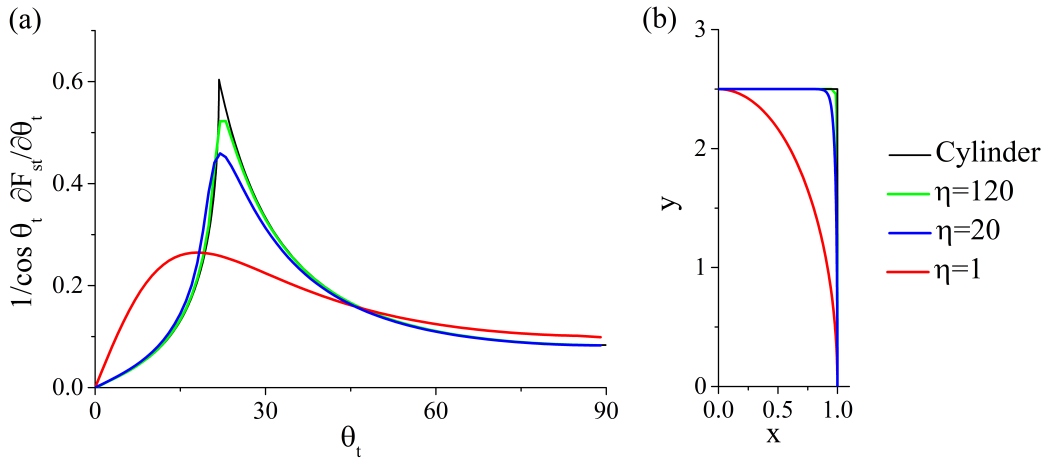

Figure C.1: (a)$\frac{1}{\cos\theta_t}\frac{\partial \bar{F}_{st}}{\partial \theta_t}$ as a function of tilt angle θ_t for an infinitely sharp cylinder calculated from flat interface theory and for rounded cylinders with different η calculated from Surface Evolver simulations where the interface is constrained to be flat. (b) Projection of cylinders with different values of η onto the horizontal plane.

Appendix D
Center-to-Center Distance

The final expression for r_{c-c} is

$$r_{c-c} = \Big(l^2(\cos\theta_b)^2(\cos\theta_t)^2 + 4r^2(\cos\theta_b)^4(\sin\theta_t)^2 + 2r^2(\sin\theta_b)^2(2(\cos\theta_t)^2 + (3+\cos(2\theta_b))(\sin\theta_t)^2)\Big)^{\frac{1}{2}}$$

Appendix E
Elliptical Polar Coordinates

This theory was developed by Lorenzo Botto a Lecturer at Queen Mary University London. It is presented here for completeness.

The amplitudes of dipoles $H = 1$ assuming identical particles. We have a constant aspect ratio $\alpha = 2$ and can calculate our s_0, which is approximately the s coordinate of the contact line, and β that is a length scale related to the distance from the origin; it controls the aspect ratio of constant s ellipses. $s_0 = a \tanh\left(\frac{1}{\alpha}\right)$ and $\beta = r/\sinh(a\tanh(1/\alpha))$. We now require the normalised centre-to-centre separation, $\tilde{r} = r_{12}/\beta$. $\tilde{r}$ is then used in s_1 and $t_1$below

$$s_1 = a \sinh \sqrt{\frac{1}{2}\left(\tilde{r}^2 - 1 + \sqrt{\left((1-\tilde{r}^2)^2 + 4\tilde{r}^2\left(\sin\theta_{b1}\right)^2\right)}\right)}$$

$$t_1 = a \tan 2\left(\tan\left(-\theta_{b1}\right), \tanh\left(s_1\right)\right).$$

$$f\left(\theta_{b1},\, \theta_{b2},\, r_{12}\right) = H^2 \exp\left(-s_0\right) \sinh s_0 \cos\left(\theta_{b1} - \theta_{b2}\right) G + \sin\left(\theta_{b1} - \theta_{b2}\right) L \tag{E.1}$$

where

$$G = \frac{\exp\left(-s_1\right)\left(\sin t_1 \tan t_1 - \cos t_1 \tanh s_1\right)}{\cosh s_1 \cos t_1 \left(\left(\tanh s_1\right)^2 + \left(\tan t_1\right)^2\right)}$$

and

$$L = \frac{\exp\left(-s_1\right)\left(\tanh s_1 \sin t_1 + \tan t_1 \cos t_1\right)}{\cosh s_1 \cos t_1 \left(\left(\tanh s_1\right)^2 + \left(\tan t_1\right)^2\right)}$$

References

[1] B. P. Binks and T. S. Horozov, *Cambridge University Press*, Vol. 1 (2006) pp. 1–74.

[2] F. Günther, S. Frijters, and J. Harting, Soft Matter **10**, 4977 (2014).

[3] K. M. Bromley, R. J. Morris, L. Hobley, G. Brandani, R. M. C. Gillespie, M. McCluskey, U. Zachariae, D. Marenduzzo, N. R. Stanley-Wall, and C. E. MacPhee, Proceedings of the National Academy of Sciences of the United States of America **112**, 5419 (2015).

[4] G. B. Davies, T. Krüger, P. V. Coveney, J. Harting, and F. Bresme, Soft Matter **10**, 6742 (2014).

[5] A. D. Law, M. Auriol, D. Smith, T. S. Horozov, and D. M. A. Buzza, Physical Review Letters **110**, 138301 (2013).

[6] P. A. Kralchevsky and K. Nagayama, *Particles at Fluid Interfaces and Membranes: Attachment of Colloid Particles and Proteins to Interfaces and Formations of Two-Dimensional Arrays* (Elsevier, Amsterdam, 2001) p. vi.

[7] J. C. Loudet, A. M. Alsayed, J. Zhang, and A. G. Yodh, Physical Review Letters **94**, 018301 (2005).

[8] J. C. Loudet, A. G. Yodh, and B. Pouligny, Physical Review Letters **97**, 018304 (2006).

[9] H. Lehle, E. Noruzifar, and M. Oettel, European Physical Journal E **26**, 151 (2008).

[10] M. Oettel and S. Dietrich, Langmuir **24**, 1425 (2008).

[11] E. P. Lewandowski, P. C. Searson, and K. J. Stebe, Journal of Physical Chemistry B **110**, 4283 (2006).

[12] E. P. Lewandowski, M. J. Cavallaro, L. Botto, J. C. Bernate, V. Garbin, and K. J. Stebe, Langmuir **26**, 15142 (2010).

[13] G. Morris, S. J. Neethling, and J. J. Cilliers, Journal of Colloid and Interface Science **354**, 380 (2011).

[14] M. A. Gharbi, M. J. Cavallaro, G. Wu, A. Daniel, R. D. Kamien, S. Yang, and K. J. Stebe, Liquid Crystals **40**, 1619 (2013).

[15] P. M. Johnson, C. M. V. Kats, and A. V. Blaaderen, Langmuir **21**, 11510 (2005).

[16] B. J. Park and D. Lee, ACS Nano **6**, 782 (2012).

[17] L. Yao, L. Botto, M. J. Cavallaro, B. J. Bleier, V. Garbin, and K. J. Stebe, Soft Matter **9**, 779 (2013).

[18] E. P. Lewandowski, J. a. Bernate, A. Tseng, P. C. Searson, and K. J. Stebe, Soft Matter **5**, 886 (2009).

[19] S. C. Glotzer and M. J. Solomon, Nature Materials **6**, 557 (2007).

[20] P.-G. de Gennes, F. Brochard-Wyart, and D. Quéré, *Capillarity and Wetting Phenomena Drops, Bubbles, Pearls, Waves* (Springer, 2004) p. 69.

[21] B. P. Binks, Current Opinion in Colloid & Interface Science **7**, 21 (2002).

[22] J. Faraudo and F. Bresme, Journal of Chemical Physics **118**, 6518 (2003).

[23] L. Botto, E. P. Lewandowski, M. J. Cavallaro, and K. J. Stebe, Soft Matter **8**, 9957 (2012).

[24] D. Y. C. Chan, J. D. Henry, and L. R. White, Journal of Colloid And Interface Science **79**, 410 (1981).

[25] P. A. Kralchevsky and K. Nagayama, Langmuir **10**, 23 (1994).

[26] F. Bresme and M. Oettel, Journal of Physics: Condensed Matter **19**, 413101 (2007).

[27] M. J. Cavallaro, L. Botto, E. P. Lewandowski, M. Wang, and K. J. Stebe, Proceedings of the National Academy of Sciences **108**, 20923 (2011).

[28] N. Bowden, F. Arias, T. Deng, and G. M. Whitesides, Langmuir **17**, 1757 (2001).

[29] A. B. D. Brown, C. G. Smith, and A. R. Rennie, Physical Review E - Statistical Physics, Plasmas, Fluids, and Related Interdisciplinary Topics **62**, 951 (2000).

[30] F. Bresme and J. Faraudo, Journal of Physics: Condensed Matter **19**, 375110 (2007).

[31] A. R. Morgan, N. Ballard, L. A. Rochford, G. Nurumbetov, T. F. Skelhon, and S. A. F. Bon, Soft Matter **9**, 487 (2013).

[32] G. B. Davies, T. Krüger, P. V. Coveney, J. Harting, and F. Bresme, Advanced Materials **26**, 6715 (2014).

[33] S. Dasgupta, M. Katava, M. Faraj, T. Auth, and G. Gompper, Langmuir **30**, 11873 (2014).

[34] L. Botto, L. Yao, R. L. Leheny, and K. J. Stebe, Soft Matter **8**, 4971 (2012).

[35] H. Cooray, P. Cicuta, and D. Vella, Journal of Physics: Condensed Matter **24**, 284104 (2012).

[36] J. C. Loudet and B. Pouligny, EuroPhysics Letters **85**, 28003 (2009).

[37] G. Morris, S. J. Neethling, and J. J. Cilliers, Journal of Colloid and Interface Science **361**, 370 (2011).

[38] G. Morris, S. J. Neethling, and J. J. Cilliers, Minerals Engineering **33**, 87 (2012).

[39] B. J. Newton, K. A. Brakke, and D. M. A. Buzza, Physical Chemistry Chemical Physics **16**, 26051 (2014).

[40] B. J. Newton and D. M. A. Buzza, Soft Matter **12**, 5285 (2016).

[41] D. Stamou, C. Duschl, and D. Johannsmann, Physical Review E **62**, 5263 (2000).

[42] E. W. Weisstein, "Elliptical Cylindrical Coordinates," (2003).

[43] K. D. Danov and P. A. Kralchevsky, Advances in Colloid and Interface Science **154**, 91 (2010).

[44] P. A. Kralchevsky and K. Nagayama, Advances in Colloid and Interface Science **85**, 145 (2000).

[45] K. Nagayama, S. Takeda, S. Endo, and H. Yoshimura, Japanese Journal of Applied Physics **34**, 3947 (1995).

[46] M. Nicolson, Mathematical Proceedings of the Cambridge Philosophical Society **45**, 288 (1949).

[47] M. G. Basavaraj, G. G. Fuller, J. Fransaer, and J. Vermant, Langmuir **22**, 6605 (2006).

[48] B. Madivala, S. Vandebril, J. Fransaer, and J. Vermant, Soft Matter **5**, 1717 (2009).

[49] B. Madivala, J. Fransaer, and J. Vermant, Langmuir **25**, 2718 (2009).

[50] B. J. Park, C.-H. Choi, S.-M. Kang, K. E. Tettey, C.-S. Lee, and D. Lee, Langmuir **29**, 1841 (2013).

[51] B. J. Park, C.-H. Choi, S.-M. Kang, K. E. Tettey, C.-S. Lee, and D. Lee, Soft Matter **9**, 3383 (2013).

[52] M. Mittal and E. M. Furst, Advanced Functional Materials **19**, 3271 (2009).

[53] N. Vandewalle, N. Obara, and G. Lumay, The European Physical Journal E **36**, 127 (2013).

[54] G. Lumay, N. Obara, F. Weyer, and N. Vandewalle, Soft Matter **9**, 2420 (2013).

[55] T. Kimura, M. Yoshino, T. Yamane, M. Yamato, and M. Tobita, Langmuir **20**, 5669 (2004).

[56] A. Snezhko and I. S. Aranson, Nature Materials **10**, 698 (2011).

[57] F. Bresme, European Physical Journal B **64**, 487 (2008).

[58] G. B. Davies and L. Botto, Soft Matter **11**, 7969 (2015).

[59] J. C. Loudet and B. Pouligny, The European Physical Journal E **34**, 1 (2011).

[60] K. A. Brakke, Experimental Mathematics **1**, 141 (1992).

[61] K. A. Brakke, *Surface Evolver Manual* (2012) pp. 9–277.

[62] C. Raufaste, G. Kirstetter, F. Celestini, and S. J. Cox, EuroPhysics Letters **99**, 24001 (2012).

[63] C. Raufaste and S. Cox, Colloids and Surfaces A: Physicochemical and Engineering Aspects **438**, 126 (2013).

[64] K. F. Riley, M. P. Hobson, and S. J. Bence, *Mathematical Methods for Physics and Engineering*, 2nd ed. (Cambridge University Press, 2002) p. 1179.

[65] P. Mendoza Zélis, D. Muraca, J. S. Gonzalez, G. A. Pasquevich, V. A. Alvarez, K. R. Pirota, and F. H. Sanchez, Journal of Nanoparticle Research **15**, 1613 (2013).

[66] N. Hijnen, *Properties and modification of akaganeite-silica rods*, Ph.D. thesis, University of Edinburgh (2013).

[67] K. Huang, *Statistical Mechanics*, 2nd ed. (John Wiley & Sons: New York, 1987).

[68] K. D. Danov, P. A. Kralchevsky, B. N. Naydenov, and G. Brenn, Journal of Colloid and Interface Science **287**, 121 (2005).

[69] B. I. Bleaney and B. Bleaney, *Electricity and Magnetism Vol. 1*, 3rd ed. (Oxford University Press, Oxford, 1976).

[70] J. B. Fournier and P. Galatola, Physical Review E - Statistical, Nonlinear, and Soft Matter Physics **65**, 031601 (2002).